CONTACT DYNAMICS IDENTIFICATION OF HOLDER EXTENSION ASSEMBLY VIA INVERSE STRUCTURAL MODIFICATION METHOD

A THESIS SUBMITTED TO
THE GRADUATE SCHOOL OF NATURAL AND APPLIED SCIENCES
OF
MIDDLE EAST TECHNICAL UNIVERSITY

BY

HANIFE AYYILDIZ

IN PARTIAL FULFILLMENT OF THE REQUIREMENTS
FOR
THE DEGREE OF MASTER OF SCIENCE
IN
MECHANICAL ENGINEERING

JANUARY 2024

Approval of the thesis:

CONTACT DYNAMICS IDENTIFICATION OF HOLDER EXTENSION ASSEMBLY VIA INVERSE STRUCTURAL MODIFICATION METHOD

submitted by **HANIFE AYYILDIZ** in partial fulfillment of the requirements for the degree of **Master of Science** i**n Mechanical Engineering, Middle East Technical University** by,

Prof. Dr. Halil Kalıpçılar
Dean, Graduate School of **Natural and Applied Sciences** _____

Prof. Dr. M.A. Sahir Arıkan
Head of the Department, **Mechanical Engineering** _____

Assist. Prof. Dr. Orkun Özşahin
Supervisor, **Mechanical Engineering, METU** _____

Prof. Dr. H. Nevzat Özgüven
Co-Supervisor, **Mechanical Engineering, METU** _____

Examining Committee Members:

Prof. Dr. Yigit Yazıcıoğlu
Mechanical Engineering, METU _____

Assoc. Prof. Dr. M. Bülent Özer
Mechanical Engineering, METU _____

Assist. Prof. Dr. Orkun Özşahin
Supervisor, **Mechanical Engineering, METU** _____

Assist. Prof. Dr. Gökhan O. Özgen
Mechanical Engineering, METU _____

Assoc. Prof. Dr. Can U. Doğruer
Mechanical Engineering, Hacettepe University _____

Date: 17.01.2024

I hereby declare that all information in this document has been obtained and presented in accordance with academic rules and ethical conduct. I also declare that, as required by these rules and conduct, I have fully cited and referenced all material and results that are not original to this work.

Name Last name : Hanife Ayyıldız

Signature :

ABSTRACT

CONTACT DYNAMICS IDENTIFICATION OF HOLDER EXTENSION ASSEMBLY VIA INVERSE STRUCTURAL MODIFICATION METHOD

Ayyıldız, Hanife
Master of Science, Mechanical Engineering
Supervisor : Asst. Prof. Dr. Orkun Özşahin
Co-Supervisor : Prof. Dr. H. Nevzat Özgüven

January 2024, 145 pages

Chatter is a critical problem in machining operations and can be eliminated using Stability Lobe Diagrams. To determine the stability diagrams, tool point FRF of the assembly is required, and contact dynamics at the holder-extension and extension-tool interfaces directly affect the tool point FRFs. Thus, modeling and identifying the contact dynamics are crucial in the machine tool models for accurately predicting tool point FRFs. This thesis uses the Inverse Structural Modification Method (ISMM) to identify contact dynamics at the holder-extension interface in tool-extension-holder assemblies. The method, first applied to bolted beam connections, is extended to machine tool dynamics using a quasi-static model with a 2x2 complex stiffness matrix. Validation studies involve numerical data, simulated experimental data, and actual experimental results. First, the full receptance matrix of contact dynamics at the interfaces is obtained in numerical studies using finite element (FE) simulations. The study demonstrates the sensitivity of the ISMM to noise using polluted numerical data sets. Simulated experimental studies approximate unmeasured rotational FRFs using the Finite Difference Technique (FDT). The

effects of the Finite Difference Technique (FDT) on identification results are also examined. The results show that second-order FDT does not yield more accurate results than first-order FDT at points near contact dynamics interfaces, comparing FDT results with FE simulation results. Since the contact dynamics faces are inaccessible, the System Equivalent Model Mixing (SEMM) method is employed as an expansion technique. However, due to numerical issues in the calculations of the SEMM method, it does not provide reliable and accurate results. Additionally, the study investigates the impact of the order of FDT on SEMM results, finding that numerical errors increase when rotational FRFs near the contact dynamics interface are approximated using second-order FDT. The SEMM method's limitations are addressed by selecting application points closest to contact interfaces on the holder and extension. These points are then used to validate the ISMM through simulated experiments, and the effects of the initially assumed complex stiffness matrix on identification results are investigated using three different models. Finally, the experimental results from impact testing of the free-free holder-extension assembly are utilized to apply the ISSM. By using these identified results to predict the modes and FRFs of the assembly, it is observed that the identified results align well with the experimental modes and FRFs. The ISMM can accurately predict the first two natural frequencies of the HE assembly, with only a one percent error, through the identified stiffness matrices.

Keywords: Machine Tool Dynamics, Contact Dynamics, FRF Expansion, Dynamic Stiffness

ÖZ

TUTUCU UZATMA SISTEMİNDE BAĞLANTI DİNAMİĞİNİN TERSİNE YAPISAL DEĞİŞİKLİK YÖNTEMİ İLE BELİRLENMESİ

Ayyildiz, Hanife
Yüksek Lisans, Makina Mühendisliği
Tez Yöneticisi : Yrd. Doç. Dr. Orkun Özşahin
Ortak Tez Yöneticisi: Prof. Dr. H. Nevzat Özgüven

Ocak 2024, 145 sayfa

İşleme merkezlerinde kullanılan iş mili takımlarında üretim sırasında performans ve verimliliği olumsuz etkileyen önemli ölçülerde titreşimler oluşmaktadır. Takımın ucundaki frekans tepki fonksiyonun (FTF) bilinmesi ile bu titreşimler önlenebilir. Takım ucunun frekans tepki fonksiyonu, iş mili takımlarının alt parçalarının birbiri ile olan dinamiğinden etkilenmektedir. Bu çalışmada iş mili takımının alt parçası olan uzatma ve tutucu arasındaki temas dinamiğinin Tersine Yapısal Değişiklik Yöntemi (TYDY) ile belirlenmesi amaçlanmıştır. Kullanılan yöntem ilk olarak cıvata ile bağlanmış iki kiriş arasında cıvata bağlantı elemanın dinamik karakteristiğinin belirlenmesi amacıyla kullanılmıştır. Bu çalışmada belirtilen yöntem, 2x2 karmaşık katılık matrisine sahip yarı statik bir model kullanılarak, tutucu-uzatma temas dinamiğinin belirlenmesinde kullanılmıştır. Doğrulama çalışmaları nümerik verileri, simüle edilmiş deneysel verileri ve gerçek deneysel sonuçları kullanarak gerçekleştirilmiştir. Nümerik doğrulama çalışmasında uzatma ve tutucu arasındaki temas dinamiğine ait FTF matrisi sonlu elamanlar simülasyonu ile elde edilmiştir. TYDY' den elde edilen sonuçların gürültü hassasiyetini

göstermek amacıyla nümerik verilere gürültü eklenerek temas dinamiği tekrar belirlenmiştir. Simüle edilen deneysel çalışmamalarda, ölçülemeyen dönme FTF'leri, Sonlu Fark Tekniği (SFT) kullanılarak belirlenmiştir. Kullanılan SFT derecesinin elde edilen temas dinamiği sonuçları üzerindeki etkisi de incelenmiştir. SFT'nin farklı dereceleri ile elde edilen dönme FTF sonuçları sonlu elemanlar simülasyonunda elde edilen FTF sonuçları ile karşılaştırılmış ve temas dinamiği ara yüzlerine yakın noktalarda birinci dereceden SFT'nin ikinci dereceden SFT' den daha doğru sonuç verdiği sonucuna varılmıştır. Temas dinamiği yüzeylerine erişilemediğinden, temas yüzeylerine ait FTF'leri elde etmek amacıyla genişletme tekniği olarak Sistem Eşdeğer Model Karıştırma (SEMK) yöntemi kullanılmıştır. Ancak, SEMK yönteminden kaynaklanan nümerik sorunlar nedeniyle, güvenilir sonuçlar elde edilememiştir. Buna ek olarak, çalışmada kullanılan SFT derecesinin SEMK yönteminden elde edilen sonuçlar üzerindeki etkisi araştırılmış ve temas yüzeylerine yakın ölçüm noktalarında, dönme eksenindeki FTF'lerin, ikinci dereceden SFT kullanılarak hesaplandığında SEMK yönteminden gelen nümerik hataların arttığı tespit edilmiştir. SEMK yöntemi ile güvenilir sonuçlar elde edilemediğinden; tutucu ve uzatma üzerinde temas dinamiği ara yüzlerine en yakın noktalar kullanılarak TYDY tekrar uygulanmıştır. Bu noktalar simüle edilmiş deneyler aracılığıyla TYDY'yi doğrulamak için kullanılmıştır. Buna ek olarak başlangıçta varsayılan karmaşık direngenlik matrisinin elde edilen sonuçlar üzerindeki etkileri üç farklı varsayılan model kullanılarak incelenmiştir. Son olarak, tutucu uzatma montaj mekaniğinin serbest çekiç testi ile elde edilen FTF sonuçları, TYDY'i doğrulamak için kullanılmıştır. Doğrulama çalışmaları sonucunda elde edilen direngenlik değerleri kullanılarak; tutucu- uzatma mekaniğine ait hesaplanan doğal frekans ve FTF sonuçlarının gerçek değerlerle oldukça yakın olduğu görülmüştür. TYDY ile elde edilen temas dinamiğini temsil eden direngenlik değerleri kullanılarak tutucu-uzatma mekaniğinin ilk iki doğal frekansı yaklaşık yüzde bir hata ile belirlenmiştir.

Anahtar Kelimeler: Tezgâh Dinamiği, Temas Dinamiği, Frekans Cevap Fonksiyonu Genişletmesi, Dinamik Direngenlik

To my mother

ACKNOWLEDGMENTS

I would like to express my sincere gratitude to my supervisor, Assist. Prof. Dr. Orkun Özşahin, and co-supervisor, Prof. Dr. H. Nevzat Özgüven, for their invaluable guidance, support, and expertise throughout the entire duration of my thesis. Their insightful feedback and constructive criticism have been pivotal in overcoming various challenges encountered during the research process.

I would like to express my deepest appreciation to my friends Ali Çağrı Batıhan, Baran Yıldırım, Tuğba Boğaz, Merve Aydın, and Kübra Altınışık for their unwavering support, understanding, and encouragement throughout this endeavor. Their belief in my abilities and constant motivation has been a driving force behind my accomplishments.

I would like to express my deepest gratitude to my family, especially my mother, Esergül Ayyıldız, and my father, Fikret Ayyıldız, for their endless love and support throughout my entire life.

TABLE OF CONTENTS

ABSTRACT v

ÖZ vii

ACKNOWLEDGMENTS xi

TABLE OF CONTENTS xii

LIST OF TABLES xv

LIST OF FIGURES xvi

LIST OF ABBREVIATIONS xxi

CHAPTERS .....

1 INTRODUCTION 1

1.1 Literature Review 1

1.1.1 Contact Dynamics Identification in Machine Dynamics 1

1.1.2 Joint Dynamics Identification in Other Mechanical Assemblies 7

1.2 Objective 9

1.3 Layout of the Thesis 10

2 THEORY-MATHEMATICAL MODEL 13

2.1 Modeling Holder-Extension Assembly via Elastic Receptance Coupling 13

2.2 Contact Dynamics Identification via Inverse Structural Modification Method 22

2.2.1 Structural Modification Method (Özgüven, 1990) by Matrix Inversion Method (Özgüven, 1987) 22

2.2.2 Inverse Structural Modification Method (Özgüven & Tekin, 2020) 25

2.2.3 Contact Dynamics Identification of The Holder-Extension Assembly via ISMM Method 27

3 IDENTIFICATION OF COMPLEX STIFFNESS MATRIX OF THE HOLDER EXTENSION INTERFACE- NUMERICAL STUDY 29

3.1 Objective and Problem Description 29

3.2 2 DOF Linear Spring- Dashpot Model.....31

3.3 Identification of Contact Dynamics Parameters by ISMM.....40

3.4 Effects of Identification Ranges on the ISMM's Results.....50

3.5 Effects of Noise on the ISMM's Results.....53

4 SIMULATED EXPERIMENT STUDIES 57

4.1 ANSYS FE Model.....59

4.2 Estimation of RDOF FRFs by Finite Difference Technique.....62

4.3 Obtaining Translational and Rotational FRFs at Contact Face by System Equivalent Model Mixing (SEMM) Method (Klaassen et al., 2018) 68

4.3.1 Hybrid Model 71

4.3.2 Effect of Finite Difference Technique on Hybrid Model.....77

4.4 New Simulated Experiment Model: ISMM Methods via the Closest Points of the Holder and Extension to the Contact Face 81

4.5 Effects of ANSYS FE Modeling Boundary Conditions on FDT Results……
…….....97

4.6 Effects of Assumed Stiffness Properties on the ISMM.....101

5 REAL EXPERIMENT STUDIES.....109

5.1 Tool-Holder-Extension Impact Hammer Test.....111

5.2 Impact Hammer Test via New Extension 115

5.3 Estimation of RDOF FRFs by Finite Difference Technique.....117

5.4 Contact Dynamics Identification by ISMM 120
5.4.1 Assumed Model for ISMM 120
5.4.2 Identification of The Contact Parameters by ISMM 125
5.5 Importance of the Contact Dynamics Definition via Complex Stiffness Matrix ……. 133
6 CONCLUSION AND FUTURE WORK 137
6.1 Conclusion 137
6.2 Future Work 140

LIST OF TABLES

TABLES

Table 3-1 Defined stiffness and damping properties representing contact dynamics 34
Table 3-2 Mechanical properties of holder and extension 34
Table 3-3 Sensitivity Ranges 40
Table 3-4 Results of identified joint parameters 45
Table 3-5 Sensitivity Ranges 50
Table 3-6 Identified stiffness values with polluted data 54
Table 4-1 Mechanical properties of the tool 59
Table 4-2 Transformation matrices [33] 63
Table 4-3 Sensitivity Regions for Closest Points Application 85
Table 4-4 Identified stiffness values for different frequency ranges 94
Table 4-5 Identified natural frequencies for different identification models 95
Table 4-6 Errors of the identified natural frequencies 95
Table 4-7 Assumed stiffness and damping values 102
Table 4-8 Identified stiffness values with three different assumed models 105
Table 4-9 Identified natural frequencies for different assumed models 106
Table 4-10 Identified natural frequency errors 106
Table 5-1 Modal impact test equipment and software 113
Table 5-2 Young's of the holder and extension identified by impact hammer test results 122
Table 5-3 Defined assumed stiffness and damping properties 122
Table 5-4 Identified stiffness values 130
Table 5-5 Identified natural frequencies 132
Table 5-6 Error of the identified natural frequencies 133

LIST OF FIGURES

FIGURES

Figure 1.1 An example of SLD [2] 2
Figure 1.2 Spindle-Holder-Tool Assembly [4] 2
Figure 1.3 Components of the SHT Assembly and contact dynamic stiffness matrix definition in [7] 4
Figure 1.4 Tool-Holder assembly model in [8] 4
Figure 1.5 Identification method used in [8] 5
Figure 1.6 Timoshenko beam elements with distributed contact spring definition [9] 6
Figure 1.7 Two different contact dynamics joint modeling in [10] 6
Figure 2.1 Elastically coupled Holder-Extension assembly and FBD of the substructures and the joint 15
Figure 2.2 Coupled HE assembly 27
Figure 3.1 Technical properties of the holder [29] 30
Figure 3.2 Technical properties of the extension [30] 30
Figure 3.3. Holder-Extension Assembly 30
Figure 3.4 Connection dynamics face of the Holder-Extension assembly 31
Figure 3.5 Holder-Extension assembly 3D ANSYS FE model and spring definition points 33
Figure 3.6 Mesh (upper) and mesh quality matrix (lower) of the assembly 35
Figure 3.7 1st and 2nd mode shape with assumed complex stiffness matrix, $Kassumed * \omega$ 37
Figure 3.8 1st and 2nd mode shape with actual complex stiffness matrix, $Kactual * \omega$ 38
Figure 3.9 Cross translational (upper) and rotational (lower) FRFs between RP1- i and RP2- j 39
Figure 3.10 Cross FRFs in Z and $RotY$ directions for different stiffness values 41
Figure 3.11 Identified stiffness value of kZ 43

Figure 3.12 Identified stiffness values of $kRotY$ 44
Figure 3.13 Identified damping value of cZ (zoom out (upper)- zoom in (lower)) 46
Figure 3.14 Identified damping value of $cRotY$ (zoom out (upper)- zoom in (lower)) 47
Figure 3.15 Calculated FRFs using identified contact parameters between RP1 and RP2 (*i-j*), in *+Z* and *+RotY* direction 49
Figure 3.16 Calculated cross-rotational FRFs using identified contact parameters between RP1 and RP2 (*i-j*) for different identification ranges 51
Figure 3.17 Calculated cross-translational FRFs using identified contact parameters between RP1 and RP2 (*i-j*) for different identification ranges 52
Figure 3.18 Polluted FRFs with different levels of random noise 53
Figure 3.19 Identified FRF results for polluted data 55
Figure 4.1 The procedure of the study for simulated experiment data 58
Figure 4.2. Tool-Extension-Holder assembly FE model 60
Figure 4.3 Comparison of the FRFs by Simulated (Finite Element Model) and Actual Experiment 61
Figure 4.4 Close-accelerometers method for RDOFs [33] 63
Figure 4.5 Translational FRFs used in the FDT (upper) and obtained rotational FRFs at P2 (lower) 65
Figure 4.6 Translational FRFs used in the FDT (upper) and obtained rotational FRFs at P3 (lower) 66
Figure 4.7 Translational FRFs used in the FDT (upper) and obtained rotational FRFs at P4 (lower) 67
Figure 4.8. Visual representation of SEMM method components [25] 69
Figure 4.9 Parent Model- (FE model includes +Z and +RotY FRFs) 70
Figure 4.10 Overlay Model- (FE model includes only +Z FRFs) 71
Figure 4.11 Obtained contact face FRFs via the SEMM Method 73
Figure 4.12. Obtained contact face FRFs via SEMM Method (for different cross FRFs) 76

Figure 4.13. Rotational FRFs for different order Finite Difference Technique (log scale (left), linear scale(right). 78
Figure 4.14 Comparison of Hybrid Models' translational (upper) and rotational (lower) FRFs 79
Figure 4.15 Comparison of the contact faces' translational (upper), and rotational (lower) FRFs for FEM and SEMM models 80
Figure 4.16 Closest Points (P2 and P3) for ISMM Application 81
Figure 4.17 Comparison of the FRF at the new P2 and P3 with their experimental counterparts 82
Figure 4.18 Translational FRFs used in FDT (upper) and obtained rotational FRFs for Simulated Experiment and Duarte Models' Rotational FRFs at P2 83
Figure 4.19 Translational FRFs used in FDT (upper) and obtained rotational FRFs for Simulated Experiment and Duarte Models' Rotational FRFs at P3 84
Figure 4.20 Direct translational and rotational FRFs at P2 for assumed and actual models 86
Figure 4.21 Direct translational and rotational FRFs at P3 for assumed and actual models 87
Figure 4.22 Identified stiffness value of kZ −FEM Model 88
Figure 4.23 Identified stiffness value of kZ −Duarte Model 89
Figure 4.24 Identified stiffness value of $kRotY$ −FEM Model 91
Figure 4.25 Identified stiffness value of $kRotY$ −Duarte Model 92
Figure 4.26 Identified stiffness value of $kRotY$ – FEM (upper) Duarte (lower) Models 93
Figure 4.27 Obtained FRFs with identified stiffness values 96
Figure 4.28 Contact face definition in $\emptyset = 10\ mm$ 98
Figure 4.29 Contact face definition in $\emptyset = 4\ mm$ 98
Figure 4.30 Translational FRFs used in FDT (upper) and rotational FRFs of the FEM and Duarte Models for P2 (lower)-narrow contact face model 99

Figure 4.31 Translational FRFs used in FDT (upper) and rotational FRFs of the FEM and Duarte Models for P3 (lower)-narrow contact face model 100
Figure 4.32 Translational and rotational FRFs for different assumed models 103
Figure 4.33 Comparison of assumed models to the actual model 104
Figure 4.34 Comparison of obtained translational FRFs with identified stiffness values to their actual model equivalent for different Assumed Models 107
Figure 5.1 The procedure followed in identifying connection dynamics using real experimental data 110
Figure 5.2 Data points and test set-up 112
Figure 5.3 Test setup- CutPRO settings 112
Figure 5.4 Direct (upper) and Cross (lower) FRFs from experiments 114
Figure 5.5 FRFs from impact hammer test and their fitted counterparts 116
Figure 5.6 Approximated RDOF FRFs from *Measured* FRFs at P2 118
Figure 5.7 Approximated RDOF FRFs from *Fitted* FRFs at P2 118
Figure 5.8 Approximated RDOF FRFs from *Measured* FRFs at P3 119
Figure 5.9 Approximated RDOF FRFs from *Fitted* FRFs at P3 119
Figure 5.10 Comparison of the holder-tip (upper) and extension-tip (lower) FRFs 121
Figure 5.11 Comparison of cross translational FRFs between P2 and P3 123
Figure 5.12 Cross translational FRF between P3 and P2 for different translational (upper) and rotational (lower) stiffness values 124
Figure 5.13 Identified translational stiffness values by ISMM for *Measured* (upper) and *Fitted (lower)* models 126
Figure 5.14 Identified rotational stiffness values by ISMM for *Measured* (upper) and *Fitted (lower)* models 127
Figure 5.15 Identified stiffnesses for *Measured* (upper) and *Fitted* (lower) model values by ISMM 128
Figure 5.16 Identified rotational stiffness values for *Measured* (left) and *Fitted* (right) models by ISMM (1950-1980 Hz) 129

Figure 5.17 Calculated cross translational FRFs between P2 and P3 using identified contact parameters for *Measured* (upper) *Fitted* (lower) FRFs.....131
Figure 5.18 Direct translational FRF at P3 -FRF obtained by bonded contact definition and comparison with identified FRF.....135

LIST OF ABBREVIATIONS

ABBREVIATIONS

FEM	Finite Element Model
DOF	Degree of Freedom
SEMM	System Equivalent Model Mixing
ISMM	Inverse Structural Modification Method
SLD	Stability Lobe Diagram
RCSA	Receptance Coupling Substructure Analysis
IRCSA	Inverse Receptance Coupling Substructure Analysis
SHT	Spindle-Holder-Tool
SH	Spindle-Holder
HE	Holder-Extension
HET	Holder-Extension-Tool
SEREP	System Equivalent Reduction Expansion Process
VPT	Virtual Point Transformation
FBD	Free Body Diagram
MIM	Matrix Inversion Method

`

CHAPTER 1

INTRODUCTION

1.1 Literature Review

1.1.1 Contact Dynamics Identification in Machine Dynamics

The cutting processes involve the machine tool, cutting tool, and workpiece interactions. Factors like displacements, forces, chip formation, and the workpiece's properties must be considered to describe the process accurately. Machining technologies necessitate an understanding of cutting mechanics and chip formation. Machine tool vibration creates significant problems during machining, including poor surface finish and faster tool wear.

Metal cutting processes can lead to three vibrations: free, forced, and self-excited. Free vibrations occur when the system moves from equilibrium and vibrates freely. Forced vibrations occur due to external harmonic excitations, such as unbalanced bearings or cutting tools. Self-excited vibrations occur during machining and are the most undesirable and least controllable. Chatter is a frequent problem caused by self-excited vibrations. Chatter depends on many factors, such as the dynamic stiffness of the structure and/or the tool, cutting parameters, workpiece, and tool characteristics [1]. Based on regenerative chatter theory, the Stability Lobe Diagram (SLD), shown in Figure 1.1, is an effective tool for predicting and controlling chatter. That diagram shows the stable and unstable regions as a function of spindle speed and axial depth of cut [1]. Tooltip FRF is one of the prerequisites for obtaining SLD. Tooltip FRFs can be measured directly by experimental modal testing. However, as the number of different tools increases, measuring the FRF of each tool experimentally becomes impossible. To eliminate the requirement of FRF

`

measurements, Schmitz et al. [2] first introduced Receptance Coupling Substructure Analysis (RCSA) to create a model for the structural dynamics of a coupled structure through its subsystems.

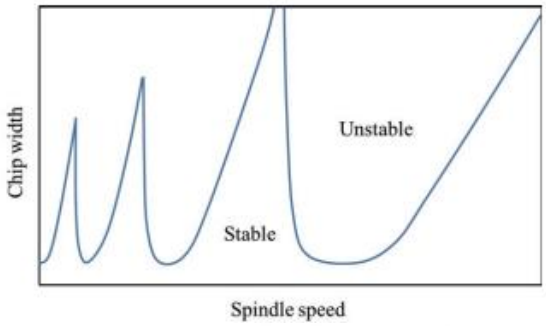


Figure 1.1 An example of SLD [2]

In the RCSA method, tip point FRF of the spindle-holder-tool (SHT) assemblies are obtained by receptance coupling of the subsystems, which are generally machine-spindle and holder-tool (Figure 1.2). The FRF of the subcomponents can be obtained through beam theories (Euler-Bernoulli Beam Theory [2], [3] and Timoshenko Beam Theory [4], [5]), finite element modeling (FEM), or experiments.

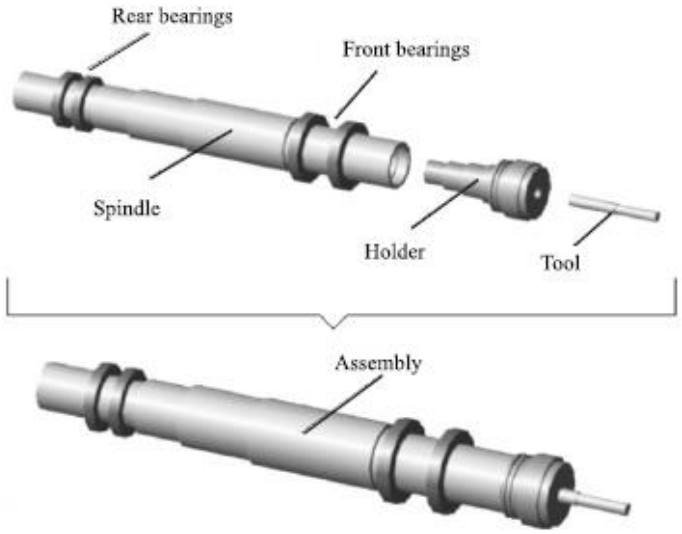


Figure 1.2 Spindle-Holder-Tool Assembly [4]

`

Schmitz et al. [2] used Euler- Bernoulli beam theory to model subsystems where they are coupled elastically. However, the primary concern of the RCSA is the appropriate modeling and definition of the complex stiffness matrix of the contact dynamics, i.e., joint dynamics. Schmitz et al. [2] defined the contact dynamics using only the translational spring-damper model. The model parameters are identified by fitting their numerical FRF results to experimental findings. Park et al. [6] showed the importance of adding rotational FRFs to the coupling processes. They also compared the numerical results obtained with and without rotational dynamics with the experimental ones to prove that adding rotational FRFs leads to more realistic coupling results. Due to the difficulties of obtaining rotational FRFs of the tool-holder assembly, Özşahin et al. [7] proposed the Inverse RCSA (IRCSA) method.

The IRCSA is a mainly receptance decoupling method implemented in machine dynamics systems. The receptance matrix of the substructure of the assembly and the complex stiffness matrix of the contact definition between the substructures can be identified. In the initial stage, the FRFs of the tool tip and holder-spindle's FRFs are acquired through impact testing. Subsequently, the FRFs of the tool located on the external side of the holder are obtained using the analytical solution of the Timoshenko beam and receptance coupling method. Finally, the connection dynamics are determined through the use of the IRCSA.

Özşahin et al. [7] modeled SHT with Timoshenko beam theory, and SHT assembly FRF matrixes are created by elastic coupling (Figure 1.3). Then, both contact dynamics stiffness matrices between the SH and HT are obtained via the IRCSA method. Then, the results are verified with the experiment.

In the studies mentioned before, contact dynamics are identified through single points. Other than those, many studies are based on the multi-point RCSA application. Schmitz et al. [8] implemented the 3-point RCSA method in the TH assembly’s FRF identification (Figure 1.4). They defined a complex stiffness matrix for each contact point with translational and rotational stiffness and damping

`

properties. Nevertheless, in this study, contact's complex stiffness matrix is adopted from another study. The stiffness matrix identification study was not executed.

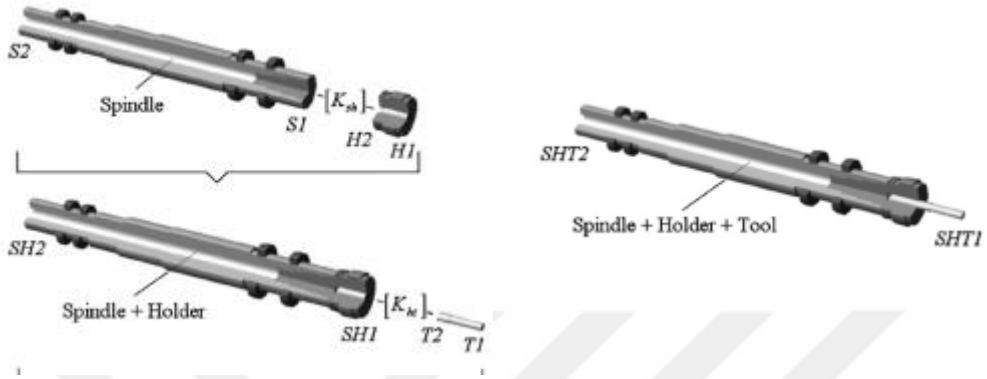


Figure 1.3 Components of the SHT Assembly and contact dynamic stiffness matrix definition in [7]

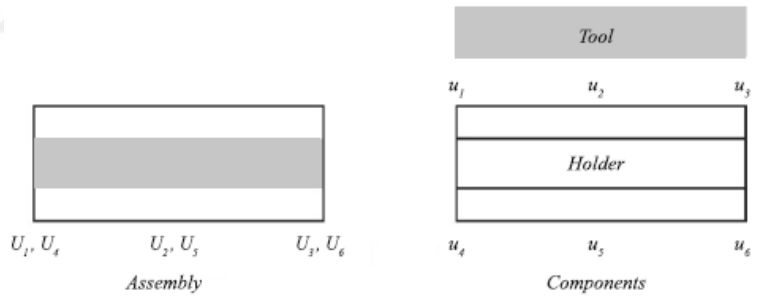


Figure 1.4 Tool-Holder assembly model in [8]

Like single-point RCSA applications, in multi-point RCSA applications, identifying and defining the contact's complex stiffness matrix is also the primary matter. Schmitz et al. [8] used tool-holder finite element simulation to extract the complex stiffness matrix terms to address that issue. The translational stiffness values are calculated by the pressure-displacement curve for the nodes, which describes the contact dynamics (Figure 1.5). The central finite difference technique is then applied

to identify rotational stiffness values. In the end, they found the damping properties from the friction force results of the simulation.

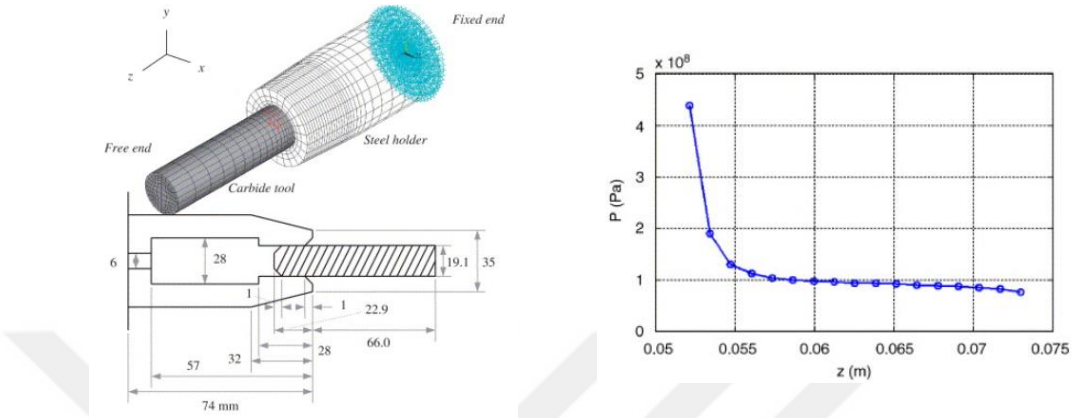


Figure 1.5 Identification method used in [8]

Namazi et al. [9] defined the tapered contact between the holder and spindle as a uniformly distributed translational and rotational stiffness matrix, given in Figure 1.6. To identify the stiffness values in tapered contact, they used the IRCSA method.

Mohammad et al. [10] modeled the contact dynamics as a set of parallel springs (Figure 1.7). The stiffness value of the contact dynamics was obtained by minimizing the difference between RCSA and experimental results.

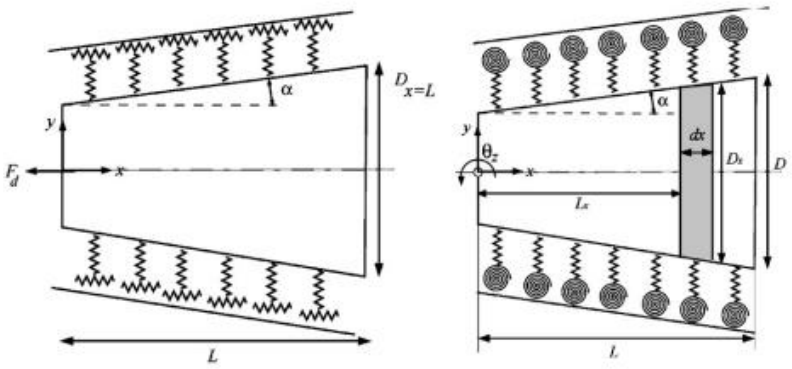


Figure 1.6 Timoshenko beam elements with distributed contact spring definition [9]

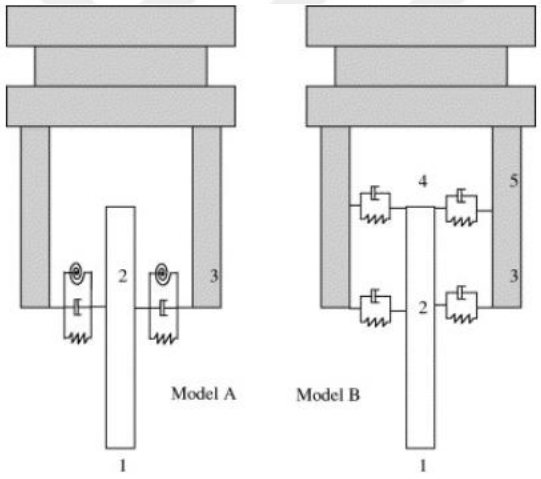


Figure 1.7 Two different contact dynamics joint modeling in [10]

Since the work described in this thesis focuses on joint identification at the holder-extension interface, only previously published research on machine tool dynamics identification is represented. However, various research studies have been conducted to determine the dynamics of mechanical joints. The literature for mechanical joint identification is represented in Section 1.1.2.

1.1.2 Joint Dynamics Identification in Other Mechanical Assemblies

Knowing the dynamics of mechanical joints allows one to estimate assembly dynamics accurately. Several studies have been done to solve the joints' inherent dynamics and identify them correctly. In those studies examined in the literature, this identification can be done through the modal or frequency domains. In modal domain identification methods, it becomes difficult to extract modal parameters from the measurements [11]. Since extracting FRF data from experimental results is more straightforward than modal parameters, FRF-based approaches have received increased attention.

Okuba et al. [12] first tried to extract linear joint stiffness properties by subtracting the substructures from the assembly through the FRF decoupling method. Then, their work is extended by Ren et al. [13], for the system has multiple joints, where the joints are modeled by stiffness, mass, and damping system. They used the weighted least-squares approach to identify joint parameters. Also, in their study, they aimed to select the best equation to minimize the error coming from the measurement. Celic et al. [14] use Ren et al.'s solution extendedly. Their study also shows the importance of including rotational FRF in joint identification. They concluded that joint dynamics are not represented accurately without considering RDOF FRFs. Since the measurement of the RDOF FRFs requires specialized equipment, they tune their FE model with experimental results to obtain RDOF FRFs. In their second study, Celic et al. [15] also discussed the reduction of the coordinate system based on the numerical studies. In their second work, they concluded that if the reduced model is used in joint identification, all the joint DOFs must be included to estimate the joint properties accurately. They validate their work with simulated and experimental results through simple bolted beam assembly.

Wang et al. [16] estimated FRF using an unmeasured FRF approach. In their investigation, they estimated the unmeasured FRFs by tailoring the results of their FE model to the experimental results. Then, using receptance decoupling, they generate identification. They further demonstrate that, in their in-line bolted beam

configuration, the impacts of noise due to a lack of FRFs may be avoided if the unmeasured FRFs are approximated and taken into account in decoupling equations by getting unmeasured FRFs. Tol et al. [17] also used the FRF decoupling method to identify bolted connections' complex stiffness matrix properties for the in-line beam assembly. The verification of the proposed method is done not only through numerical simulations but also experimentally. They also proposed an optimization algorithm to minimize the numerical error due to inverse matrix calculations. Özgüven et al. [18] identified the in-line beam connection element's complex stiffness matrix via the proposed Inverse Structural Modification Method (ISMM). In this study, joint dynamics identification was conducted through only numerical studies. The used stiffness matrix components, named actual and assumed stiffness matrix, are adopted from the earlier studies.

In all the studies mentioned above, the identification is done by correlated FE models, known joint dynamics properties from earlier studies, or by measuring FRFs close to joint dynamics. Especially in experimental studies where highly accurate joint dynamics identification is required, the noise from close points measurement creates issues. To eliminate the noise problem, Meggie et al. [19] used the in-situ decoupling method without the substructure measurement.

The identification studies that use the FRF decoupling method shared earlier use simple structures, mostly bolted beam connections, for experimental validation studies. That is because it is easy to measure the joint dynamics of FRFs near the connection. However, when the assembly is complex, and it is impossible to reach the joint interface of the substructures to get FRF measurements, it necessitates using an expansion method. Other than tuning FE models with experimental results, several methods enable the extraction of rotational FRFs from known and/or measured translational FRFs. The System Equivalent Reduction and Expansion (SEREP) method [20] is one of the modal domain expansion techniques that requires the mode, mode shapes, and the damping properties of the assembly, which makes it challenging to use in experimental identifications because it is hard to extract modal properties from the signal. The studies that used SEREP can be found in [21]

and [22]. Silva et al. [23] used Kidder's Method, another modal domain expansion technique, to estimate rotational FRFs in their study.

The Virtual Point Transformation (VPT) [24] is another technique for FRF expansion for unreachable places. In that method, the joint location is defined as a virtual point, and the measurements are done close to the VP. Then, FRFs at the joint are obtained through the formulas given in [24].

Klassen et al. [25] introduced the System equivalent Model Mixing Method (SEMM), a hybrid FRF expansion technique. In that technique, the experimental model is expanded on the numerical model where the unreachable joint dynamics are. In this method, it is essential to create a numerical model that represents the actual model correctly. If the difference between the models exists, this leads to an error in the identification procedure [26]. Klassen et al. [26] used the SEMM method to identify joint dynamics through the FRF decoupling method. Since the joint faces are unreachable, they used the SEMM method to get the FRF of the substructures around the bolt.

1.2 Objective

The objective of this thesis study is to identify a complex stiffness matrix that represents the interface dynamics between the Holder and Extension through the Inverse Structural Modification Method (ISMM).

The ISMM, previously applied to in-line bolted beam assembly [18] to identify bolt dynamics, is now applied to the Holder- Extension assembly to represent the contact between the holder and extension. Also, unlike in the [18], the method is applied to numerical models and experimental results. The applicability of the ISMM in experimental studies is also discussed and shared in this thesis. The simulated experimental studies examine the effects of the approximation technique used to obtain the rotational FRFs by comparing the results of the different orders of the technique. Since the connection dynamics are inaccessible, the SEMM method is

`

used as the expansion technique. Previously done works show the numerical issues raised due to the manipulation of the SEMM, so the SEMM method does not provide reliable results. This outcome is also validated in this thesis work.

In real experimental studies, the importance of the Elastic Modulus values is also examined to increase the accuracy of the identification results.

1.3 Layout of the Thesis

The outline of the thesis is as follows:

Chapter 2 introduces the theory behind the Inverse Structural Modification Method (ISMM). This introduction starts with creating receptance matrix equations for the elastically coupled HE assembly. Then, the application of the ISMM to the contact dynamics identification of the HE assembly introduced based on the Structural Modification Method (SMM) and Matrix Inversion Method (MIM) is shown.

Chapter 3 shows the application of the ISMM on the HE assembly through numerical studies. The assembly is modeled in ANSYS FE software as a 3D body. Since the assembly is almost symmetrical, the contact dynamics properties, which are stiffness and damping, are defined in 2 DOFs. Also, that chapter investigates the effects of the noise on the identified contact dynamics results.

In Chapter 4, the application of the ISMM to the actual experiment studies is done through simulated experimental results. The translational FRF results obtained in Chapter 3 are accepted as actual experimental results. Expansion techniques are used to obtain the RDOF FRFs, and their effects on the identified contact dynamics results are investigated. After verification studies are completed, the effects of the assumed complex stiffness matrix on the identification results are shown with three assumed models.

Chapter 5 provides the application of the ISMM in impact hammer test results. Here, the applicability of the ISMM is verified, firstly, by experimental data. Also, a case

study demonstrates the importance of defining contact dynamics elastically instead of rigidly.

At the end of the thesis, in Chapter 6, the conclusion is presented, and recommendations for future studies based on this thesis are shared.

`

`

CHAPTER 2

THEORY-MATHEMATICAL MODEL

Chatter decreases the performance of the Tool-Extention-Holder assemblies in machine centers. Based on the tool tip FRFs, SLD diagrams are used to predict chatter to decrease the vibration level. Tool tip FRF mainly relies on the contact dynamics between the substructures. If the dynamics of the substructures and the contact dynamics between the substructures are known, the tool tip FRFs can be determined through the receptance coupling equation. Several studies that rely on receptance coupling are shared in Section 1.1.

In this chapter, in Section 2.1, the receptance coupling theory of the elastically coupled Holder-Extension assembly is shared based on the free-free boundary condition. Then, in Section 2.2.2, the theory of the Inverse Structural Modification Method, first introduced in [18] based on the bolted joint dynamics identification, is shared, and then the application of this method to the HE assembly is utilized in Section 2.2.3.

2.1 Modeling Holder-Extension Assembly via Elastic Receptance Coupling

Before starting the theory of receptance coupling, some assumptions are made. Those are as follows:

- In reality, Holder and Extension are connected by shrink fit. In this study, the connection is assumed through a singular face where the connection dynamics are represented in Figure 2.1.
- The connection dynamics are assumed to be linear.
- Although the bodies are 3D, the receptance coupling is done through 2DOF due to the symmetricity of the Holder and Extension assembly.

`

- A complex stiffness matrix with only stiffness and damping properties represents the connection dynamics. Connection elements are modeled with zero mass.
- The Holder-Extension assembly is in free-free condition.
- There is no external displacement, force, or moment on the systems.

To explain the theory of receptance coupling, let's consider the substructures, which are Holder-$\boldsymbol{H}$ and Extension-$\boldsymbol{E}$ (Figure 2.1), connected via two DOF complex linear elastic coupling elements, which is K^*. In Figure 2.1, *r* and *s* represent internal DOFs, whereas *j* and *k* represent joint dynamics DOFs. The DOFs of the system are translational- *x* and rotational- θ directions. The free body diagram (FBD) of the subsystems and the joint are given in Figure 2.1. The notations of $\boldsymbol{F}$ and $\boldsymbol{M}$ used in Figure 2.1 represent force and moments at the relevant locations.

The equilibrium equations of each subsystem are as follows:

<u>*Holder*</u>

$$\{x^{\boldsymbol{H}}\} = [\alpha^{\boldsymbol{H}}]\,\{F^{\boldsymbol{H}}\} \tag{2.1}$$

$$\begin{Bmatrix} x_r^{\boldsymbol{H}} \\ \theta_r^{\boldsymbol{H}} \\ x_j^{\boldsymbol{H}} \\ \theta_j^{\boldsymbol{H}} \end{Bmatrix} = \begin{bmatrix} [H_{rr}]^{\boldsymbol{H}} & [H_{rj}]^{\boldsymbol{H}} \\ [H_{jr}]^{\boldsymbol{H}} & [H_{jj}]^{\boldsymbol{H}} \end{bmatrix} \begin{Bmatrix} F_r^{\boldsymbol{H}} \\ M_r^{\boldsymbol{H}} \\ F_j^{\boldsymbol{H}} + F_j^{\boldsymbol{joint}} \\ M_j^{\boldsymbol{H}} + M_j^{\boldsymbol{joint}} \end{Bmatrix} \tag{2.2}$$

where H stands for the receptance matrix, and details of the matrixes in Equation (2.2) are as follows:

$$[\mathrm{H}_{rr}]^{\boldsymbol{H}} = \begin{bmatrix} \mathrm{H}_{r_x r_x}{}^{\boldsymbol{H}} & \mathrm{H}_{r_x r_\theta}{}^{\boldsymbol{H}} \\ \mathrm{H}_{r_\theta r_x}{}^{\boldsymbol{H}} & \mathrm{H}_{r_\theta r_\theta}{}^{\boldsymbol{H}} \end{bmatrix} \tag{2.3}$$

$$[\mathrm{H}_{rj}]^{\boldsymbol{H}} = \begin{bmatrix} \mathrm{H}_{r_x j_x}{}^{\boldsymbol{H}} & \mathrm{H}_{r_x j_\theta}{}^{\boldsymbol{H}} \\ \mathrm{H}_{r_\theta j_x}{}^{\boldsymbol{H}} & \mathrm{H}_{r_\theta j_\theta}{}^{\boldsymbol{H}} \end{bmatrix} \tag{2.4}$$

$$[\mathrm{H}_{jr}]^{\boldsymbol{H}} = \begin{bmatrix} \mathrm{H}_{j_x r_x}{}^{\boldsymbol{H}} & \mathrm{H}_{j_x r_\theta}{}^{\boldsymbol{H}} \\ \mathrm{H}_{j_\theta r_x}{}^{\boldsymbol{H}} & \mathrm{H}_{j_\theta r_\theta}{}^{\boldsymbol{H}} \end{bmatrix} \tag{2.5}$$

$$[\mathrm{H}_{jj}]^{\boldsymbol{H}} = \begin{bmatrix} \mathrm{H}_{j_x j_x}{}^{\boldsymbol{H}} & \mathrm{H}_{j_x j_\theta}{}^{\boldsymbol{H}} \\ \mathrm{H}_{j_\theta j_x}{}^{\boldsymbol{H}} & \mathrm{H}_{j_\theta j_\theta}{}^{\boldsymbol{H}} \end{bmatrix} \tag{2.6}$$

`

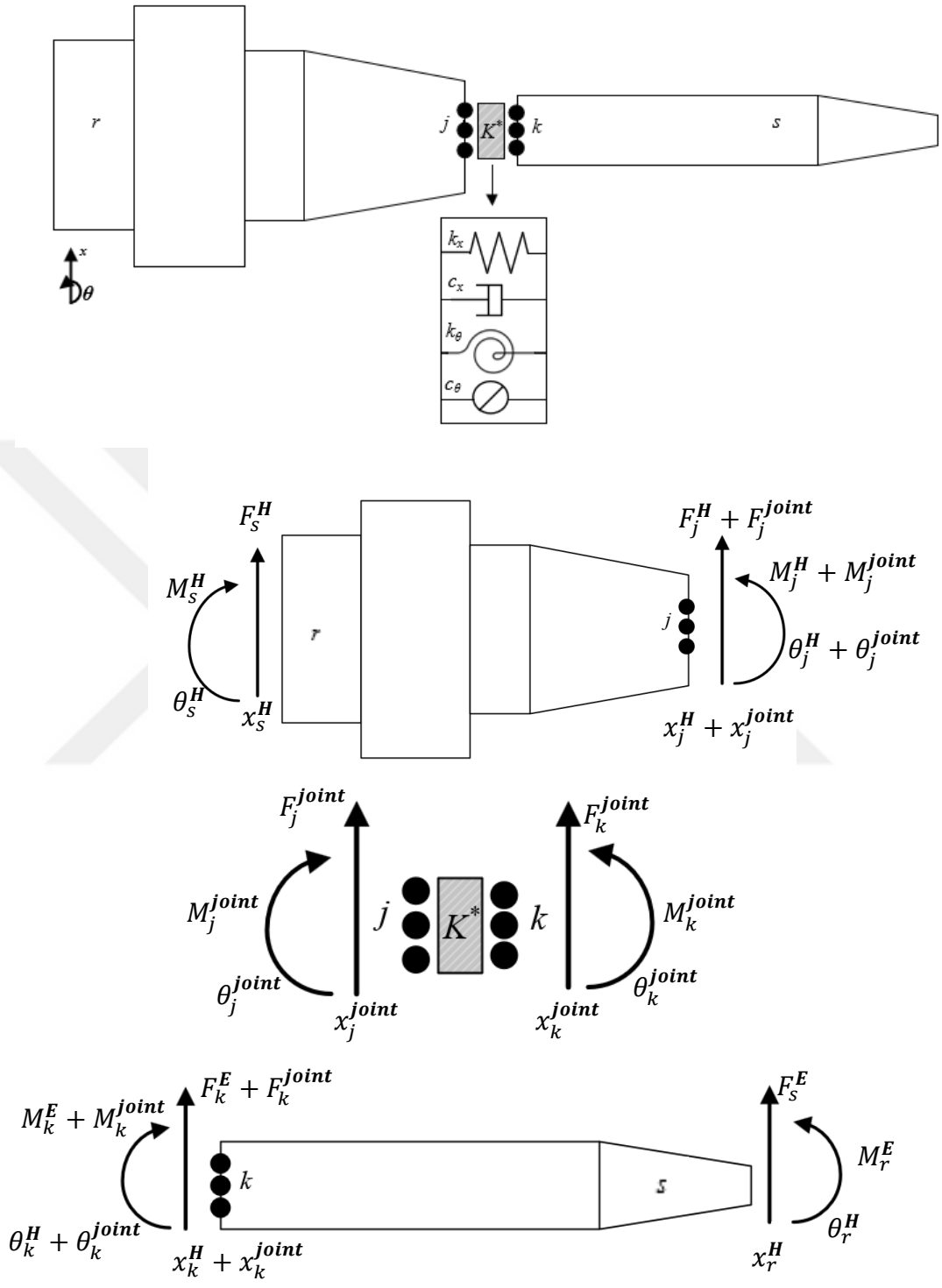


Figure 2.1 Elastically coupled Holder-Extension assembly and FBD of the substructures and the joint

`

Extension

$$\{x^{\boldsymbol{E}}\} = [\alpha^{\boldsymbol{E}}]\,\{F^{\boldsymbol{E}}\} \tag{2.7}$$

$$\begin{Bmatrix} x_k^{\boldsymbol{E}} \\ \theta_k^{\boldsymbol{E}} \\ x_s^{\boldsymbol{E}} \\ \theta_s^{\boldsymbol{E}} \end{Bmatrix} = \begin{bmatrix} [H_{kk}]^{\boldsymbol{E}} & [H_{ks}]^{\boldsymbol{E}} \\ [H_{sk}]^{\boldsymbol{E}} & [H_{ss}]^{\boldsymbol{E}} \end{bmatrix} \begin{Bmatrix} F_k^{\boldsymbol{E}} + F_k^{\boldsymbol{joint}} \\ M_k^{\boldsymbol{E}} + M_k^{\boldsymbol{joint}} \\ F_s^{\boldsymbol{E}} \\ M_s^{\boldsymbol{E}} \end{Bmatrix} \tag{2.8}$$

where H stands for the receptance matrix, and details of the matrixes in Equation (2.8) are as follows:

$$[\mathrm{H}_{kk}]^{\boldsymbol{E}} = \begin{bmatrix} \mathrm{H}_{k_x k_x}{}^{\boldsymbol{E}} & \mathrm{H}_{k_x k_\theta}{}^{\boldsymbol{E}} \\ \mathrm{H}_{k_\theta k_x}{}^{\boldsymbol{E}} & \mathrm{H}_{k_\theta k_\theta}{}^{\boldsymbol{E}} \end{bmatrix} \tag{2.9}$$

$$[\mathrm{H}_{ks}]^{\boldsymbol{E}} = \begin{bmatrix} \mathrm{H}_{k_x s_x}{}^{\boldsymbol{E}} & \mathrm{H}_{k_x s_\theta}{}^{\boldsymbol{E}} \\ \mathrm{H}_{k_\theta s_x}{}^{\boldsymbol{E}} & \mathrm{H}_{k_\theta s_\theta}{}^{\boldsymbol{E}} \end{bmatrix} \tag{2.10}$$

$$[\mathrm{H}_{sk}]^{\boldsymbol{E}} = \begin{bmatrix} \mathrm{H}_{s_x k_x}{}^{\boldsymbol{E}} & \mathrm{H}_{s_x k_\theta}{}^{\boldsymbol{E}} \\ \mathrm{H}_{s_\theta k_x}{}^{\boldsymbol{E}} & \mathrm{H}_{s_\theta k_\theta}{}^{\boldsymbol{E}} \end{bmatrix} \tag{2.11}$$

$$[\mathrm{H}_{ss}]^{\boldsymbol{E}} = \begin{bmatrix} \mathrm{H}_{s_x s_x}{}^{\boldsymbol{E}} & \mathrm{H}_{s_x s_\theta}{}^{\boldsymbol{E}} \\ \mathrm{H}_{s_\theta s_x}{}^{\boldsymbol{E}} & \mathrm{H}_{s_\theta s_\theta}{}^{\boldsymbol{E}} \end{bmatrix} \tag{2.12}$$

Substructures, Holder, and Extension are then connected via a complex stiffness matrix, K^* which has stiffness and damping properties. The complex stiffness matrix is as follows:

$$[K^*(\omega)] = \begin{bmatrix} K_x^*(\omega) & 0 \\ 0 & K_\theta^*(\omega) \end{bmatrix} \tag{2.13}$$

$$= \begin{bmatrix} k_x + c_x(\omega) & -(k_x + c_x(\omega)) & 0 & 0 \\ -(k_x + c_x(\omega)) & k_x + c_x(\omega) & 0 & 0 \\ 0 & 0 & (k_\theta + c_\theta(\omega)) & -(k_\theta + c_\theta(\omega)) \\ 0 & 0 & -(k_\theta + c_\theta(\omega)) & (k_\theta + c_\theta(\omega)) \end{bmatrix} \tag{2.14}$$

From the equilibrium of forces (force and moment) and compatibility of displacements (translational and rotational), one can write:

$$\begin{Bmatrix} F_j^{\boldsymbol{joint}} \\ M_j^{\boldsymbol{joint}} \end{Bmatrix} + \begin{Bmatrix} F_k^{\boldsymbol{joint}} \\ M_k^{\boldsymbol{joint}} \end{Bmatrix} = 0$$

(2.15)

$$c_x(\dot{x}_k^{\boldsymbol{E}} - \dot{x}_j^{\boldsymbol{E}}) + k_x(x_k^{\boldsymbol{E}} - x_j^{\boldsymbol{E}}) = F_j^{\boldsymbol{joint}}$$

(2.16)

$$c_\theta(\dot{\theta}_k^{\boldsymbol{E}} - \dot{\theta}_j^{\boldsymbol{E}}) + k_\theta(\theta_k^{\boldsymbol{E}} - \theta_j^{\boldsymbol{E}}) = M_j^{\boldsymbol{joint}}$$

(2.17)

By rearranging Equations (2.16) and (2.17) and using Equation (2.14), one can write:

$$\begin{Bmatrix} x_k^{\boldsymbol{E}} - x_j^{\boldsymbol{H}} \\ \theta_k^{\boldsymbol{E}} - \theta_j^{\boldsymbol{H}} \end{Bmatrix} = [K^*(\omega)]^{-1} \begin{Bmatrix} F_j^{\boldsymbol{joint}} \\ M_j^{\boldsymbol{joint}} \end{Bmatrix}$$

(2.18)

To make use of the receptance derivation, let's define $[\alpha^{\boldsymbol{joint}}]$ as the receptance of the joint as follows:

$$[K^*(\omega)]^{-1} = [\alpha^{\boldsymbol{joint}}] = \begin{bmatrix} [H_{xx}]^{\boldsymbol{joint}} & 0 \\ 0 & [H_{\theta\theta}]^{\boldsymbol{joint}} \end{bmatrix}$$

(2.19)

$$[\mathrm{H}_{xx}]^{\boldsymbol{joint}} = \begin{bmatrix} \mathrm{H}_{j_x j_x}{}^{\boldsymbol{joint}} & \mathrm{H}_{j_x k_x}{}^{\boldsymbol{joint}} \\ \mathrm{H}_{k_x j_x}{}^{\boldsymbol{joint}} & \mathrm{H}_{k_x k_x}{}^{\boldsymbol{joint}} \end{bmatrix} \quad [\mathrm{H}_{\theta\theta}]^{\boldsymbol{joint}} = \begin{bmatrix} \mathrm{H}_{j_\theta j_\theta}{}^{\boldsymbol{joint}} & \mathrm{H}_{j_\theta k_\theta}{}^{\boldsymbol{joint}} \\ \mathrm{H}_{k_\theta j_\theta}{}^{\boldsymbol{joint}} & \mathrm{H}_{k_\theta k_\theta}{}^{\boldsymbol{joint}} \end{bmatrix}$$

(2.20) (2.21)

So, Equation (2.18) becomes

$$\begin{Bmatrix} x_k^{\boldsymbol{E}} - x_j^{\boldsymbol{H}} \\ \theta_k^{\boldsymbol{E}} - \theta_j^{\boldsymbol{H}} \end{Bmatrix} = [\alpha^{\boldsymbol{joint}}] \begin{Bmatrix} F_j^{\boldsymbol{joint}} \\ M_j^{\boldsymbol{joint}} \end{Bmatrix}$$

(2.22)

By using Equations (2.2) to (2.4), $x_j^{\boldsymbol{H}}$, $\theta_j^{\boldsymbol{H}}$, $x_k^{\boldsymbol{E}}$, and $\theta_k^{\boldsymbol{E}}$ can be written as follows:

`

$$x_j^{\boldsymbol{H}} = \mathrm{H}_{j_x r_x}{}^{\boldsymbol{H}} F_r^{\boldsymbol{H}} + \mathrm{H}_{j_x r_\theta}{}^{\boldsymbol{H}} M_r^{\boldsymbol{H}} + \mathrm{H}_{j_x j_x}{}^{\boldsymbol{H}} (F_j^{\boldsymbol{H}} + F_j^{\boldsymbol{joint}}) + \mathrm{H}_{j_x j_\theta}{}^{\boldsymbol{H}} (M_j^{\boldsymbol{H}} + M_j^{\boldsymbol{joint}})$$

(2.23)

$$\theta_j^{\boldsymbol{H}} = \mathrm{H}_{j_\theta r_x}{}^{\boldsymbol{H}} F_r^{\boldsymbol{H}} + \mathrm{H}_{j_\theta r_\theta}{}^{\boldsymbol{H}} M_r^{\boldsymbol{H}} + \mathrm{H}_{j_\theta j_x}{}^{\boldsymbol{H}} (F_j^{\boldsymbol{H}} + F_j^{\boldsymbol{joint}}) + \mathrm{H}_{j_\theta j_\theta}{}^{\boldsymbol{H}} (M_j^{\boldsymbol{H}} + M_j^{\boldsymbol{joint}})$$

(2.24)

$$x_k^{\boldsymbol{E}} = \mathrm{H}_{k_x k_x}{}^{\boldsymbol{E}} (F_k^{\boldsymbol{E}} + F_k^{\boldsymbol{joint}}) + \mathrm{H}_{k_x k_\theta}{}^{\boldsymbol{E}} (M_k^{\boldsymbol{E}} + M_k^{\boldsymbol{joint}}) + \mathrm{H}_{k_x s_x}{}^{\boldsymbol{E}} F_s^{\boldsymbol{E}} + \mathrm{H}_{k_x s_\theta}{}^{\boldsymbol{E}} M_s^{\boldsymbol{E}}$$

(2.25)

$$\theta_k^{\boldsymbol{E}} = \mathrm{H}_{k_\theta k_x}{}^{\boldsymbol{E}} (F_k^{\boldsymbol{E}} + F_k^{\boldsymbol{joint}}) + \mathrm{H}_{k_\theta k_\theta}{}^{\boldsymbol{E}} (M_k^{\boldsymbol{E}} + M_k^{\boldsymbol{joint}}) + \mathrm{H}_{k_\theta s_x}{}^{\boldsymbol{E}} F_s^{\boldsymbol{E}} + \mathrm{H}_{k_\theta s_\theta}{}^{\boldsymbol{E}} M_s^{\boldsymbol{E}}$$

(2.26)

Now, look at Equation (2.22) and by rearranging Equation (2.22), one can find it as follows:

$$\begin{Bmatrix} [H_{xx}]^{\boldsymbol{joint}} F_j^{\boldsymbol{joint}} \\ [H_{\theta\theta}]^{\boldsymbol{joint}} M_j^{\boldsymbol{joint}} \end{Bmatrix} = \begin{Bmatrix} x_k^{\boldsymbol{E}} - x_j^{\boldsymbol{H}} \\ \theta_k^{\boldsymbol{E}} - \theta_j^{\boldsymbol{H}} \end{Bmatrix}$$

(2.27)

To calculate ($[H_{xx}]^{\boldsymbol{joint}} F_j^{\boldsymbol{joint}}$), use Equations (2.25) and (2.23) and replace the terms $F_k^{\boldsymbol{joint}}$ and $M_k^{\boldsymbol{joint}}$ with $-F_j^{\boldsymbol{joint}}$ and $-M_j^{\boldsymbol{joint}}$, respectively. So,

$$[H_{xx}]^{\boldsymbol{joint}} F_j^{\boldsymbol{joint}} = \mathrm{H}_{k_x k_x}{}^{\boldsymbol{E}} F_k^{\boldsymbol{E}} - \mathrm{H}_{k_x k_x}{}^{\boldsymbol{E}} F_j^{\boldsymbol{joint}} + \mathrm{H}_{k_x k_\theta}{}^{\boldsymbol{E}} M_k^{\boldsymbol{E}} - \mathrm{H}_{k_x k_\theta}{}^{\boldsymbol{E}} M_j^{\boldsymbol{joint}} \ldots$$

$$\ldots + \mathrm{H}_{k_x s_x}{}^{\boldsymbol{E}} F_s^{\boldsymbol{E}} + \mathrm{H}_{k_x s_\theta}{}^{\boldsymbol{E}} M_s^{\boldsymbol{E}} - \mathrm{H}_{j_x r_x}{}^{\boldsymbol{H}} F_r^{\boldsymbol{H}} - \mathrm{H}_{j_x r_\theta}{}^{\boldsymbol{H}} M_r^{\boldsymbol{H}} - \mathrm{H}_{j_x j_x}{}^{\boldsymbol{H}} F_j^{\boldsymbol{H}} -$$

$$\mathrm{H}_{j_x j_x}{}^{\boldsymbol{H}} F_j^{\boldsymbol{joint}} \ldots$$

$$\ldots - \mathrm{H}_{j_x j_\theta}{}^{\boldsymbol{H}} M_j^{\boldsymbol{H}} - \mathrm{H}_{j_x j_\theta}{}^{\boldsymbol{H}} M_j^{\boldsymbol{joint}}$$

(2.28)

To calculate ($[H_{\theta\theta}]^{\boldsymbol{joint}} M_j^{\boldsymbol{joint}}$), use Equations (2.26), (2.24), and (2.23) and replace the terms $F_k^{\boldsymbol{joint}}$ and $M_k^{\boldsymbol{joint}}$ with $-F_j^{\boldsymbol{joint}}$ and $-M_j^{\boldsymbol{joint}}$, respectively. So,

`

$$[H_{\theta\theta}]^{\boldsymbol{joint}}\, M_j^{\boldsymbol{joint}}$$

$$= \mathrm{H}_{k_\theta k_x}{}^{\boldsymbol{E}} F_k^{\boldsymbol{E}} - \mathrm{H}_{k_\theta k_x}{}^{\boldsymbol{E}} F_j^{\boldsymbol{joint}} + \mathrm{H}_{k_\theta k_\theta}{}^{\boldsymbol{E}} M_k^{\boldsymbol{E}} - \mathrm{H}_{k_\theta k_\theta}{}^{\boldsymbol{E}} M_j^{\boldsymbol{joint}} \ldots$$

$$\ldots + \mathrm{H}_{k_\theta s_x}{}^{\boldsymbol{E}} F_s^{\boldsymbol{E}} + \mathrm{H}_{k_\theta s_\theta}{}^{\boldsymbol{E}} M_s^{\boldsymbol{E}} - \mathrm{H}_{j_\theta r_x}{}^{\boldsymbol{H}} F_r^{\boldsymbol{H}} - \mathrm{H}_{j_\theta r_\theta}{}^{\boldsymbol{H}} M_r^{\boldsymbol{H}} - \mathrm{H}_{j_\theta j_x}{}^{\boldsymbol{H}} F_j^{\boldsymbol{H}} - \mathrm{H}_{j_\theta j_x}{}^{\boldsymbol{H}} F_j^{\boldsymbol{joint}} \ldots$$

$$\ldots - \mathrm{H}_{j_\theta j_x}{}^{\boldsymbol{H}} F_j^{\boldsymbol{joint}} - \mathrm{H}_{j_\theta j_\theta}{}^{\boldsymbol{H}} M_j^{\boldsymbol{H}} - \mathrm{H}_{j_\theta j_\theta}{}^{\boldsymbol{H}} M_j^{\boldsymbol{joint}})$$

(2.29)

Equations (2.28) and (2.29) can be arranged as follows:

$$\left[[H_{xx}]^{\boldsymbol{joint}} + \mathrm{H}_{k_x k_x}{}^{\boldsymbol{E}} + \mathrm{H}_{j_x j_x}{}^{\boldsymbol{H}} \quad \mathrm{H}_{k_x k_\theta}{}^{\boldsymbol{E}} + \mathrm{H}_{j_x j_\theta}{}^{\boldsymbol{H}}\right] \begin{Bmatrix} F_j^{\boldsymbol{joint}} \\ M_j^{\boldsymbol{joint}} \end{Bmatrix} \ldots$$

$$\ldots = \left[\mathrm{H}_{k_x k_x}{}^{\boldsymbol{E}} \quad \mathrm{H}_{k_x k_\theta}{}^{\boldsymbol{E}}\right] \begin{Bmatrix} F_k^{\boldsymbol{E}} \\ M_k^{\boldsymbol{E}} \end{Bmatrix} + \left[\mathrm{H}_{k_x s_x}{}^{\boldsymbol{E}} \quad \mathrm{H}_{k_x s_\theta}{}^{\boldsymbol{E}}\right] \begin{Bmatrix} F_s^{\boldsymbol{E}} \\ M_s^{\boldsymbol{E}} \end{Bmatrix} \ldots$$

$$\ldots - \left[\mathrm{H}_{j_x r_x}{}^{\boldsymbol{H}} \quad \mathrm{H}_{j_x r_\theta}{}^{\boldsymbol{H}}\right] \begin{Bmatrix} F_r^{\boldsymbol{H}} \\ M_r^{\boldsymbol{H}} \end{Bmatrix} - \left[\mathrm{H}_{j_x j_x}{}^{\boldsymbol{H}} \quad \mathrm{H}_{j_x j_\theta}{}^{\boldsymbol{H}}\right] \begin{Bmatrix} F_j^{\boldsymbol{H}} \\ M_j^{\boldsymbol{H}} \end{Bmatrix}$$

(2.30)

$$\left[\mathrm{H}_{k_\theta k_x}{}^{\boldsymbol{E}} + \mathrm{H}_{j_\theta j_x}{}^{\boldsymbol{H}} \quad [H_{\theta\theta}]^{\boldsymbol{joint}} + \mathrm{H}_{k_\theta k_\theta}{}^{\boldsymbol{E}} + \mathrm{H}_{j_\theta j_\theta}{}^{\boldsymbol{H}}\right] \begin{Bmatrix} F_j^{\boldsymbol{joint}} \\ M_j^{\boldsymbol{joint}} \end{Bmatrix} \ldots$$

$$\ldots = \left[\mathrm{H}_{k_\theta k_x}{}^{\boldsymbol{E}} \quad \mathrm{H}_{k_\theta k_\theta}{}^{\boldsymbol{E}}\right] \begin{Bmatrix} F_k^{\boldsymbol{E}} \\ M_k^{\boldsymbol{E}} \end{Bmatrix} + \left[\mathrm{H}_{k_\theta s_x}{}^{\boldsymbol{E}} \quad \mathrm{H}_{k_\theta s_\theta}{}^{\boldsymbol{E}}\right] \begin{Bmatrix} F_s^{\boldsymbol{E}} \\ M_s^{\boldsymbol{E}} \end{Bmatrix} \ldots$$

$$\ldots - \left[\mathrm{H}_{j_\theta r_x}{}^{\boldsymbol{H}} \quad \mathrm{H}_{j_\theta r_\theta}{}^{\boldsymbol{H}}\right] \begin{Bmatrix} F_r^{\boldsymbol{H}} \\ M_r^{\boldsymbol{H}} \end{Bmatrix} - \left[\mathrm{H}_{j_\theta j_x}{}^{\boldsymbol{H}} \quad \mathrm{H}_{j_\theta j_\theta}{}^{\boldsymbol{H}}\right] \begin{Bmatrix} F_j^{\boldsymbol{H}} \\ M_j^{\boldsymbol{H}} \end{Bmatrix}$$

(2.31)

Now, combine Equations (2.30) and (2.31) and get the one given as:

`

$$\begin{bmatrix} [H_{xx}]^{\boldsymbol{joint}} + \mathrm{H}_{k_x k_x}{}^{\boldsymbol{E}} + \mathrm{H}_{j_x j_x}{}^{\boldsymbol{H}} & \mathrm{H}_{k_x k_\theta}{}^{\boldsymbol{E}} + \mathrm{H}_{j_x j_\theta}{}^{\boldsymbol{H}} \\ \mathrm{H}_{k_\theta k_x}{}^{\boldsymbol{E}} + \mathrm{H}_{j_\theta j_x}{}^{\boldsymbol{H}} & [H_{\theta\theta}]^{\boldsymbol{joint}} + \mathrm{H}_{k_\theta k_\theta}{}^{\boldsymbol{E}} + \mathrm{H}_{j_\theta j_\theta}{}^{\boldsymbol{H}} \end{bmatrix} \begin{Bmatrix} F_j^{\boldsymbol{joint}} \\ M_j^{\boldsymbol{joint}} \end{Bmatrix} = \ldots$$

$$\ldots + \begin{bmatrix} \mathrm{H}_{k_x k_x}{}^{\boldsymbol{E}} & \mathrm{H}_{k_x k_\theta}{}^{\boldsymbol{E}} \\ \mathrm{H}_{k_\theta k_x}{}^{\boldsymbol{E}} & \mathrm{H}_{k_\theta k_\theta}{}^{\boldsymbol{E}} \end{bmatrix} \begin{Bmatrix} F_k^{\boldsymbol{E}} \\ M_k^{\boldsymbol{E}} \end{Bmatrix} + \begin{bmatrix} \mathrm{H}_{k_x s_x}{}^{\boldsymbol{E}} & \mathrm{H}_{k_x s_\theta}{}^{\boldsymbol{E}} \\ \mathrm{H}_{k_\theta s_x}{}^{\boldsymbol{E}} & \mathrm{H}_{k_\theta s_\theta}{}^{\boldsymbol{E}} \end{bmatrix} \begin{Bmatrix} F_s^{\boldsymbol{E}} \\ M_s^{\boldsymbol{E}} \end{Bmatrix} \ldots$$

$$\ldots - \begin{bmatrix} \mathrm{H}_{j_x r_x}{}^{\boldsymbol{H}} & \mathrm{H}_{j_x r_\theta}{}^{\boldsymbol{H}} \\ \mathrm{H}_{j_\theta r_x}{}^{\boldsymbol{H}} & \mathrm{H}_{j_\theta r_\theta}{}^{\boldsymbol{H}} \end{bmatrix} \begin{Bmatrix} F_r^{\boldsymbol{H}} \\ M_r^{\boldsymbol{H}} \end{Bmatrix} - \begin{bmatrix} \mathrm{H}_{j_x j_x}{}^{\boldsymbol{H}} & \mathrm{H}_{j_x j_\theta}{}^{\boldsymbol{H}} \\ \mathrm{H}_{j_\theta j_x}{}^{\boldsymbol{H}} & \mathrm{H}_{j_\theta j_\theta}{}^{\boldsymbol{H}} \end{bmatrix} \begin{Bmatrix} F_j^{\boldsymbol{H}} \\ M_j^{\boldsymbol{H}} \end{Bmatrix}$$

(2.32)

Let's define $[Z]$ and rearrange the Equation (2.32) given as follows:

$$[Z] = [\alpha^{\boldsymbol{joint}}] + [\mathrm{H}_{kk}]^{\boldsymbol{E}} + [\mathrm{H}_{jj}]^{\boldsymbol{H}}$$

(2.33)

$$\begin{Bmatrix} F_j^{\boldsymbol{joint}} \\ M_j^{\boldsymbol{joint}} \end{Bmatrix} = [Z]^{-1} [\mathrm{H}_{kk}]^{\boldsymbol{E}} \begin{Bmatrix} F_k^{\boldsymbol{E}} \\ M_k^{\boldsymbol{E}} \end{Bmatrix} + [Z]^{-1} [\mathrm{H}_{ks}]^{\boldsymbol{E}} \begin{Bmatrix} F_s^{\boldsymbol{E}} \\ M_s^{\boldsymbol{E}} \end{Bmatrix} - [Z]^{-1} [\mathrm{H}_{jr}]^{\boldsymbol{H}} \begin{Bmatrix} F_r^{\boldsymbol{H}} \\ M_r^{\boldsymbol{H}} \end{Bmatrix} \ldots$$

$$\ldots - [Z]^{-1} [\mathrm{H}_{jj}]^{\boldsymbol{H}} \begin{Bmatrix} F_j^{\boldsymbol{H}} \\ M_j^{\boldsymbol{H}} \end{Bmatrix}$$

(2.34)

Now, to obtain the receptance matrix of the coupled HE assembly (***HE***) can be obtained by implementing Equation (2.34) to Equations (2.2) to (2.8) obtain the HE assembly's receptance matrix as follows:

$$\begin{Bmatrix} \boldsymbol{X}_r^{\boldsymbol{HE}} \\ \boldsymbol{X}_j^{\boldsymbol{HE}} \\ \boldsymbol{X}_k^{\boldsymbol{HE}} \\ \boldsymbol{X}_s^{\boldsymbol{HE}} \end{Bmatrix} = \begin{bmatrix} H_{rr}^{\boldsymbol{HE}} & H_{rj}^{\boldsymbol{HE}} & H_{rk}^{\boldsymbol{HE}} & H_{rs}^{\boldsymbol{HE}} \\ H_{jr}^{\boldsymbol{HE}} & H_{jj}^{\boldsymbol{HE}} & H_{jk}^{\boldsymbol{HE}} & H_{js}^{\boldsymbol{HE}} \\ H_{kr}^{\boldsymbol{HE}} & H_{kj}^{\boldsymbol{HE}} & H_{kk}^{\boldsymbol{HE}} & H_{ks}^{\boldsymbol{HE}} \\ H_{sr}^{\boldsymbol{HE}} & H_{sj}^{\boldsymbol{HE}} & H_{sk}^{\boldsymbol{HE}} & H_{ss}^{\boldsymbol{HE}} \end{bmatrix} \begin{Bmatrix} \boldsymbol{F}_r^{\boldsymbol{HE}} \\ \boldsymbol{F}_j^{\boldsymbol{HE}} \\ \boldsymbol{F}_k^{\boldsymbol{HE}} \\ \boldsymbol{F}_s^{\boldsymbol{HE}} \end{Bmatrix}$$

(2.35)

$$\begin{Bmatrix} \boldsymbol{X}_r^{\boldsymbol{HE}} \\ \boldsymbol{X}_j^{\boldsymbol{HE}} \\ \boldsymbol{X}_k^{\boldsymbol{HE}} \\ \boldsymbol{X}_s^{\boldsymbol{HE}} \end{Bmatrix} = \begin{bmatrix} [\mathrm{H}_{rr}]^{\boldsymbol{H}} - [H_{rj}]^{\boldsymbol{H}} [Z]^{-1} [H_{jr}]^{\boldsymbol{H}} & [\mathrm{H}_{rj}]^{\boldsymbol{H}} - [H_{rj}]^{\boldsymbol{H}} [Z]^{-1} [H_{jj}]^{\boldsymbol{H}} \\ [\mathrm{H}_{jr}]^{\boldsymbol{H}} - [H_{jj}]^{\boldsymbol{H}} [Z]^{-1} [H_{jr}]^{\boldsymbol{H}} & [\mathrm{H}_{jj}]^{\boldsymbol{H}} - [H_{jj}]^{\boldsymbol{H}} [Z]^{-1} [H_{jj}]^{\boldsymbol{H}} \\ [\mathrm{H}_{kk}]^{\boldsymbol{E}} [Z]^{-1} [H_{jr}]^{\boldsymbol{H}} & [\mathrm{H}_{kk}]^{\boldsymbol{E}} [Z]^{-1} [H_{jj}]^{\boldsymbol{H}} \\ [\mathrm{H}_{sk}]^{\boldsymbol{E}} [Z]^{-1} [H_{jr}]^{\boldsymbol{H}} & [\mathrm{H}_{sk}]^{\boldsymbol{E}} [Z]^{-1} [H_{jj}]^{\boldsymbol{H}} \end{bmatrix} \dots$$

$$\dots \begin{bmatrix} [\mathrm{H}_{rj}]^{\boldsymbol{H}} [Z]^{-1} [\mathrm{H}_{kk}]^{\boldsymbol{E}} & [\mathrm{H}_{rj}]^{\boldsymbol{H}} [Z]^{-1} [\mathrm{H}_{ks}]^{\boldsymbol{E}} \\ [H_{jj}]^{\boldsymbol{H}} [Z]^{-1} [\mathrm{H}_{kk}]^{\boldsymbol{E}} & [H_{jj}]^{\boldsymbol{H}} [Z]^{-1} [\mathrm{H}_{ks}]^{\boldsymbol{E}} \\ [\mathrm{H}_{kk}]^{\boldsymbol{E}} - [\mathrm{H}_{kk}]^{\boldsymbol{E}} [Z]^{-1} [\mathrm{H}_{kk}]^{\boldsymbol{E}} & [\mathrm{H}_{ks}]^{\boldsymbol{E}} - [\mathrm{H}_{kk}]^{\boldsymbol{E}} [Z]^{-1} [\mathrm{H}_{ks}]^{\boldsymbol{E}} \\ [\mathrm{H}_{sk}]^{\boldsymbol{E}} - [\mathrm{H}_{sk}]^{\boldsymbol{E}} [Z]^{-1} [\mathrm{H}_{kk}]^{\boldsymbol{E}} & [\mathrm{H}_{ss}]^{\boldsymbol{E}} - [\mathrm{H}_{sk}]^{\boldsymbol{E}} [Z]^{-1} [\mathrm{H}_{ks}]^{\boldsymbol{E}} \end{bmatrix} \begin{Bmatrix} \boldsymbol{F}_r^{\boldsymbol{HE}} \\ \boldsymbol{F}_j^{\boldsymbol{HE}} \\ \boldsymbol{F}_k^{\boldsymbol{HE}} \\ \boldsymbol{F}_s^{\boldsymbol{HE}} \end{Bmatrix}$$

(2.36)

where $\boldsymbol{X}$ holds translational and rotational displacements, and $\boldsymbol{F}$ contains both force and moment vectors. The details of the matrixes in Equation (2.35) are as follows:

$$[H_{rr}^{\boldsymbol{HE}}] = [\mathrm{H}_{rr}]^{\boldsymbol{H}} - [H_{rj}]^{\boldsymbol{H}} [Z]^{-1} [H_{jr}]^{\boldsymbol{H}} \tag{2.37}$$

$$[H_{rj}^{\boldsymbol{HE}}] = [\mathrm{H}_{rj}]^{\boldsymbol{H}} - [H_{rj}]^{\boldsymbol{H}} [Z]^{-1} [H_{jj}]^{\boldsymbol{H}} \tag{2.38}$$

$$[H_{jr}^{\boldsymbol{HE}}] = [\mathrm{H}_{jr}]^{\boldsymbol{H}} - [H_{jj}]^{\boldsymbol{H}} [Z]^{-1} [H_{jr}]^{\boldsymbol{H}} \tag{2.39}$$

$$[H_{jj}^{\boldsymbol{HE}}] = [\mathrm{H}_{jj}]^{\boldsymbol{H}} - [H_{jj}]^{\boldsymbol{H}} [Z]^{-1} [H_{jj}]^{\boldsymbol{H}} \tag{2.40}$$

$$[H_{rk}^{\boldsymbol{HE}}] = [\mathrm{H}_{rj}]^{\boldsymbol{H}} [Z]^{-1} [\mathrm{H}_{kk}]^{\boldsymbol{E}} \tag{2.41}$$

$$[H_{rs}^{\boldsymbol{HE}}] = [\mathrm{H}_{rj}]^{\boldsymbol{H}} [Z]^{-1} [\mathrm{H}_{ks}]^{\boldsymbol{E}} \tag{2.42}$$

$$[H_{jk}^{\boldsymbol{HE}}] = [H_{jj}]^{\boldsymbol{H}} [Z]^{-1} [\mathrm{H}_{kk}]^{\boldsymbol{E}} \tag{2.43}$$

`

$$\left[H_{js}^{\boldsymbol{HE}}\right] = \left[H_{jj}\right]^{\boldsymbol{H}}[Z]^{-1}[\mathrm{H}_{ks}]^{\boldsymbol{E}} \tag{2.44}$$

$$\left[H_{kr}^{\boldsymbol{HE}}\right] = [\mathrm{H}_{kk}]^{\boldsymbol{E}}\,[Z]^{-1}\left[H_{jr}\right]^{\boldsymbol{H}} \tag{2.45}$$

$$\left[H_{kj}^{\boldsymbol{HE}}\right] = [\mathrm{H}_{kk}]^{\boldsymbol{E}}\,[Z]^{-1}\left[H_{jj}\right]^{\boldsymbol{H}} \tag{2.46}$$

$$[H_{sr}^{\boldsymbol{HE}}] = [\mathrm{H}_{sk}]^{\boldsymbol{E}}\,[Z]^{-1}\left[H_{jr}\right]^{\boldsymbol{H}} \tag{2.47}$$

$$\left[H_{sj}^{\boldsymbol{HE}}\right] = [\mathrm{H}_{sk}]^{\boldsymbol{E}}\,[Z]^{-1}\left[H_{jj}\right]^{\boldsymbol{H}} \tag{2.48}$$

$$\left[H_{kk}^{\boldsymbol{HE}}\right] = [\mathrm{H}_{kk}]^{\boldsymbol{E}} - [\mathrm{H}_{kk}]^{\boldsymbol{E}}\,[Z]^{-1}[\mathrm{H}_{kk}]^{\boldsymbol{E}} \tag{2.49}$$

$$\left[H_{ks}^{\boldsymbol{HE}}\right] = [\mathrm{H}_{ks}]^{\boldsymbol{E}} - [\mathrm{H}_{kk}]^{\boldsymbol{E}}\,[Z]^{-1}[\mathrm{H}_{ks}]^{\boldsymbol{E}} \tag{2.50}$$

$$\left[H_{sk}^{\boldsymbol{HE}}\right] = [\mathrm{H}_{sk}]^{\boldsymbol{E}} - [\mathrm{H}_{sk}]^{\boldsymbol{E}}\,[Z]^{-1}[\mathrm{H}_{kk}]^{\boldsymbol{E}} \tag{2.51}$$

$$[H_{ss}^{\boldsymbol{HE}}] = [\mathrm{H}_{ss}]^{\boldsymbol{E}} - [\mathrm{H}_{sk}]^{\boldsymbol{E}}\,[Z]^{-1}[\mathrm{H}_{ks}]^{\boldsymbol{E}} \tag{2.52}$$

2.2 Contact Dynamics Identification via Inverse Structural Modification Method

2.2.1 Structural Modification Method (Özgüven, 1990) by Matrix Inversion Method (Özgüven, 1987)

The Matrix Inversion Method (MIM) was first proposed by Özgüven [27]. This method is aimed to obtain the receptance matrix of the non-proportionally, locally damped structure through their undamped counterparts. Then, this method is applied

as the general modification method in addition to damping properties, So the modified system receptance matrixes are obtained by their unmodified counterparts.[28]

Consider a system that has a mass matrix $[M]$, stiffness matrix,$[K]$, and structural damping $[H]$. The system excited with a harmonic force, $\{F\}$ with excitation frequency ω. So, the equation of motion of the system can be written as follows:

$$[M]\{\ddot{x}\} + i[H]\{x\} + [K]\{x\} = \{F\} \tag{2.53}$$

$$([K] - \omega^2[M] + i[H])\{x\} = \{F\} \tag{2.54}$$

where $\{x\}$ is the vector of generalized coordinates.

The receptance matrix of the system, $[\alpha]$ can be written as the inverse of the coefficient of $\{x\}$ in Equation (2.54)

$$[\alpha] = ([K] - \omega^2[M] + i[H])^{-1} \tag{2.55}$$

If the system is modified such that:

$$[M] \to [M] + [\Delta M] \qquad [K] \to [K] + [\Delta K] \qquad [H] \to [H] + [\Delta H]$$

Let $[\beta]$ is the receptance of the modified systems receptance matrix, and it can be written in terms of its unmodified equivalent as follows:

$$[\beta] = (([K] + [\Delta K]) - \omega^2([M] + [\Delta M]) + i([H] + [\Delta H]))^{-1} \tag{2.56}$$

$$[\beta]^{-1} = [\alpha]^{-1}\,([\Delta K] - \omega^2 + [\Delta M] + i + [\Delta H])) \tag{2.57}$$

`

Define $[D]$ as the dynamic stiffness matrix of the modified part, which is given as

$$[D] = [\Delta K] - \omega^2 + [\Delta M] + i + [\Delta H] \tag{2.58}$$

Now, put Equation (2.58) into Equation (2.57)

$$[\beta]^{-1} = [\alpha]^{-1}\,[D] \tag{2.59}$$

Let's pre-multiply Equation (2.59) by $[\alpha]$ and post-multiply by $[\beta]$, and obtain $[\beta]$ as follows:

$$[\beta] = ([I] + [\alpha]\,[D])^{-1}[\alpha] \tag{2.60}$$

As stated in the studies [27] and [28], Equation (2.60) requires the inversion of large matrixes. To take the advantage of the SMM, consider local modifications:

$$[D] = \begin{bmatrix} [D_{mm}] & 0 \\ 0 & 0 \end{bmatrix} \tag{2.61}$$

where m represents the coordinates in which the modifications are done.

If Equation (2.61) is inserted in Equation (2.60), the modified system's receptances can be found as follows after several manipulations. The details of the intermediate steps can be found in [28].

$$[\beta_{mm}] = ([I] + [\alpha_{mm}]\,[D_{mm}])^{-1}[\alpha_{mm}] \tag{2.62}$$

$$[\beta_{mu}] = ([I] + [\alpha_{mm}]\,[D_{mm}])^{-1}[\alpha_{mu}] \tag{2.63}$$

$$[\beta_{um}] = [\alpha_{um}] - [\alpha_{um}][D_{mm}][\beta_{mm}] \tag{2.64}$$

$$[\beta_{uu}] = [\alpha_{uu}] - [\alpha_{um}][D_{mm}][\beta_{mu}] \tag{2.65}$$

where *u* is the unmodified coordinates of the system.

`

2.2.2 Inverse Structural Modification Method (Özgüven & Tekin, 2020)

The Inverse Structural Modification Method (ISMM) was first applied by Özgüven et al. [18] to identify the complex stiffness matrix of the bolted connection in in-line beam assembly. The ISMM method utilizes the SMM in reverse order. The studies are conducted through the bolted in-line beam configuration. The bolt is modeled as a complex stiffness matrix. In the application of the ISMM, two models are created with different complex stiffness matrices representing the bolted connection.

Initially, the first model is obtained with an estimated complex stiffness matrix, and the receptance matrix of the assembly is represented as $[\alpha]$. Then, the second model, which is the measured model with an unknown complex stiffness matrix, is named, $[\beta]$. Furthermore, the modification is assumed only in joint coordinates where the complex stiffness matrix is defined. The modification matrix that shows the difference between the measured and estimated model is calculated by SMM by MIM.

The obtained modification matrix is then added to the estimated complex stiffness matrix to find the equivalent complex stiffness matrix, which enables the identified systems to have the same dynamics (mode and mode shapes) as their measured counterparts.

To obtain the modification matrix $[D_{mm}]$, recall the Equation (2.60):

$$[\beta] = ([I] + [\alpha]\,[D])^{-1}[\alpha] \tag{2.66}$$

$$[\alpha] = [\beta] + [\alpha][D][\beta] \tag{2.67}$$

$$\begin{bmatrix}[\alpha_{mm}] & [\alpha_{mu}]\\ [\alpha_{um}] & [\alpha_{uu}]\end{bmatrix} = \begin{bmatrix}[\beta_{mm}] & [\beta_{mu}]\\ [\beta_{um}] & [\beta_{uu}]\end{bmatrix}\begin{bmatrix}[\alpha_{mm}] & [\alpha_{mu}]\\ [\alpha_{um}] & [\alpha_{uu}]\end{bmatrix}\dots \dots\begin{bmatrix}[D_{mm}] & 0\\ 0 & 0\end{bmatrix}\begin{bmatrix}[\beta_{mm}] & [\beta_{mu}]\\ [\beta_{um}] & [\beta_{uu}]\end{bmatrix} \tag{2.68}$$

`

$$\begin{bmatrix} [\alpha_{mm}] & [\alpha_{mu}] \\ [\alpha_{um}] & [\alpha_{uu}] \end{bmatrix} = \begin{bmatrix} [\beta_{mm}] & [\beta_{mu}] \\ [\beta_{um}] & [\beta_{uu}] \end{bmatrix} + \begin{bmatrix} [\alpha_{mm}][D_{mm}][\beta_{mm}] & \cdots \\ \cdots & [\alpha_{mm}][D_{mm}][\beta_{mu}] \\ [\alpha_{um}][D_{mm}][\beta_{mm}] & \\ & [\alpha_{um}][D_{mm}][\beta_{mu}] \end{bmatrix}$$

(2.69)

The receptance matrix of the modified coordinates in the assumed model is as follows:

$$[\alpha_{mm}] = [\beta_{mm}] + [\beta_{mm}][D_{mm}][\beta_{mm}]$$

(2.70)

$$[\alpha_{mm}] - [\beta_{mm}] = [\beta_{mm}][D_{mm}][\beta_{mm}]$$

(2.71)

To obtain a modification matrix, $[D_{mm}]$ in modified coordinates, pre-multiply Equation (2.71) by $[\alpha_{mm}]^{-1}$ then post- multiply by $[\beta_{mm}]^{-1}$. Then $[D_{mm}]$ can be found as follows:

$$[D_{mm}] = [\alpha_{mm}]^{-1}([\alpha_{mm}] - [\beta_{mm}])[\beta_{mm}]^{-1}$$

(2.72)

As the modification matrix's equation shows, the matrix calculations are now limited to the modified coordinates, eliminating the inverse calculation of the matrix representing the whole system's dynamics.

`

2.2.3 Contact Dynamics Identification of The Holder-Extension Assembly via ISMM Method

To apply the ISMM for the HE assembly, recall the coupled HE assembly in Figure 2.2. As indicated in Equation (2.72) assumed model, $[\alpha_{mm}]$ and a measured model, $[\beta_{mm}]$ FRFs at the contact faces between the H and E is required.

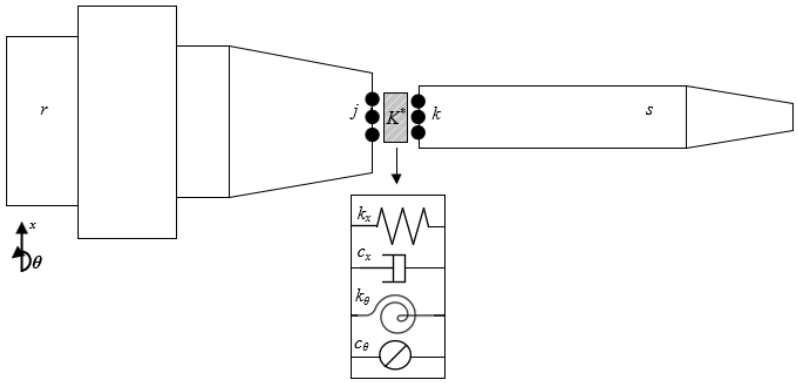


Figure 2.2 Coupled HE assembly

The assumed model, $[\alpha_{mm}]$ includes only contact faces, j and k, FRFs are calculated through FE simulations by assumed complex stiffness matrix, $[K_1^*]$ which is taken from the literature. The superscript α represents the assumed coupled model in Equation (2.73).

$$[\alpha_{mm}] = \begin{bmatrix} [\alpha_{jj}{}^{a}] & [\alpha_{jk}{}^{a}] \\ [\alpha_{kj}{}^{a}] & [\alpha_{kk}{}^{a}] \end{bmatrix} \tag{2.73}$$

The actual (measured) model, $[\beta_{mm}]$ includes only contact faces, j and k, FRFs are obtained by experiment. It is assumed that the actual HE assembly has the complex stiffness value of $[K_2^*]$. The superscript β stands for the actual coupled model in Equation (2.74).

$$[\beta_{mm}] = \begin{bmatrix} [{\beta_{jj}}^{\beta}] & [{\beta_{jk}}^{\beta}] \\ [{\beta_{kj}}^{\beta}] & [{\beta_{kk}}^{\beta}] \end{bmatrix}$$

(2.74)

Then, assumed and the actual models FRFs are utilized in Equation (2.72), the dynamics stiffness matrix of the modified complex stiffness matrix can be written as follows:

$$[D_{mm}] = \begin{bmatrix} j\ coord. & \Delta \\ \Delta & j\ coord. \end{bmatrix}$$

(2.75)

To identify the $[K_2^*]$, cross elements that apply the complex stiffness matrix defined between the contact faces (see Equation (2.14)) Δ of the $[D_{mm}]$ should be added to $[K_1^*]$, so $[K_2^*]$ identified as

$$[K_2^*] = [K_1^*] + \Delta$$

(2.76)

It should be noted that the dimension of the matrixes is the same as the contact degree of freedom. In this study, the contact dynamics are modeled through two faces where each has 2 DOF, so all the matrixes used in modification matrix identification are 4*4.

`

CHAPTER 3

IDENTIFICATION OF COMPLEX STIFFNESS MATRIX OF THE HOLDER EXTENSION INTERFACE- NUMERICAL STUDY

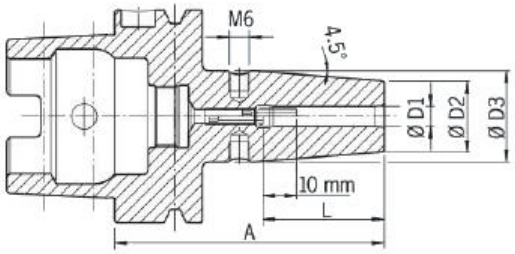
3.1 Objective and Problem Description

In this section, the application of the ISMM method for the identification of the HE interface is done by FE simulation. Some assumptions are made in the beginning to apply the method for the HE assembly. The ISMM method, detailed in Section 2.2.2, uses joint dynamics identification through a single point on each contact face. However, the holder (HAIMER A63.140.20) and extension (HAIMER 77.202.08) are assembled using shrink fit, where the extension has an inserted part in the holder (Figure 3.3). The holder's and the extension's technical properties are also given in Figure 3.1 and Figure 3.2, respectively.

The contact is the circular face contact between the holder and the extension through the outer face of the inserted part. As a first assumption, the HE assembly is assumed to be joined via the single face illustrated in Figure 3.4. The FE simulation is built on that assumption. The FE simulation is created using ANSYS Inc. software. The details of the ANSYS Finite Element Model (FEM) are covered in the following sections.

The effects of noise on the obtained joint dynamics results are investigated following the first results of the ISMM method. In the investigation, the simulation results are polluted with different noise levels. The identification procedures are then repeated with polluted data. Finally, the noise effects in the results are shared and compared to their unpolluted counterparts.

`



$$Ø_{D1} = 20\ mm$$

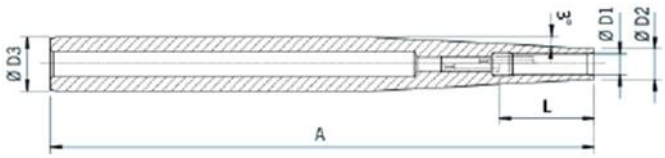
$$Ø_{D2} = 33\ mm$$

$$Ø_{D3} = 42\ mm$$

$$L = 52\ mm$$

$$A = 100\ mm$$

Figure 3.1 Technical properties of the holder [29]



$$Ø_{D1} = 8\ mm$$

$$Ø_{D2} = 14\ mm$$

$$Ø_{D3} = 20\ mm$$

$$L = 34\ mm$$

$$A = 160\ mm$$

Figure 3.2 Technical properties of the extension [30]

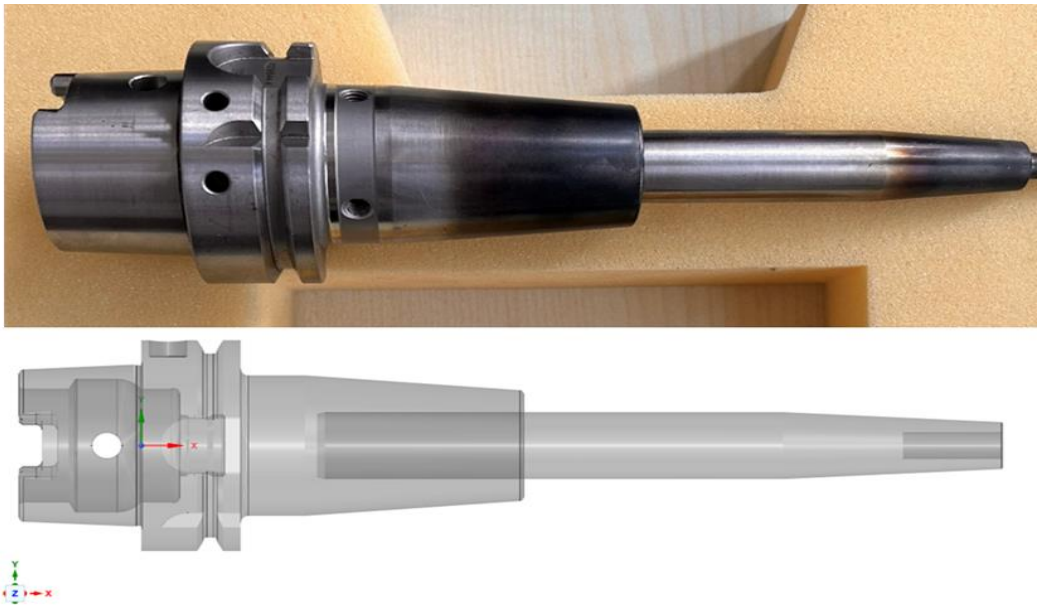


Figure 3.3. Holder-Extension Assembly

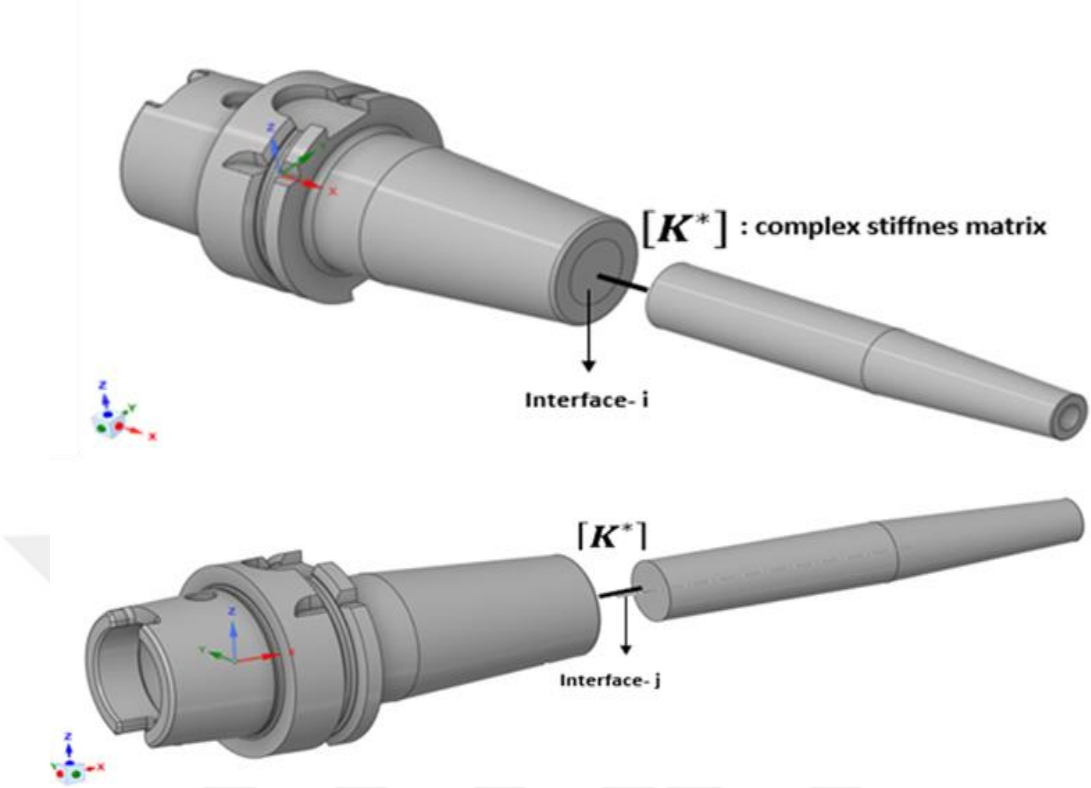


Figure 3.4 Connection dynamics face of the Holder-Extension assembly

3.2 2 DOF Linear Spring- Dashpot Model

As discussed in Section 2.2, to accurately identify the complex stiffness matrix of the HE interfaces using ISMM, it is essential to have two distinct models of the assembly: assumed and actual. This chapter relies on the numerical results obtained from ANSYS, Inc. 2022 R2 FE simulations. The comprehensive description of the modeling procedures and the results are detailed in the following sections.

To begin generating an FE model, the 3D CAD model of the HE assembly is cleared without making significant modifications to the assembly's modes and mode shapes. It is assumed in this analysis that the holder and extension are connected by a single circular interface, as shown in Figure 3.5. Two deformable remote points (RBE3 elements [31]) are constructed at interfaces *i* and *j*. The remote points only have

degrees of freedom in Z and RotY directions because the identification of interface dynamics is only executed in those axes.

In the analysis model, faces *i* and *j* connect the holder and extension (Figure 3.5). Two Combin14 [31] elements define the contact dynamics in both axes. Complex stiffness matrix properties, stiffness, and viscous damping are adopted from the study in [32], and stiffness and damping properties are defined for the contact elements (Table 3-1). In Table 3-1, there are two sets of complex stiffness matrixes named assumed-α and actual-β. The assumed model-α is the model that has guessed stiffness and damping values other than actual values, and it is required in the ISMM. The details of using the assumed model are in detail in Section. 2.1. The actual model-β is the model that represents the actual contact face dynamics of the HE assembly.

Both the tool holder and extension are made of steel. The material properties of the steel employed in the simulation are also given in Table 3-2.

The assembly has meshed ten node tetrahedral solid elements named TET10 (Figure 3.6). Several sensitivity analyses are done to decide the mesh size. The results of those analyses are evaluated in terms of the convergence of the first and second natural frequencies, and in the end, the mesh is generated, as given in Figure 3.6. The element quality matrix of the generated mesh is also shared in Figure 3.6. This graph shows the element quality of the meshed body from zero to one. As the element's quality increases, the model becomes more reliable. In this model, the element quality is enough to get reliable results.

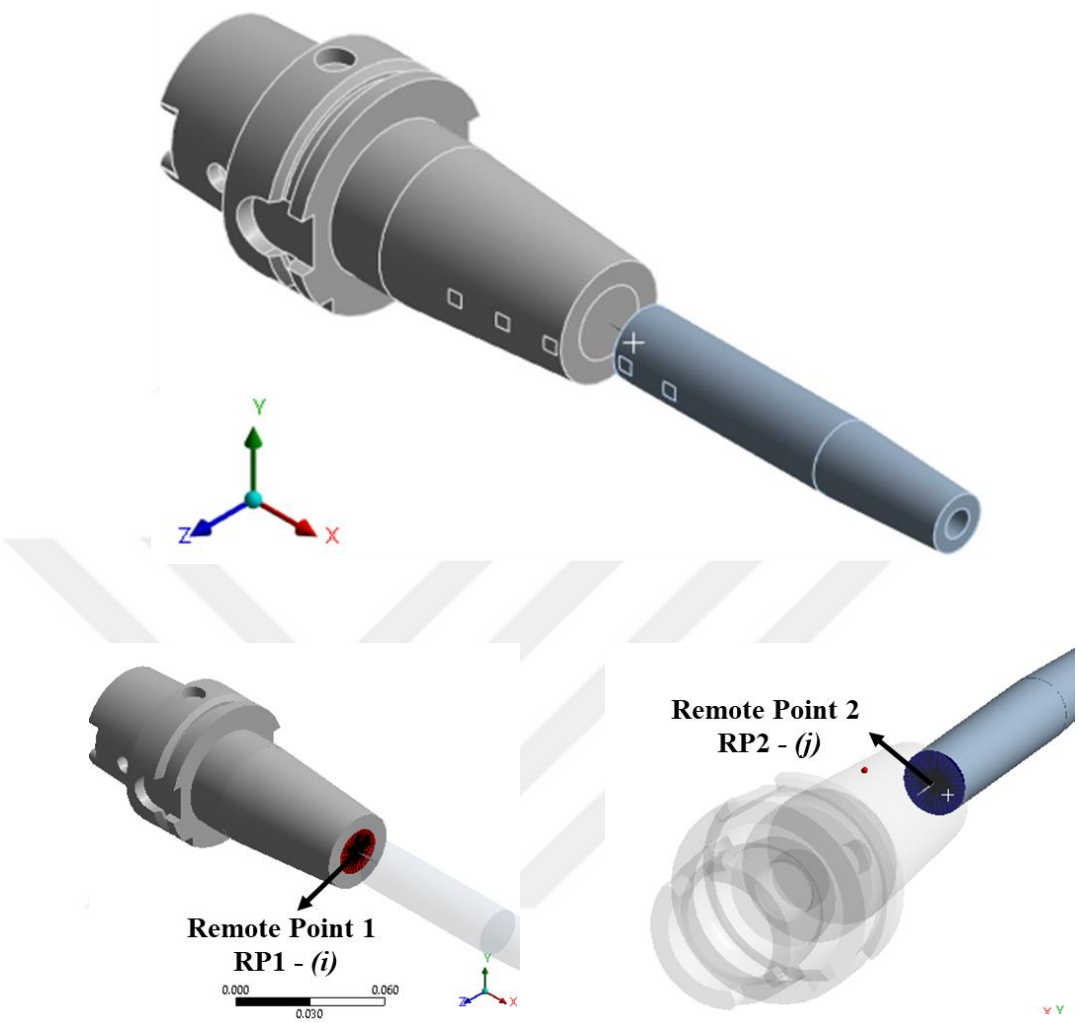


Figure 3.5 Holder-Extension assembly 3D ANSYS FE model and spring definition points

`

Table 3-1 Defined stiffness and damping properties representing contact dynamics

	Stiffness and Damping Properties	Assumed- α Model	Actual- β Model
Stiffness	k_{Fz} (N/m)	1.00E+08	2.40E+08
	$k_{M\theta y}$ (N.m/rad)	3.00E+05	4.50E+05
Damping	c_{Fz} (N.s/m)	47	57
	$c_{M\theta y}$ (N.m.s/rad)	3	5
Constant Structural Damping		0.001	0.001

Table 3-2 Mechanical properties of holder and extension

	Material Properties		
	Elastic Modulus- E (GPa)	**Density- ρ ($kg.m^{-3}$)**	**Poisson's Ratio -ν**
Holder Extension (Steel)	200	7850	0.33

`

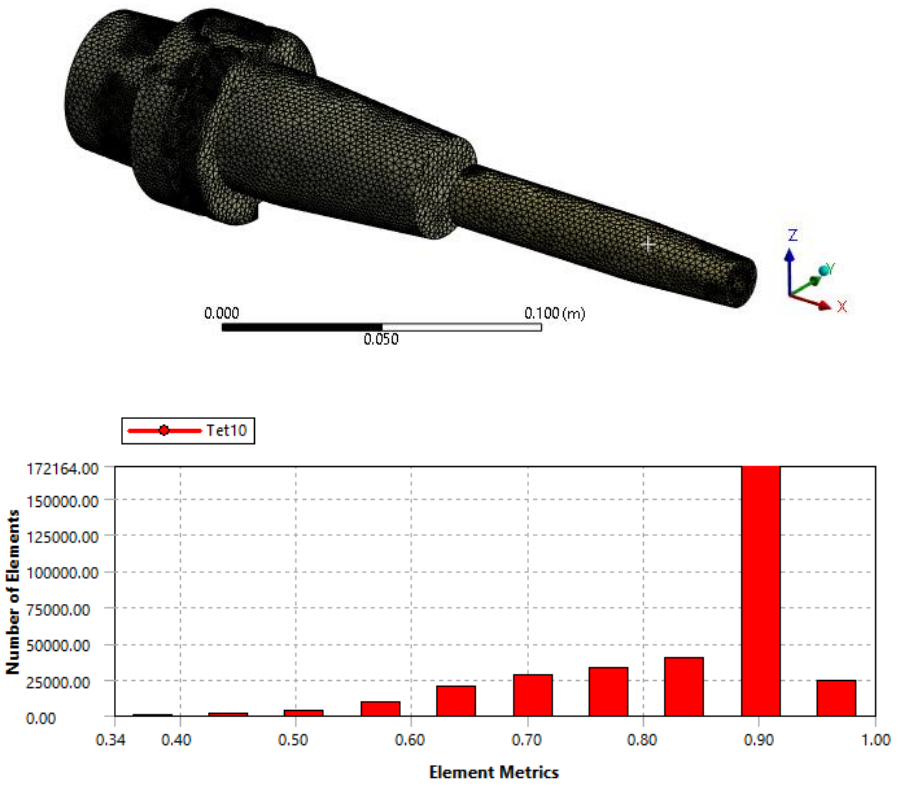


Figure 3.6 Mesh (upper) and mesh quality matrix (lower) of the assembly

After completing the FE model, a free- free modal analysis is conducted. To derive complete 4*4 joint FRF matrices of RP1 (*i*) and RP2 (*j*), Reduced Damped Modal Analysis (QR Damped in ANSYS, Inc.) is employed first, and then Mode Superposition Harmonic Analysis is run to obtain FRF matrices of the assumed and actual models. Two harmonic analyses are employed for each contact face for the Z and RotY axes. For the Z axis and RotY axes' analyses, 1 N force and 1 N/m moment are applied, respectively.

Figure 3.7 and Figure 3.8 show the modes and mode shapes of the assumed and actual models, named α and β, respectively. The obtained FRFs are also shared in Figure 3.9, where the deviation between the FRFs belonging to the assumed and actual models becomes clear. After all FRF results are gathered, FRF matrices are created as described as follows:

$$[H_{assumed}(\omega)] = [H_{\alpha}(\omega)] = \begin{bmatrix} [H_{ii}{}^{a}] & [H_{ij}{}^{a}] \\ [H_{ji}{}^{a}] & [H_{jj}{}^{a}] \end{bmatrix} \tag{3.1}$$

$$[H_{actual}(\omega)] = [H_{\beta}(\omega)] = \begin{bmatrix} [H_{ii}{}^{r}] & [H_{ij}{}^{r}] \\ [H_{ji}{}^{r}] & [H_{jj}{}^{r}] \end{bmatrix} \tag{3.2}$$

where

$$[H_{ii}{}^{?}] = \begin{bmatrix} H_{i_z i_z}{}^{?} & H_{i_z i_{RotY}}{}^{?} \\ H_{i_{RotY} i_z}{}^{?} & H_{i_{RotY} i_{RotY}}{}^{?} \end{bmatrix} \tag{3.3}$$

$$[H_{ij}{}^{?}] = \begin{bmatrix} H_{i_z j_z}{}^{?} & H_{i_z j_{RotY}}{}^{?} \\ H_{i_{RotY} j_z}{}^{?} & H_{i_{RotY} j_{RotY}}{}^{?} \end{bmatrix} \tag{3.4}$$

$$[H_{ji}{}^{?}] = ([H_{ij}{}^{?}])^{T} \tag{3.5}$$

$$[H_{jj}{}^{?}] = \begin{bmatrix} H_{j_z j_z}{}^{?} & H_{j_z j_{RotY}}{}^{?} \\ H_{j_{RotY} j_z}{}^{?} & H_{j_{RotY} j_{RotY}}{}^{?} \end{bmatrix} \tag{3.6}$$

`

where

? :	Represents the model α or β
$H_{i_z i_z}$:	Direct translational FRF at surface i (or j)
$H_{i_z i_{RotY}}$:	Force- Moment receptance at surface i (or j)
$H_{i_{RotY} i_{RotY}}$:	Direct rotational FRF at surface i
$H_{i_z j_z}$:	Cross translational FRF between the surface i and j
$H_{i_z j_{RotY}}$:	Force- Moment receptance between the surface i and j
$H_{i_{RotY} j_z}$:	Moment- Force receptance between the surface i and j
$H_{i_{RotY} j_{RotY}}$:	Cross rotational FRF between the surface i and j

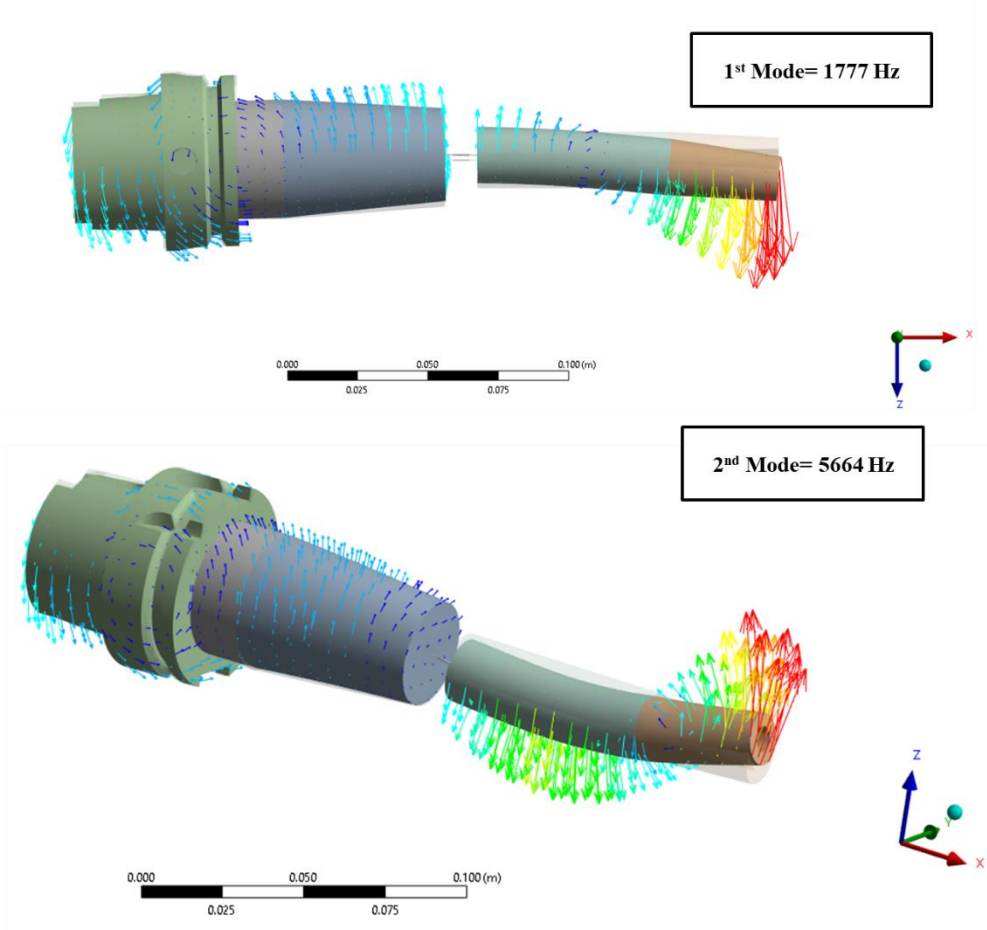


Figure 3.7 1st and 2nd mode shape with assumed complex stiffness matrix, $[K_{assumed}{}^{*}(\omega)]$

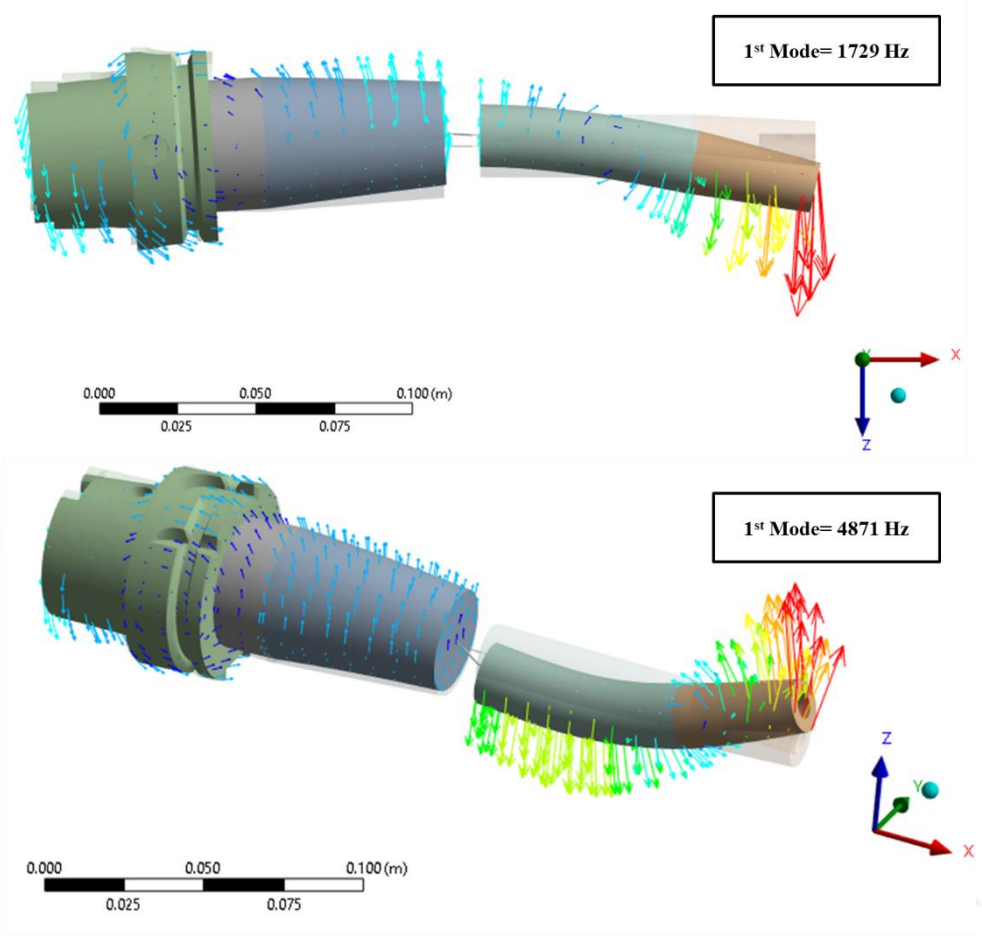


Figure 3.8 1st and 2nd mode shape with actual complex stiffness matrix, $[K_{actual}{}^{*}(\omega)]$

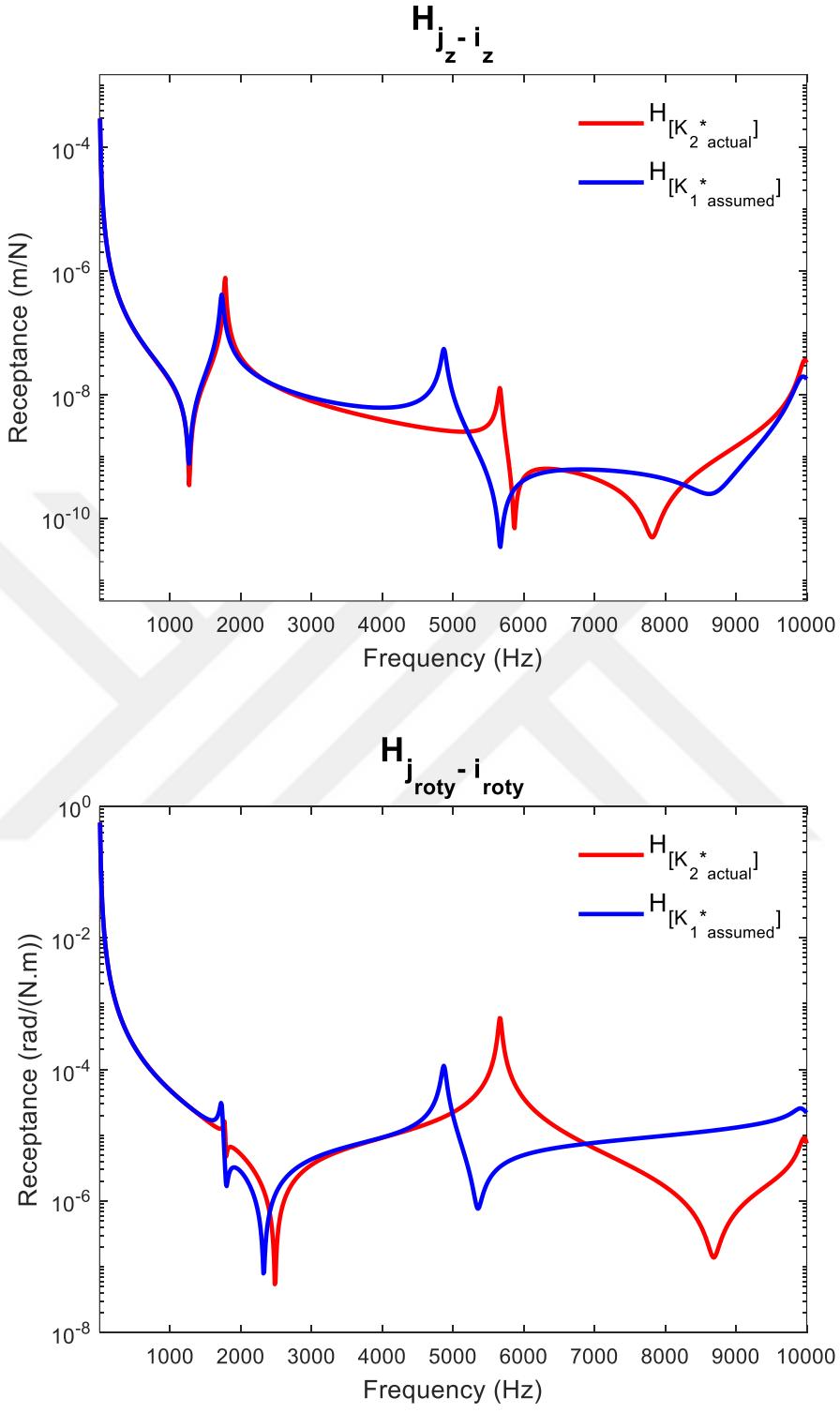


Figure 3.9 Cross translational (upper) and rotational (lower) FRFs between RP1- *i* and RP2- *j*

`

3.3 Identification of Contact Dynamics Parameters by ISMM

The identification ranges must be determined as an initial step to use ISMM (Equation (2.72)). Sensitivity analyses are performed to determine the ranges for each DOF. In those analyses, various stiffness values associated with each DOF have been used, and the cross-translational and rotational FRFs for the points RP1 and RP2 are obtained. For the sensitivity analysis of the Z direction, stiffness values that are approximately 80% lower, 60% lower, and 70% higher than the actual stiffness value are chosen. As for the analysis of the RotY direction, the stiffness values employed for range identification are approximately 80% lower, 70% lower, and 80% higher than the actual stiffness value. Figure 3.10 shows the FRF results for the different stiffness values in the Z and RotY directions. After identification analysis in Figure 3.10, it has become clear that stiffness in the Z direction has more impact on the 2nd natural frequency, whereas stiffness in the RotY direction influences the 1st natural frequency.

Based on the sensitivity analysis shown in Figure 3.10, sensitivity regions for the contact parameters are defined as shown in Table 3-3. Those ranges are determined by picking frequency ranges where the FRFs in Figure 3.10 deviate from each other.

Table 3-3 Sensitivity Ranges

Stiffness Direction	Sensitivity Range
$\mathbf{k_{Fz}}$	1300-5000 Hz
$\mathbf{k_{M\theta y}}$	1450-5000 Hz

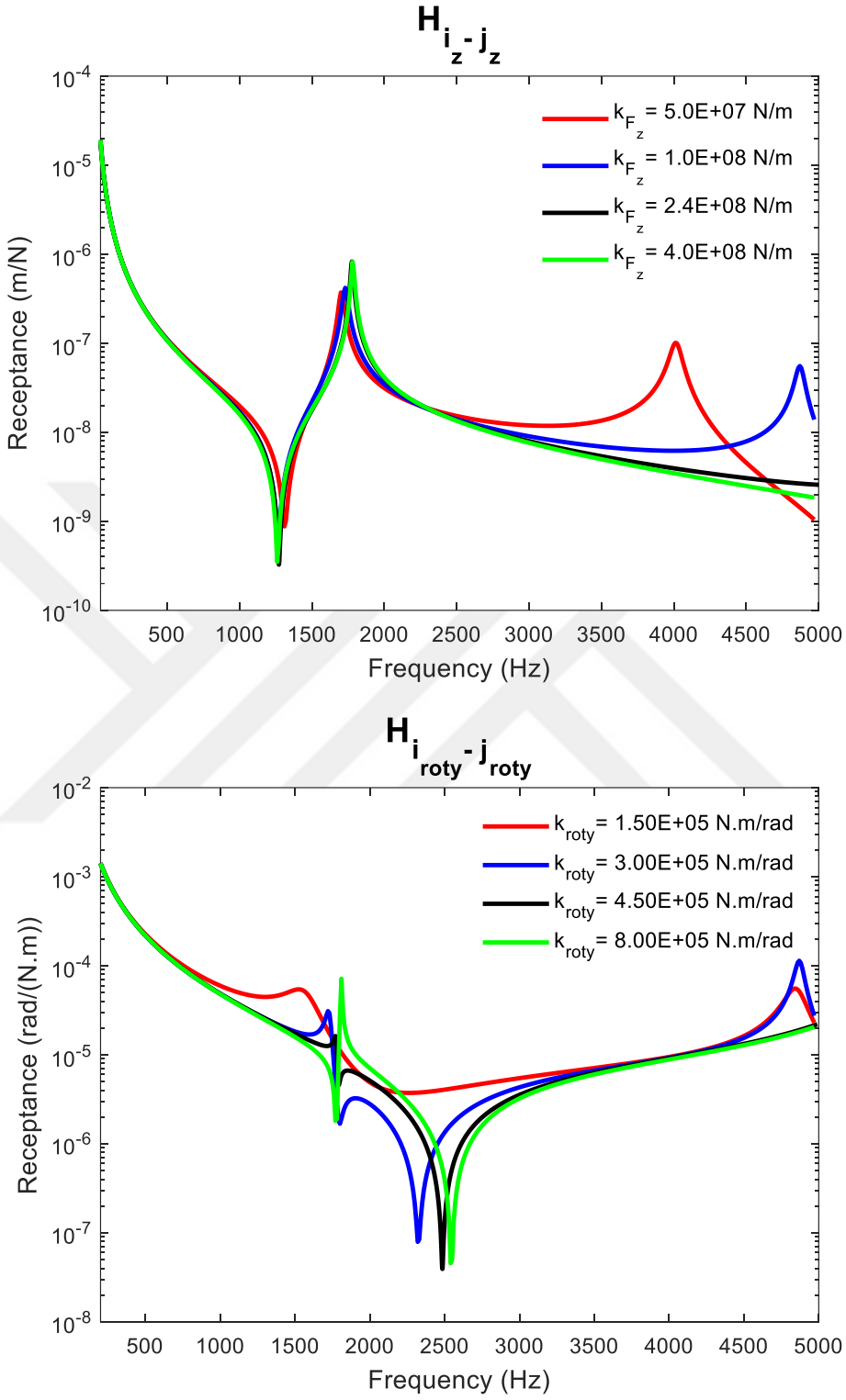


Figure 3.10 Cross FRFs in *Z* and *RotY* directions for different stiffness values

`

Stiffness and damping values for Z and RotY directions are identified by applying ISMM in the specified ranges. The identified stiffness and damping values are shown in Figure 3.11 to Figure 3.14, and summarized in Table 3-4. However, there are unexpected spikes when the identified stiffness and damping values are examined, as seen in Figure 3.11 to Figure 3.14. FRF matrices that belong to assumed and actual models are examined, and it is seen that the RCOND (Reciprocal condition number in MATLAB) numbers are small and lead to singularities in matrix inversion. To eliminate that issue, although pseudo-inverses of the matrices are calculated, those spikes could not be prevented entirely. Without getting more into detail in the numerical calculations done by MATLAB, the unexpected results, which can be seen in the box in the related figures, are extracted from the identification calculations. Following the extraction of unrealistic results, the identified stiffness values are calculated by taking the mean of the stiffness values in the identification ranges. The means of those stiffness values for Z and RotY directions are given in the lower part of Figure 3.11 and Figure 3.12, respectively. They are also compared to assumed and actual stiffness values to see how close the identified stiffness values are to the desired ones. The identified stiffness values in those graphs are calculated by adding the mean of the related stiffness values to their actual counterparts. The absolute errors of each stiffness value are calculated and shared in Table 3-4 to convert the accuracy of the identification results into a metric. It is seen that the errors in the identified stiffness values are at the 10% level. However, it is essential to note that to determine whether these errors are acceptable, a comparison between the newly identified and the actual models' FRFs is necessary. These comparisons will be conducted in the subsequent sections, allowing for a comprehensive evaluation of the effectiveness of the ISMM in contact dynamics identification.

`

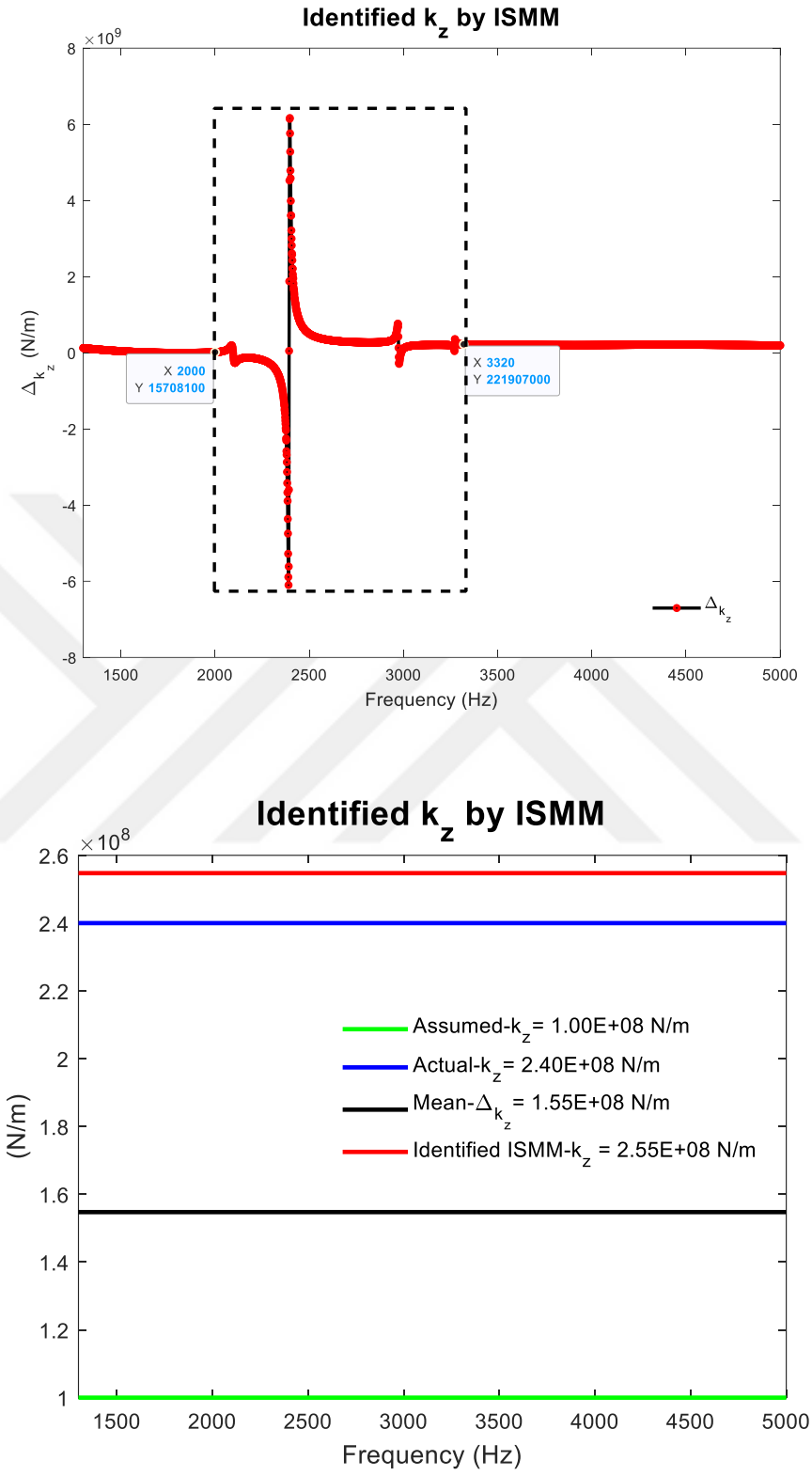


Figure 3.11 Identified stiffness value of k_Z

`

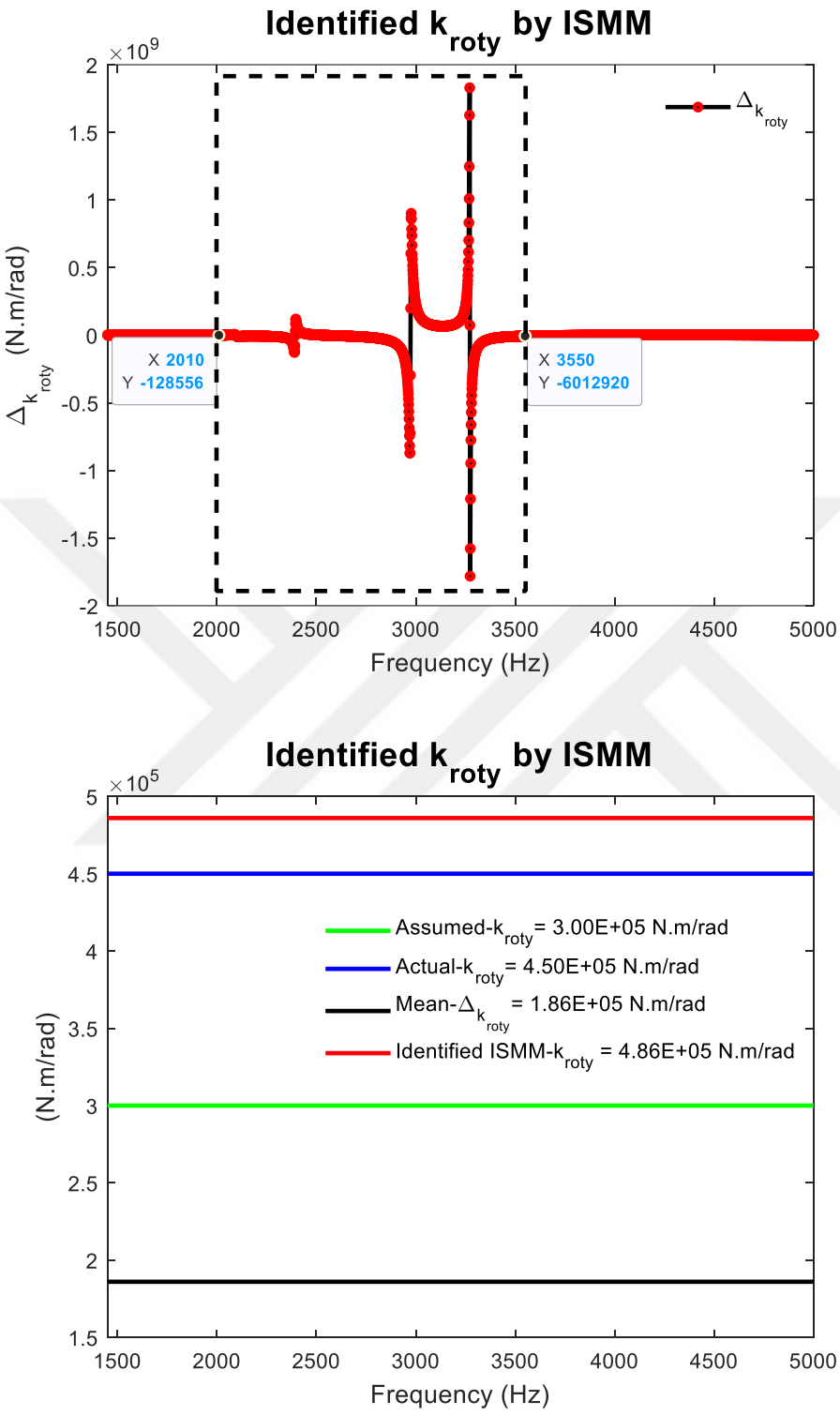


Figure 3.12 Identified stiffness values of k_{RotY}

Table 3-4 Results of identified joint parameters

Stiffness and Damping Properties	Assumed Model Joint Parameters	Actual Model Joint Parameters	Identified Model Joint Parameters	Abs-Error (%)
$\mathbf{k_{Fz}}$ (N/m)	1.00E+08	2.40E+08	2.55E+08	**6.25**
$\mathbf{k_{M\theta y}}$ (N.m/rad)	3.00E+05	4.50E+05	4.86E+05	**8.00**
$\mathbf{c_{Fz}}$ (N.s/m)	47	57	6.20E+06	-
$\mathbf{c_{M\theta y}}$ (N.m.s/rad)	3	5	2.69E+04	-

When the damping results are examined in Figure 3.13 and Figure 3.14, it is clear that the identified damping values deviate significantly from the actual ones. The magnitudes of the viscous damping in assumed and actual models are much smaller than the stiffness values of the same models. Because identification by ISMM is accomplished through matrix inversion, minor errors can result in significant errors after matrix inversion, as indicated in [17]. That is why the identified damping results in this study are not considered for the upcoming comparison analyses. Also, since the damping identification is unrealistic, the absolute error calculation of the identified damping values in Table 3-4 is disregarded.

`

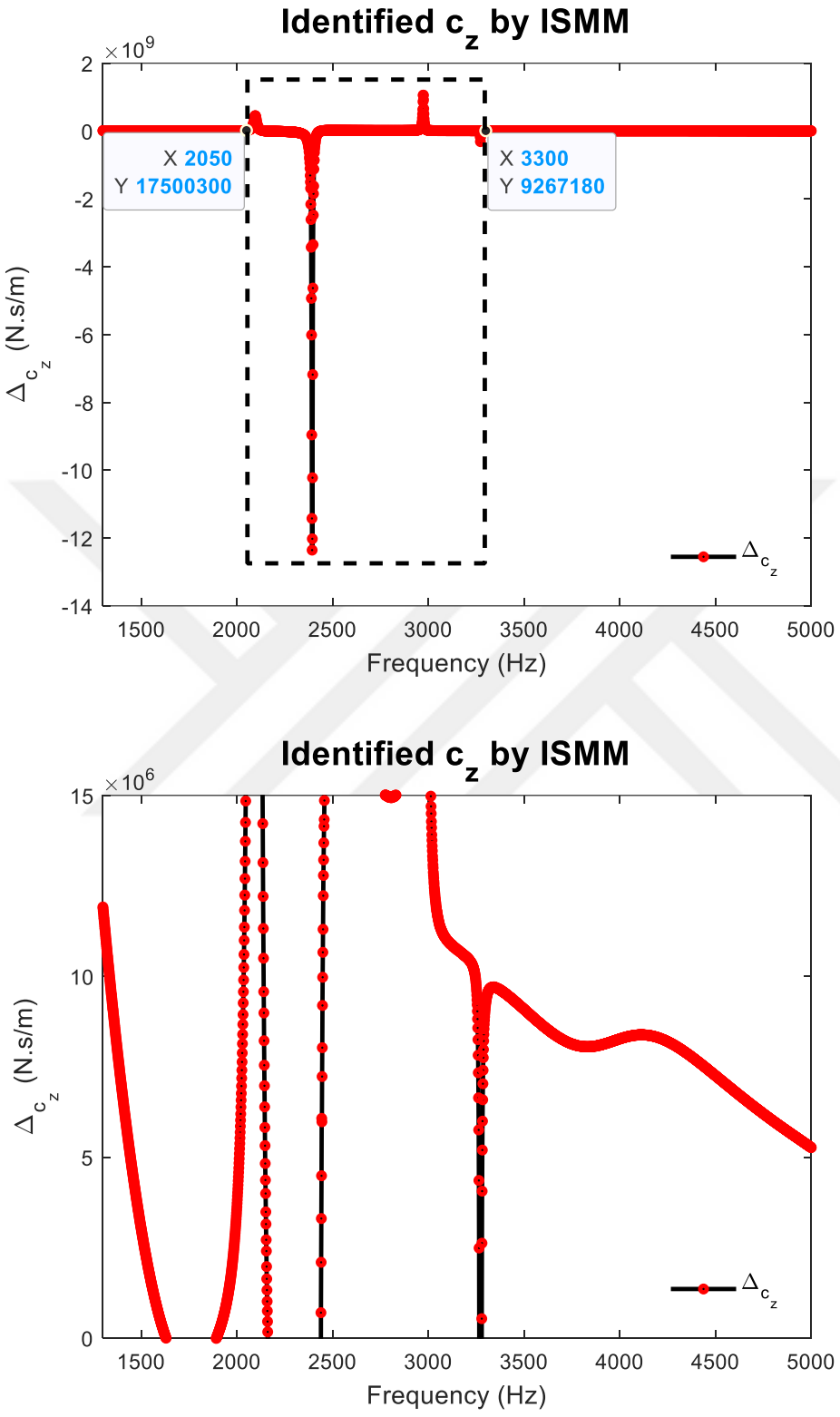


Figure 3.13 Identified damping value of c_Z (zoom out (upper)- zoom in (lower))

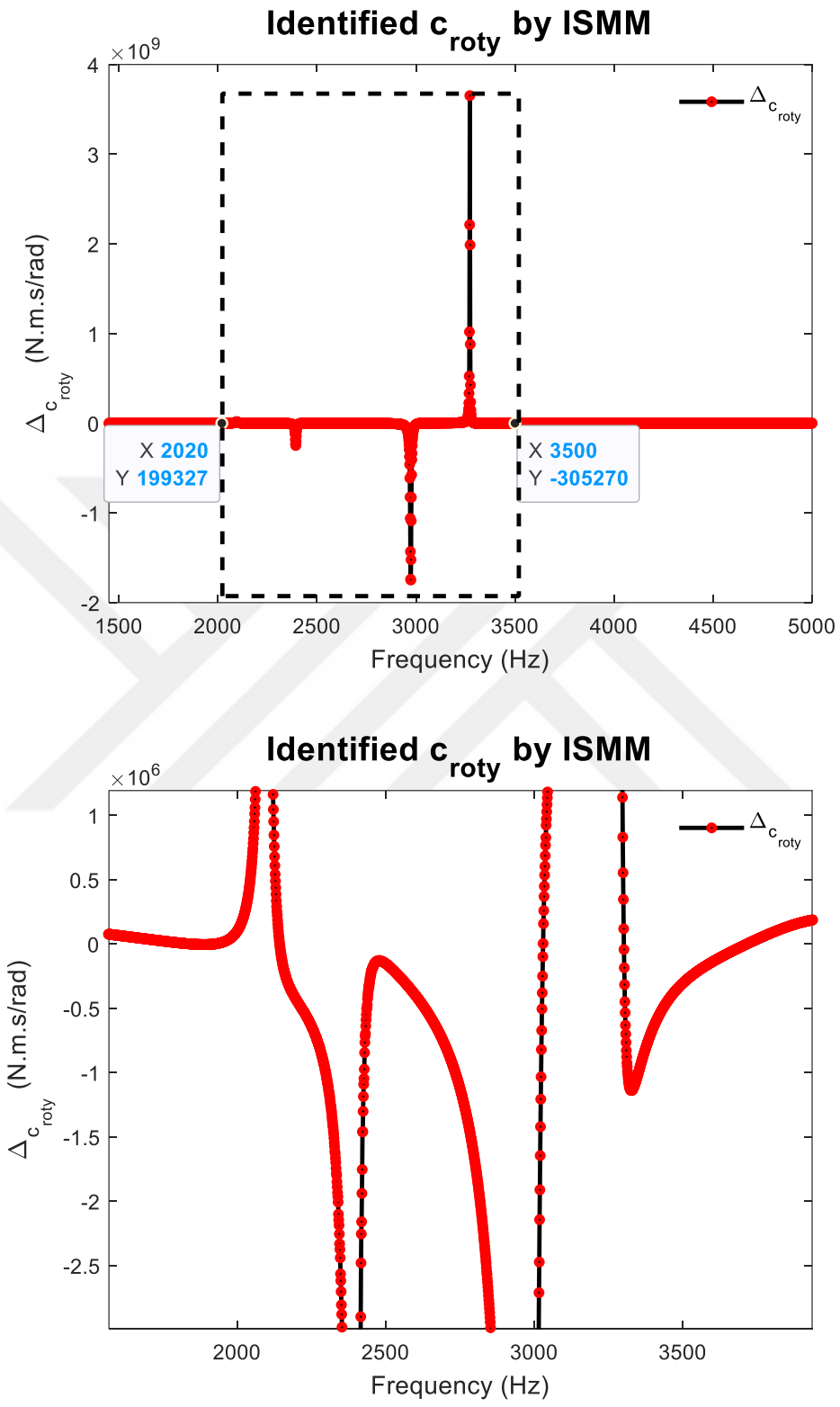


Figure 3.14 Identified damping value of c_{RotY} (zoom out (upper)- zoom in (lower))

Since the core objective of employing ISMM is to develop a complex stiffness matrix capable of exhibiting the same dynamic behavior as the assembly's contact dynamics, the harmonic analyses of the holder-extension assembly are repeated with the identified stiffness values to ensure the correctness of the identified complex stiffness values. Since the identified viscous damping results are unreliable, they are not included in the repeated harmonic analyses. Only structural damping values are defined.

Finally, the FRF of the holder-extension assembly is calculated using the identified contact parameters, and the obtained FRFs are shown in Figure 3.15, along with the FRFs obtained using the assumed and actual contact parameters.

As seen from Figure 3.15, when there is a deviation of about 10 percent in the accuracy of stiffness identification, it is observed that the FRF results closely correspond to their actual counterparts in the contact dynamic’s faces. Although identification analyses encompass frequencies ranging from 0 to 5000 Hz, FRFs are extracted up to 10 kHz as evidence to support the validity of the developed stiffness values within a more extensive frequency spectrum.

`

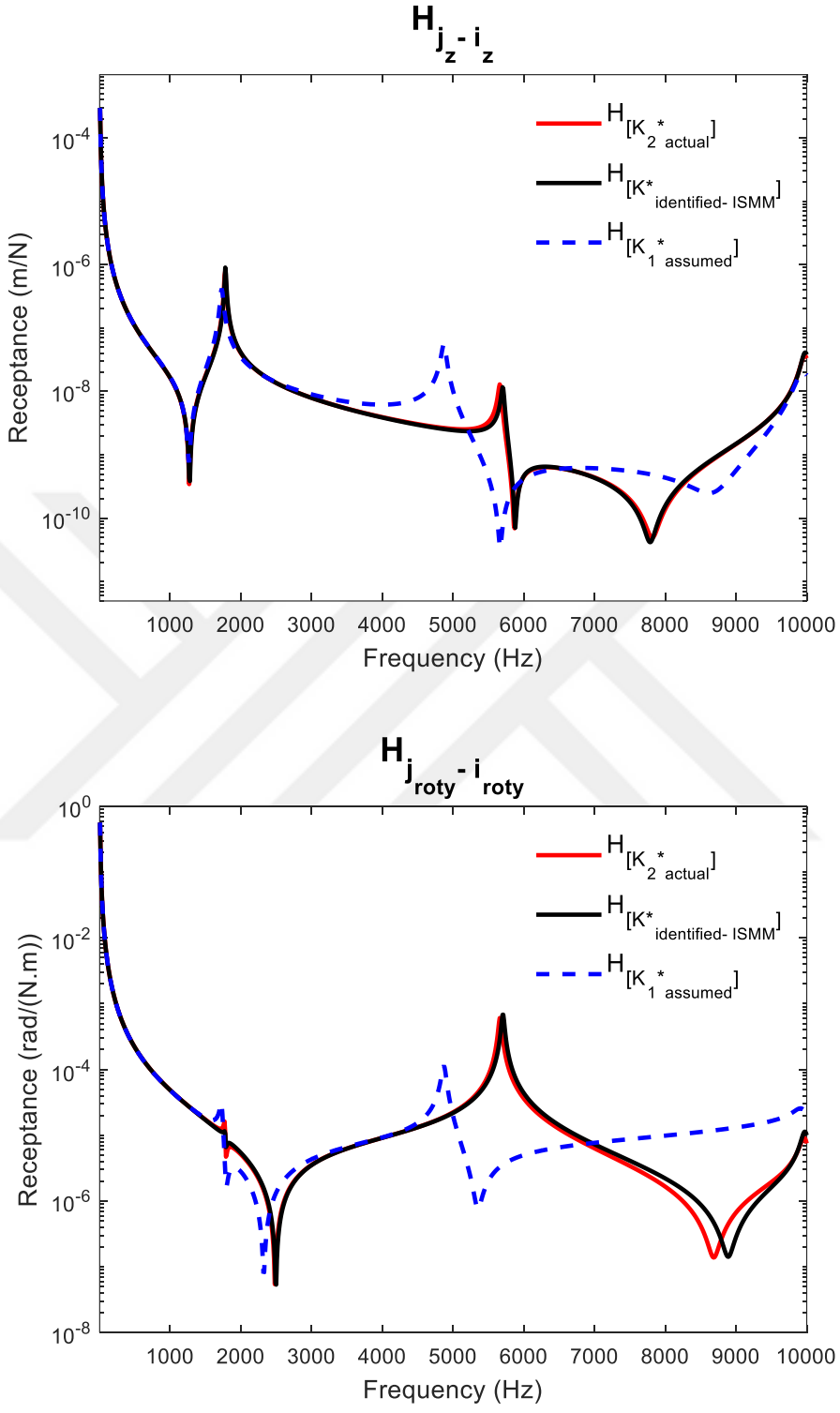


Figure 3.15 Calculated FRFs using identified contact parameters between RP1 and RP2 (*i-j*), in +*Z* and +*RotY* direction

`

3.4 Effects of Identification Ranges on the ISMM's Results

To check the sensitivity of the identification method to the frequency range, based on the results shown in Figure 3.10, a broader frequency range (560-5000 Hz) is selected for the identification. Then, contact parameters are identified for the same system using the new frequency region. Identified contact parameters using different frequency regions are given in Table 3-5.

Table 3-5 Sensitivity Ranges

Stiffness Direction	**Sensitivity Range**	**Identified Stiffness Values by ISMM**	**Absolute Error (%)**
$\mathbf{k_{M\theta y}}$	560-5000 Hz	5.09E+05	**13.11**
	1450-5000 Hz	4.86E+05	**8.00**
$\mathbf{k_{Fz}}$	560-5000 Hz	2.32E+08	**3.33**
	1400-5000 Hz	2.55E+08	**6.25**

As shown in Table 3-5, stiffness values identified are subject to variation as the identification range is modified, indicating their sensitivity to the identification range. However, for this specific dataset, it is not possible to get a result showing that the identified stiffness value rises as the range widens.

The cross-rotational and translational FRFs at the contact face are given for the new stiffness values in Table 3-5. The effects of k_{RotY} on the cross rotational FRF at the contact dynamics are given in Figure 3.16, while the effects of k_Z is represented in Figure 3.17. The calculation of the cross-rotational FRFs in Figure 3.16, takes into account the actual value of the k_Z value identified in Section 3.3.

`

Similarly, for the cross translational FRFs' calculation in Figure 3.17, the actual value of k_{RotY} identified in Section 3.3 is used.

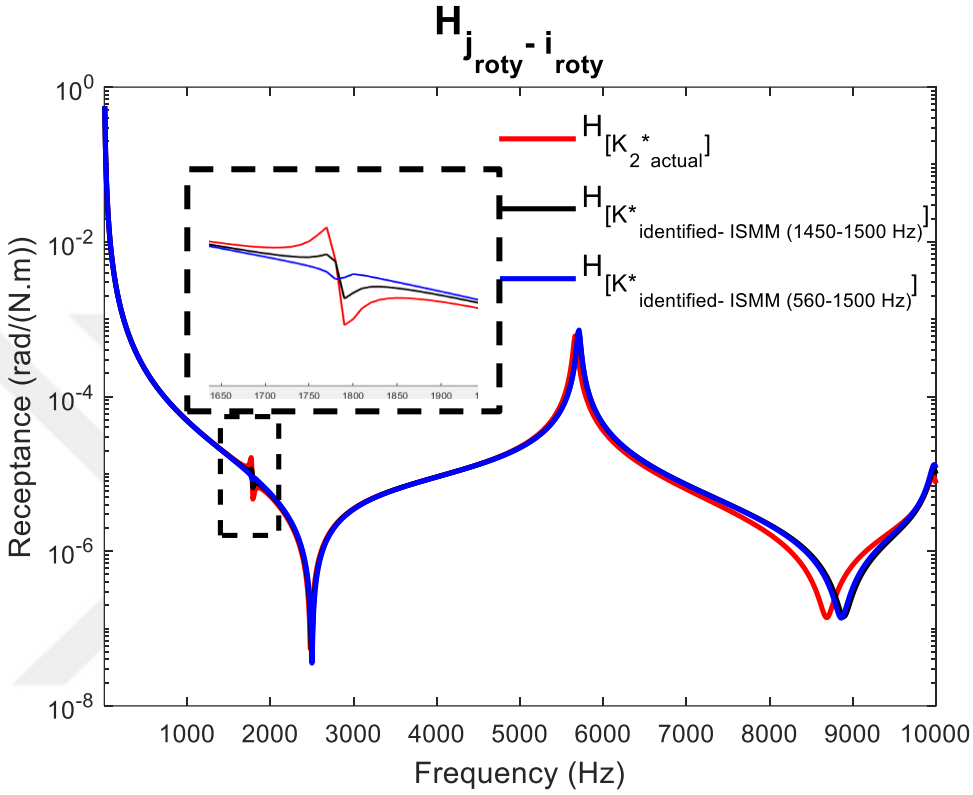


Figure 3.16 Calculated cross-rotational FRFs using identified contact parameters between RP1 and RP2 (*i*-*j*) for different identification ranges

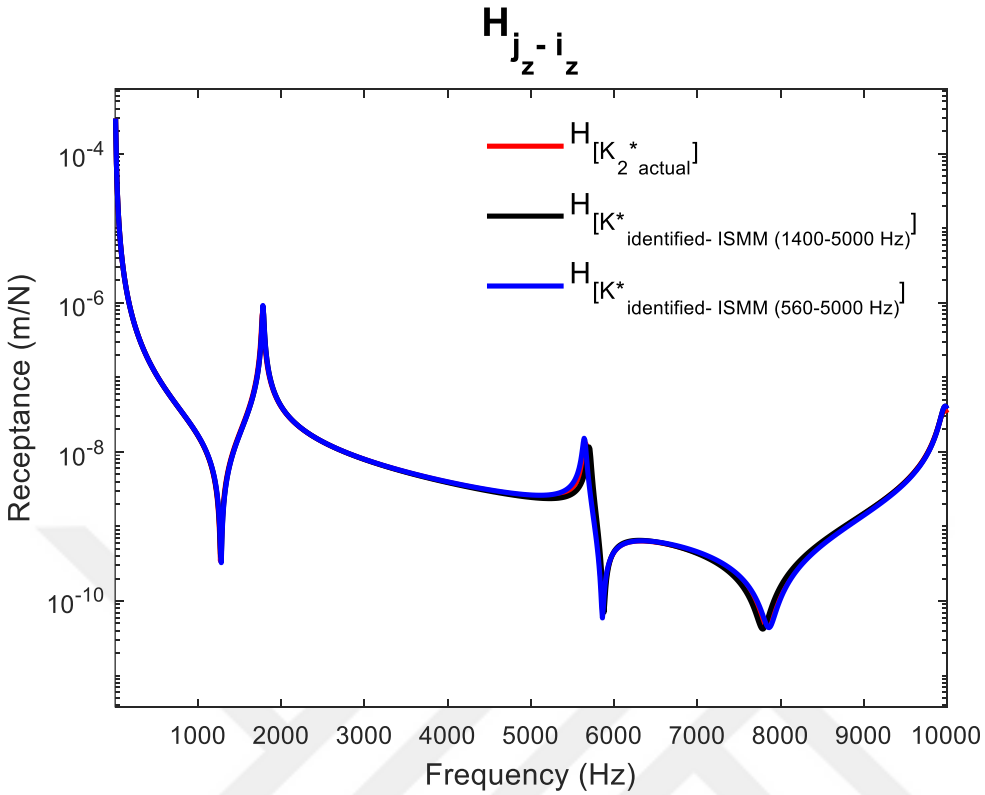


Figure 3.17 Calculated cross-translational FRFs using identified contact parameters between RP1 and RP2 (*i-j*) for different identification ranges

In Figure 3.16, the first natural frequency is not shown for the stiffness values of the k_{RotY} determined in the range of 560-5000 Hz. Because the first mode of the system is highly dependent on the rotational stiffness, to make a good estimation for the first frequency, rotational stiffness values should be identified close to the actual stiffness value. On the other hand, there is no significant difference in the effects of k_Z (Figure 3.17), which makes the estimation of the second mode match well with its actual counterpart.

3.5 Effects of Noise on the ISMM's Results

Until now, all calculations have been performed with noise-free data. However, the experimental results contain measurement errors. The actual model FRFs in Section 3.3 are polluted with two different sets of noise with a zero mean of 5% and a 10% standard deviation to demonstrate the effects of those errors on the identified results by ISMM. The polluted cross-translational and rotational FRFs are represented in Figure 3.18.

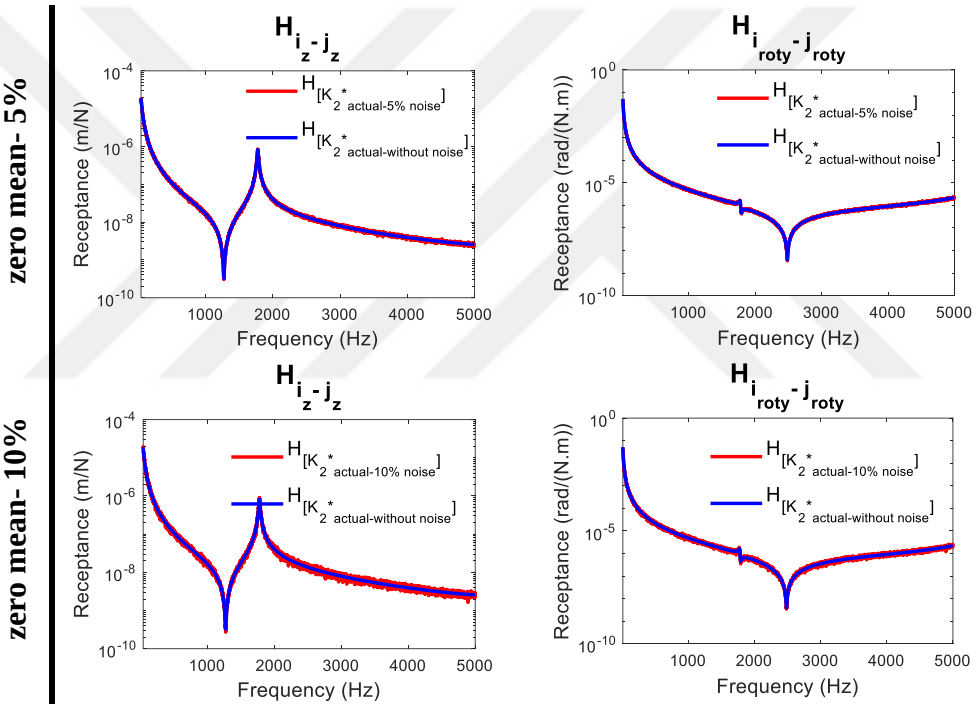


Figure 3.18 Polluted FRFs with different levels of random noise

Then, contact stiffnesses are identified using the polluted FRFs, and the results obtained are given in Table 3-6 for the 5% and 10% noisy data along with the noise-free case. In addition, the FRFs of the system are calculated using the contact parameters given in Table 3-6, and these FRFs are given in Figure 3.19.

Table 3-6 Identified stiffness values with polluted data

Stiffness Direction	**Identified Stiffness Values by ISMM**		
	without noise	***zero mean- 5% noise***	***zero mean-10% noise***
$\mathbf{k_{Fz}}$	2.55E+08	2.16E+08	2.56E+08
$\mathbf{k_{M\theta y}}$	4.86E+05	4.83E+05	2.3E+06

As seen from Table 3-6, the noise's effect on the identified rotational stiffness value starts to become significant at the level of 10% random noise, while there is no significant impact on the identified translational stiffness value. However, these observations alone do not provide enough evidence to draw a definitive conclusion regarding the deviation of the identified stiffness caused by noise.

When the FRF results are examined in Figure 3.19, especially on the cross-rotational FRF graph, it is clear that the FRF value at the first natural frequency, where the rotational stiffness value has more impact, deviates significantly when the error increases. On the other hand, the cross-translational FRF value, particularly in the vicinity of the second natural frequency where translational stiffness holds a significant impact, is almost identical to the actual value, with a difference of approximately 5%. However, there is no clear indication of the noise level in the cross-translational FRFs.

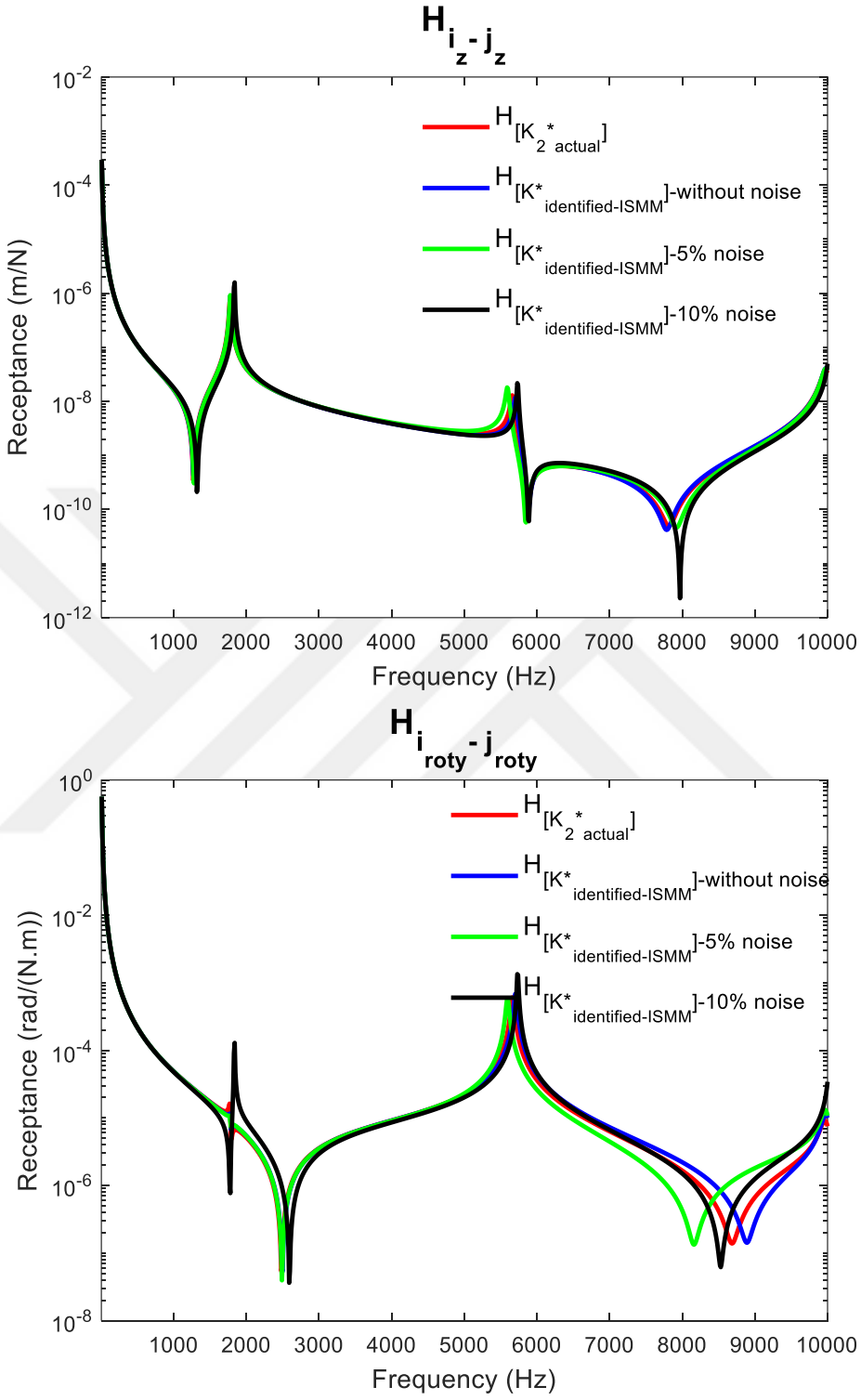


Figure 3.19 Identified FRF results for polluted data

CHAPTER 4

SIMULATED EXPERIMENT STUDIES

Chapter 3 aims to apply the ISMM method to identify the complex stiffness matrix at the holder-extension interface, which represents the contact dynamics, through numerical models. In Chapter 3, all required FRFs, including the RDOFs, are obtained directly from the FE model, and ISMM is applied for the identification.

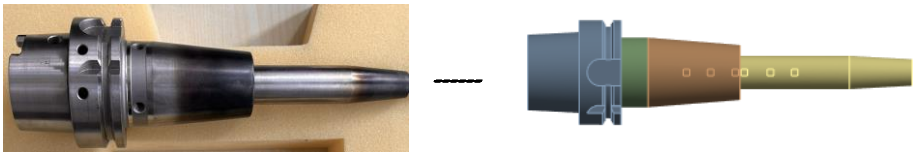
However, the measurement of rotational FRFs is often challenging and impractical due to the lack of specialized equipment. These limitations can be altered by the approximate methods where rotational FRFs are obtained using the translational FRFs and FD methods.

Before the application of actual experiments, in this chapter, the accuracy of the approximation methods for obtaining the FRFs for rotational DOFs and their effect on identification results are investigated using the FE model. To do that, translational FRFs are obtained from the FE model and treated as simulated experiments. Then, the ISSM is applied using both translational and approximated rotational FRFs, and contact parameters are identified. Also, it is essential to note that this chapter includes simulated experiment demonstrations, focusing on THE assembly.

In this chapter, simulated experiment results taken by ANSYS are used in contact dynamics identification. The steps of contact dynamics identification through the ISMM are displayed in Figure 4.1 below. All steps represented in Figure 4.1 are detailed under the subsections.

Creating an ANSYS FE Model

representing the same behavior as the actual THE assembly



Obtaining RDOF FRFs of P2 to P4 (Figure 5.2)

making use of the Finite Difference Technique [33]

requiring to apply the SEMM method

Obtaining Translational and Rotational FRFs at Contact Face

making use of the SEMM method [25], which enables to get the experimental model

requiring to apply ISMM

Applying ISMM and Identifying Contact Stiffness Matrix

Figure 4.1 The procedure of the study for simulated experiment data

As a brief roadmap for this chapter,

- Section 5.1 details the impact hammer test's plan and results. Those results are used to check how close the created simulation model results are to the impact hammer test results.
- In Sections 4.2 and 4.3, simulated experiment studies are executed based on the FE simulation, and FDT results are shared. Measuring rotational FRFs in experiments is often challenging and impractical due to the lack of

specialized equipment. That is why the studies detailed in Sections 4.1 to 4.4 require identifying RDOF FRFs at the identification points used in the ISMM. Estimation techniques are used to obtain the RDOF FRFs, and their effects on the results are also discussed in related subsections. Those two studies differ from the faces where contact dynamics are defined. The reasons behind two different simulated experiments are detailed in related sections.

4.1 ANSYS FE Model

As indicated earlier, this section aims to show the applicability of the ISMM through a simulated experiment. To achieve this, the initial stage involves developing an FE-model that accurately reflects the dynamic behavior of the actual TEH assembly dynamics.

Firstly, the tool is added to the ANSYS FE model, explained in Section 3.2. The simulation model with the added tool is given in Figure 4.2. In this model, the tool is modeled as part of the extension but with the material properties of carbide, as outlined in Table 4-1.

Table 4-1 Mechanical properties of the tool

	Material Properties		
	Elastic Modulus- E (GPa)	**Density- ρ ($kg.m^{-3}$)**	**Poisson's Ratio -ν**
Tool (Carbide)	560	14400	0.22

The contact dynamics definition is kept the same regarding the modeling method and the magnitude of the stiffness values, as given in Section 3.3. In this model, only structural damping is defined in the model parameters since, in Section 3.3, it has been concluded that a small numerical error in the obtained FRFs causes a significant error when the inverse of that error is taken [17]. Except for those considerations, all simulation settings in this new model are identical to those outlined in Section 3.2.

After the modeling, model-based harmonic analysis is conducted, as detailed in Section 3.3, to simulate the experimental FRF values.

The simulated experiment FRF results at points P1 to P5 are compared with their experimental counterparts (as detailed in Section 5.1). This comparison aims to determine how closely the simulated experiment model represents the dynamic behavior of the actual TEH assembly model because the outcome of the simulated experiments will be valid for real experimental studies. The results of these comparisons can be seen in Figure 4.3.

As shown in Figure 4.3, the FRFs near the joint interface exhibit a satisfactory agreement, particularly between points P2 to P4. These data points are then utilized to develop a hybrid model through the System Equivalent Model Mixing (SEMM) Method. SEMM is used to obtain the FRFs at the contact faces since the contact faces are not reachable to make measurements even in the translational direction. The details of the SEMM method and its use in this study are utilized in Section 4.3. However, before applying SEMM to obtain contact faces' FRF matrices, it is necessary to fully represent the dynamic behavior of points P2 to P4. As mentioned earlier, only translational FRFs are measured in the experiments due to the specific requirements of the sensors and excitation system for measuring rotational FRFs. Therefore, the Finite Difference Technique (FDT) [33] is used to obtain the RDOF FRFs as an expansion technique,

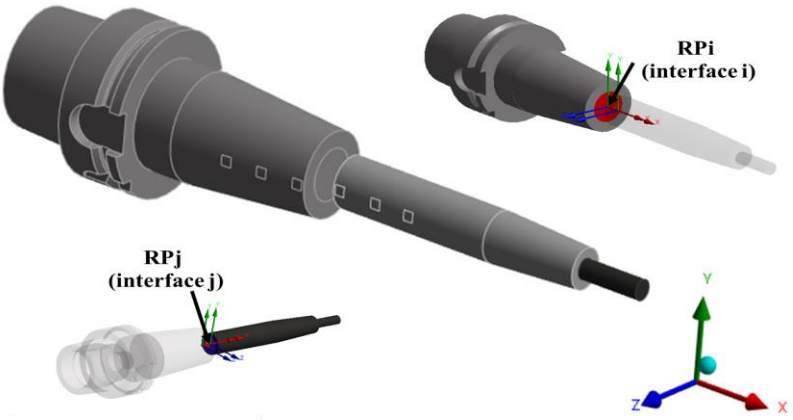


Figure 4.2. Tool-Extension-Holder assembly FE model

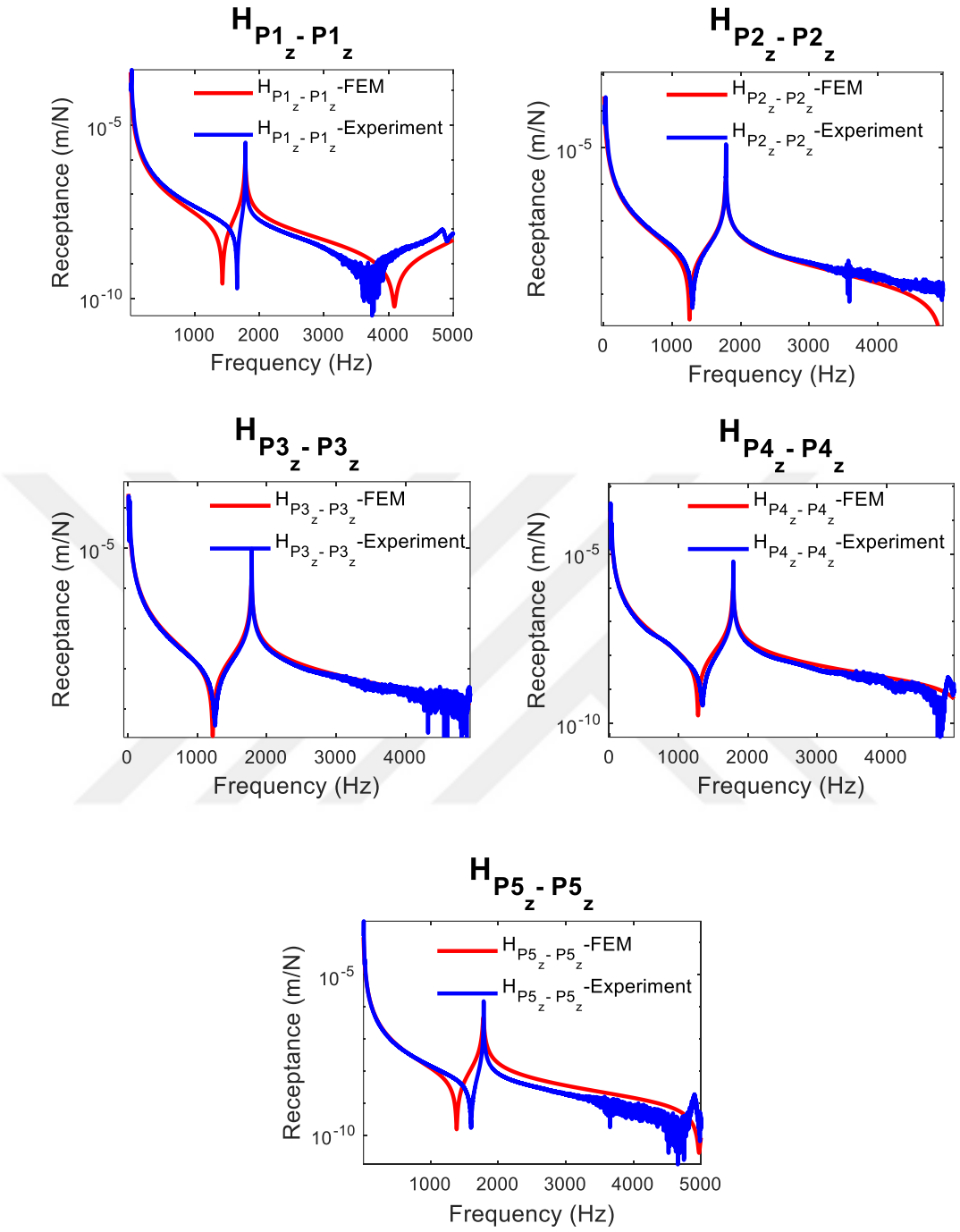


Figure 4.3 Comparison of the FRFs by Simulated (Finite Element Model) and Actual Experiment

4.2 Estimation of RDOF FRFs by Finite Difference Technique

Rotational FRFs can be confidently identified by employing FRF expansion techniques after acquiring translational FRFs at specific locations. To do that, The Finite Difference Technique [33] is applied to generate rotational FRF information for points P2 to P4. In this approach, three (or two) accelerometers are placed close to each other with a constant spacing, *s* (Figure 4.4). Then, translational measurements are used in finite-difference formulas to calculate the rotational quantities. The first and second-order finite-difference transformation matrices are needed for estimating the rotational parameters. [33]

Using the Finite difference method, RDOFs can be obtained as follows:

$$[H_{est}] = \begin{bmatrix} H_{yy} & H_{y\theta} \\ H_{\theta y} & H_{\theta\theta} \end{bmatrix} = [T_{2?}][H_{meas}][T_{2?}]^T \tag{4.1}$$

where

$$[H_{est}] = \begin{bmatrix} H_{AA} & H_{AB} & H_{AC} \\ H_{BA} & H_{BB} & H_{BC} \\ H_{CA} & H_{CB} & H_{CB} \end{bmatrix} \tag{4.2}$$

$T_{2?}$ is the transformation matrix, and in this study, first-order forward and backward and second-order approximation matrixes (Table 4-2), which are forward, central, and backward finite difference transformation matrices, are used for RDOF FRFs estimation of points P2 to P4.

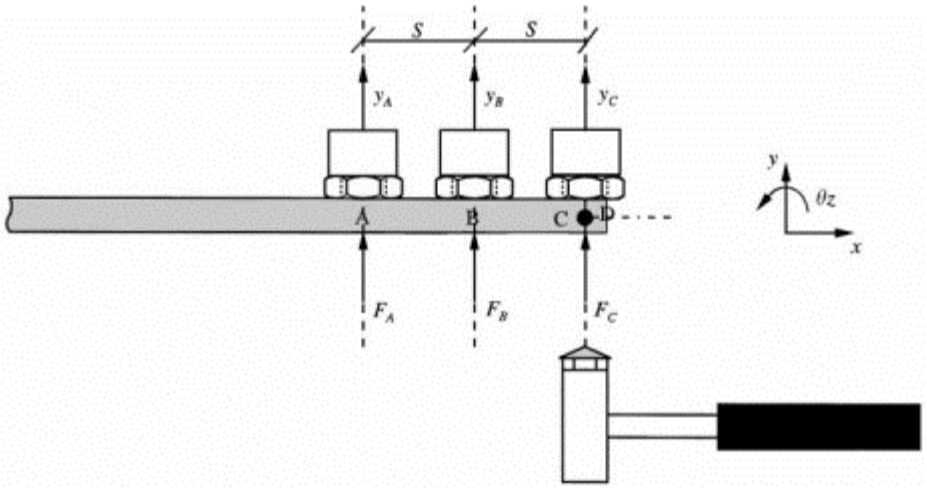


Figure 4.4 Close-accelerometers method for RDOFs [33]

Table 4-2 Transformation matrices [33]

	First-order	Second-order
Forward	$[T_{2f}] = \begin{bmatrix} 0 & 1 \\ 1/s & -1/s \end{bmatrix}$ (4.3)	$[T_{2f}] = \frac{1}{2s}\begin{bmatrix} 0 & 0 & 2s \\ -1 & 4 & -3 \end{bmatrix}$ (4.4)
Center	-	$[T_{2c}] = \frac{1}{2s}\begin{bmatrix} 0 & 2s & 0 \\ -1 & 0 & 1 \end{bmatrix}$ (4.5)
Backward	$[T_{2f}] = \begin{bmatrix} 0 & 1 \\ 1/s & -1/s \end{bmatrix}$ (4.6)	$[T_{2b}] = \frac{1}{2s}\begin{bmatrix} 0 & 0 & 2s \\ 1 & -4 & 3 \end{bmatrix}$ (4.7)

The procedure given above is now applied to the current work to obtain the required RDOF FRFs at points P2 to P4. Additionally, the ANSYS FE simulation extracts rotational results at those points. Both RDOF FRF results, belonging to the FDT and the ANSYS FE simulation, are then presented in the same graph (Figure 4.5- Figure 4.7) to facilitate a comparison of the impact of the RDOF FRF estimation method on the results.

- ***P2 RDOF FRF $H_{P2-roty}$ Estimation***

  P2, P1, and P6 are used to determine the $H_{P2-roty}$. The technique of second-order forward finite difference is applied. Obtained $H_{P2-roty}$ is given in Figure 4.5.

- ***P3 RDOF FRF- $H_{P3-roty}$ Estimation***

  P3, P4, and P5 are used to determine the $H_{P3-roty}$. The technique of second-order backward finite difference is applied. Obtained $H_{P3-roty}$ is given in Figure 4.6.

- ***P4 RDOF FRF- $H_{P4-roty}$ Estimation***

  P3, P4, and P5 are used to determine the $H_{P4-roty}$. The technique of second-order center finite difference is applied. Obtained $H_{P4-roty}$ is given in Figure 4.7.

Note that the FRFs obtained with the FDT approximation are named the Duarte model in Figure 4.5 to Figure 4.7. In Figure 4.5, it is obvious that the rotational FRFs of the Duarte Model and the Simulated Experiment Model give different results. The behavior of the obtained FRFs is completely different. This deviation is due to the boundary condition in the FE model. The effects of the boundary condition on the FDT results are examined, and the results are shared in Section 4.5 in detail.

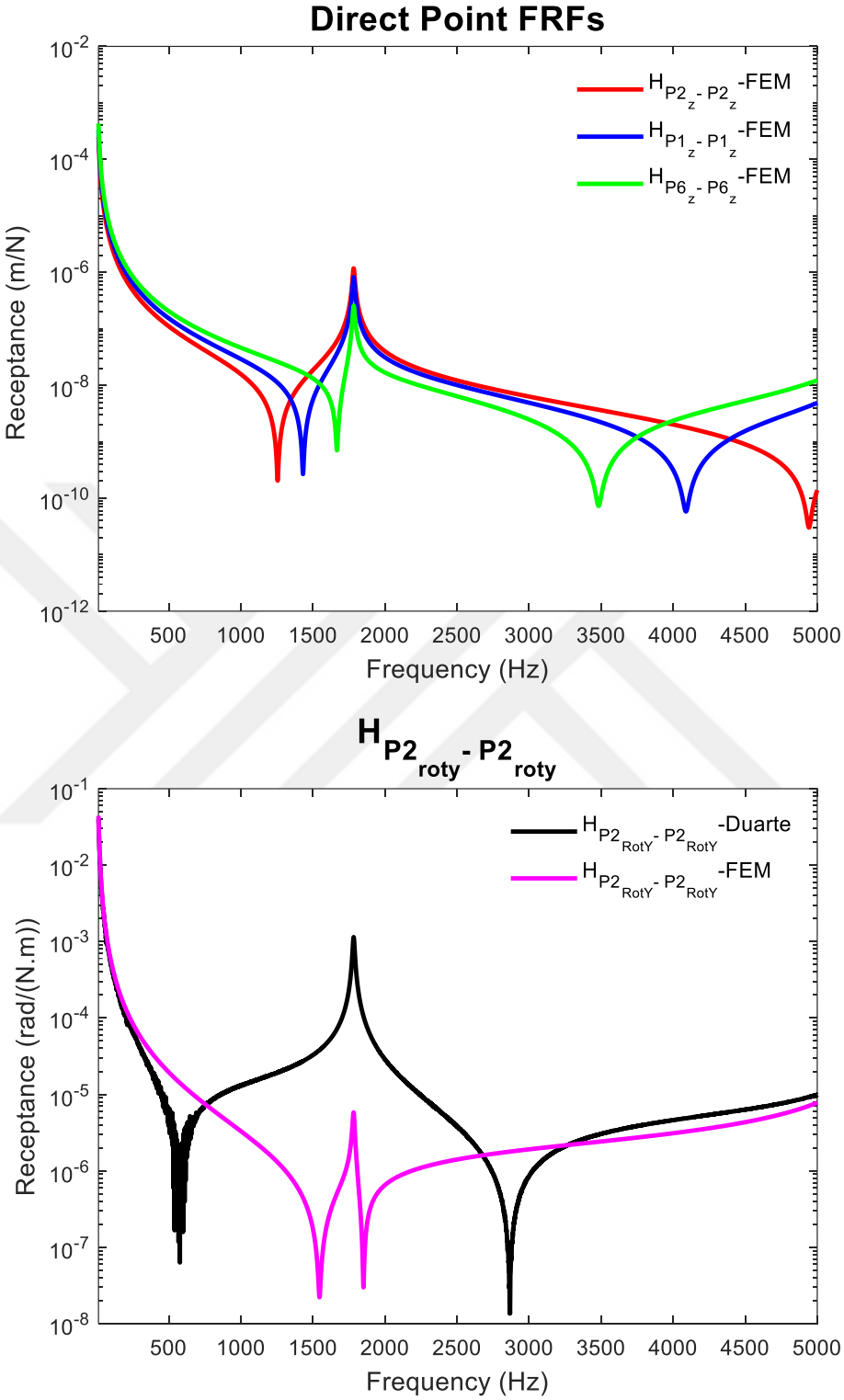


Figure 4.5 Translational FRFs used in the FDT (upper) and obtained rotational FRFs at P2 (lower)

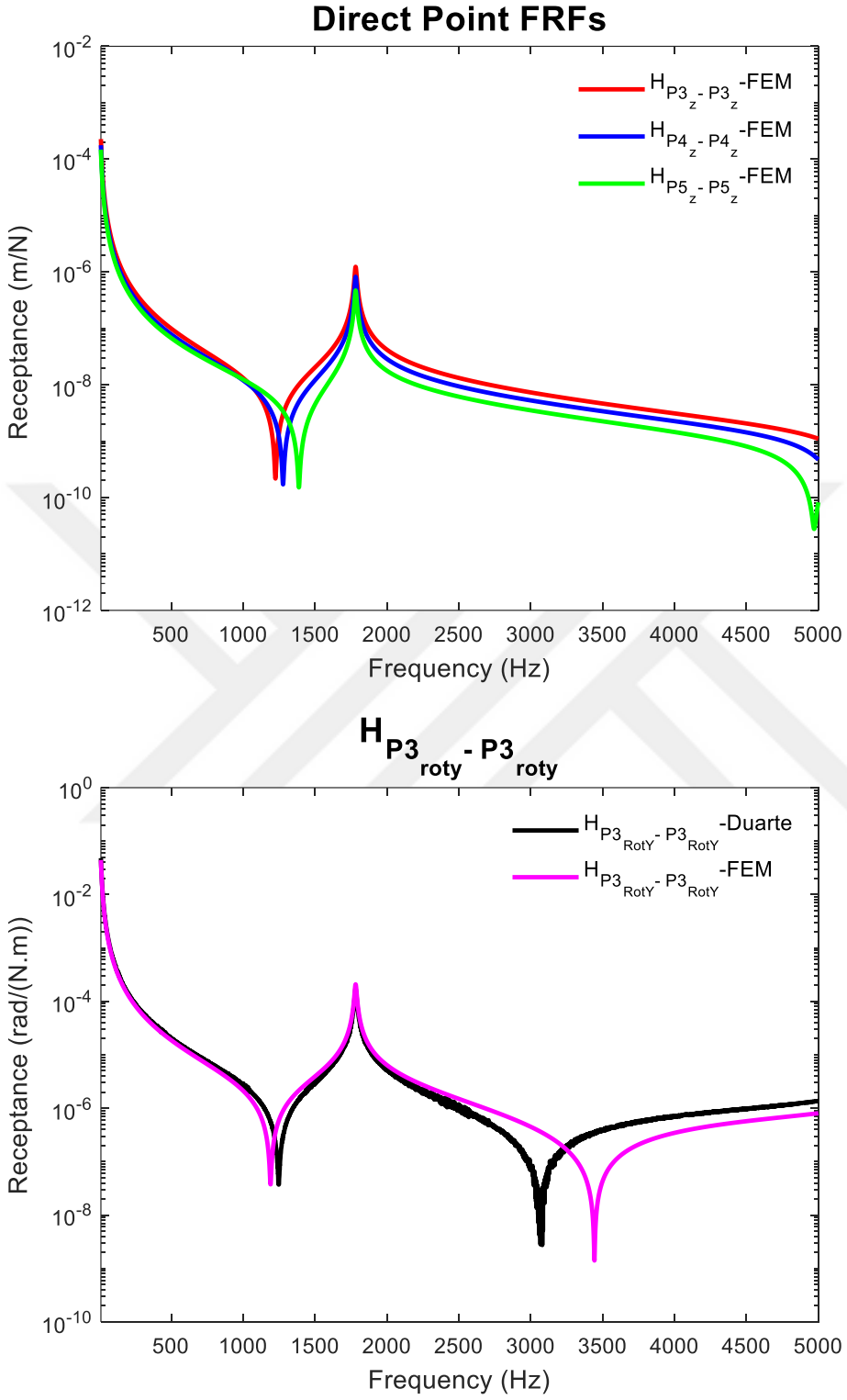


Figure 4.6 Translational FRFs used in the FDT (upper) and obtained rotational FRFs at P3 (lower)

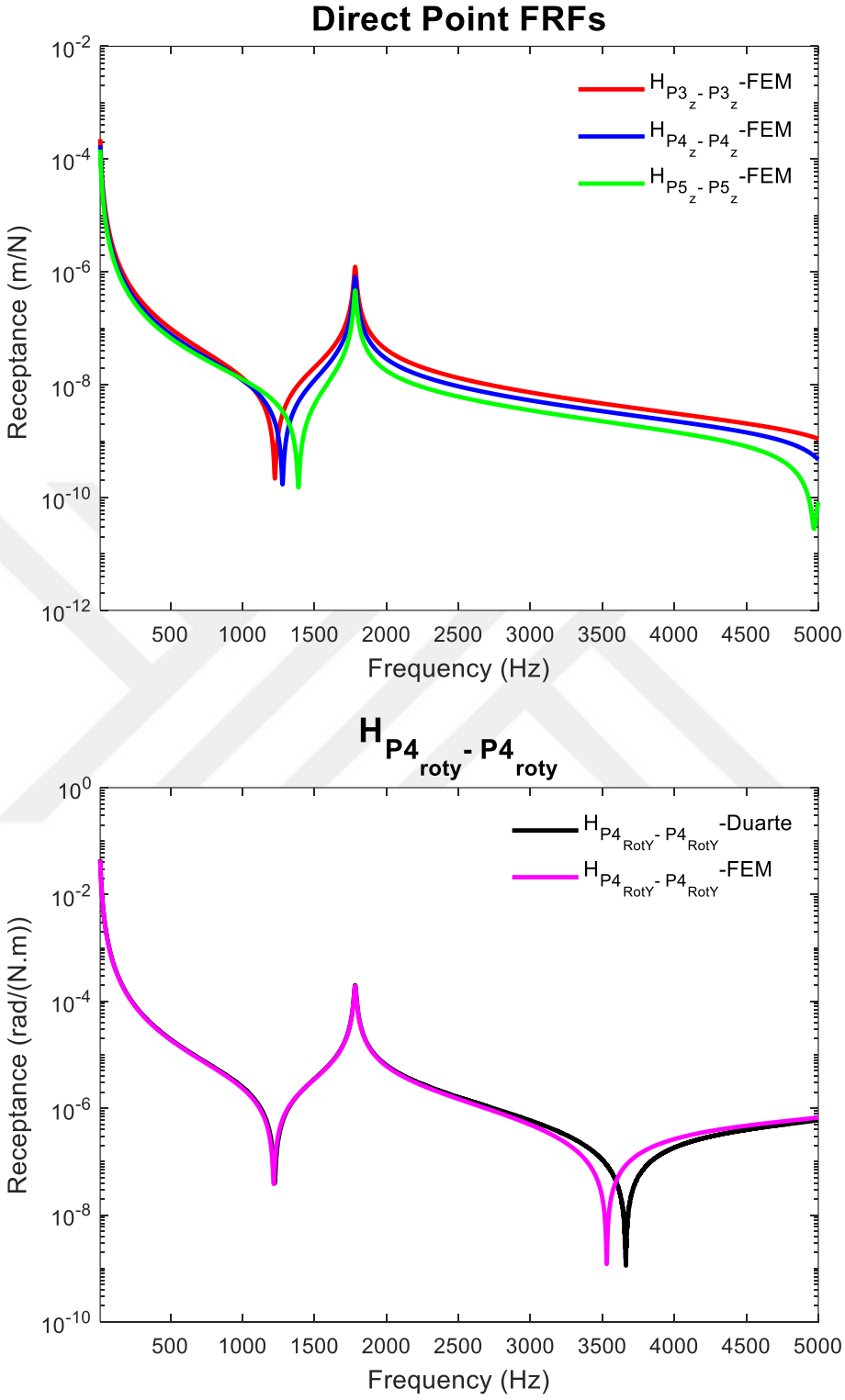


Figure 4.7 Translational FRFs used in the FDT (upper) and obtained rotational FRFs at P4 (lower)

Unlike the FDT results at P2, in Figure 4.6 and Figure 4.7, the obtained rotational FRF from the FE model and the Duarte method at points P3 and P4 follow each other quite well in terms of the value of the natural frequency and the behavior of the FRFs. There is a slight deviation around antiresonance frequency at P3 in Figure 4.6, but this difference is at the level of E-08, which is visible since the scale of the figure is logarithmic. After rotational FRFs are obtained for the data points, it is time to create a 4*4 FRF matrix, β, which includes both translational and rotational FRF values of the contact face. However, since the contact face is not directly accessible, expansion methods must be employed to obtain the necessary FRF values. This study uses the SEMM [25] as the expansion method.

4.3 Obtaining Translational and Rotational FRFs at Contact Face by System Equivalent Model Mixing (SEMM) Method (Klaassen et al., 2018)

The SEMM Method is a hybrid approach that extends observed and/or measured DOFs to inaccessible DOFs. SEMM operates based on the frequency and enables the combination of numerical and experimental models from different ways of modeling the same system to create a hybrid model that follows the dynamic behavior of a parent model.[25]

In the SEMM method [25], a parent model with many degrees of freedom (N) is connected to an overlay model with a smaller subset ($M \leq N$) of degrees of freedom. From this connected model, a subset of the parent model called the removed model is separated to create a new hybrid formulation. This hybrid model has the same size as the parent model (N), but it includes the dynamic information from the overlay model. It also has a full dynamics response of the entire system.[25]

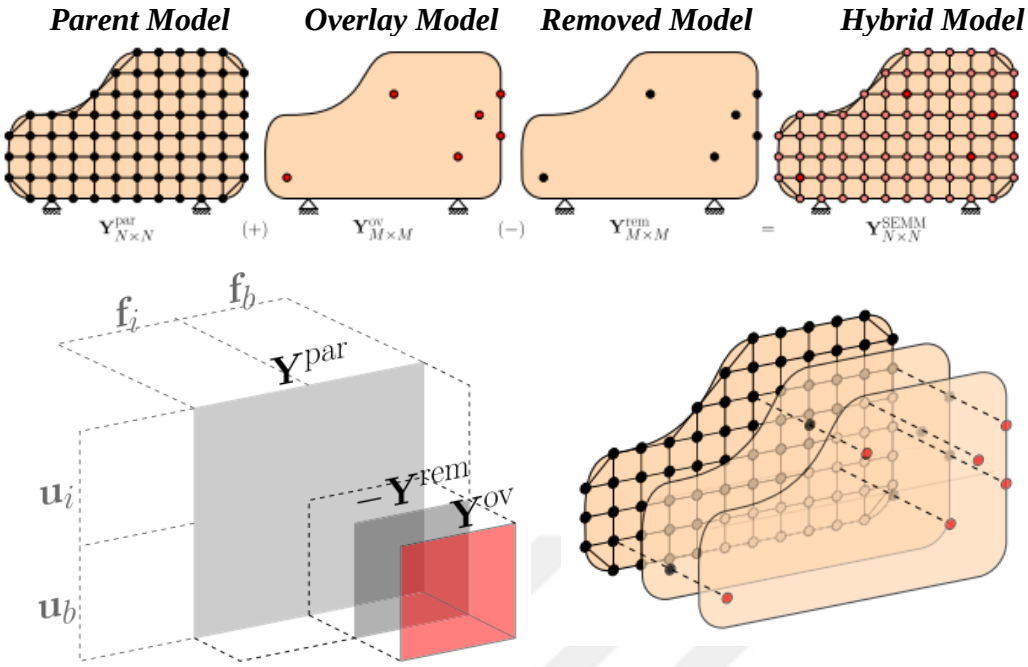


Figure 4.8. Visual representation of SEMM method components [25]

$$H^{SEMM} = H^{par} - H^{par}\left([H_{bi} \quad H_{bb}]^{rem}\right)^{+}\left(H_{par}^{rem} - H^{ov}\right)\left(\begin{bmatrix} H_{ib} \\ H_{bb} \end{bmatrix}^{rem}\right)^{+} H^{par} \tag{4.8}$$

where

H^{SEMM} *: Equivalent hybrid model includes interface DOFs*

par: Parent model where interface dynamics are obtained.

ov: Overlay model where experimental results are added to hybrid system results.

rem: removed model from parent model

b: boundary DOFs removed from the parent model

i: interface DOFs.

The details of the theory can be found in [25]. Only Equation (4.8) obtained by SEMM is used in the study to get experimental contact face dynamics, 4*4 FRF matrix. The utilization of SEMM in this study is elaborated upon below.

- **Hybrid Model:** *The model asked to obtain has all FRFs, even inaccessible DOFs.*
    - In this study, it is the one that is used in ISMM for contact dynamics identification.
- **Parent Model**: *The model that hybrid models' DOFs come from. However, it does not contribute to the dynamics of the hybrid model.*
    - In this study, it is the ANSYS FE model with 2 DOF spring-dashpot and has both translational and rotational FRFs of the P2, P3, P4, i, and j. (Figure 4.9)

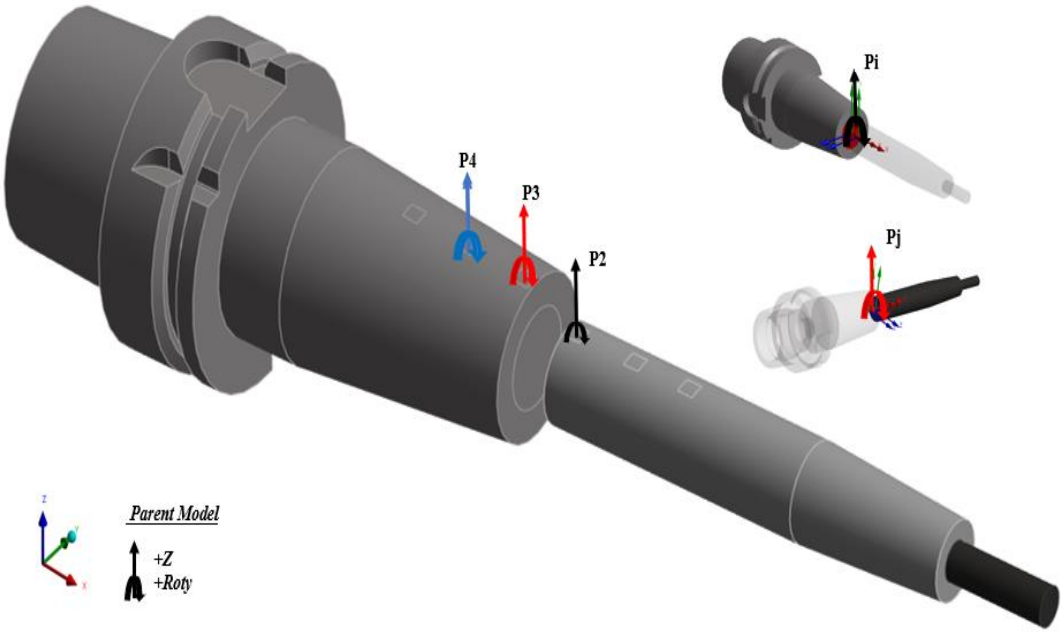


Figure 4.9 Parent Model- (FE model includes +Z and +RotY FRFs)

- **Overlay Model**: *The model that the dynamic properties of the hybrid model come from. Also, it has a subset DOF of the parent model.*

- In this study, it is the simulated experimental model (the same as the Parent Model) and has only translational FRFs of P2, P3, and P4 (Figure 4.10). FDT obtains the rotational FRFs at those points in Section 4.2.

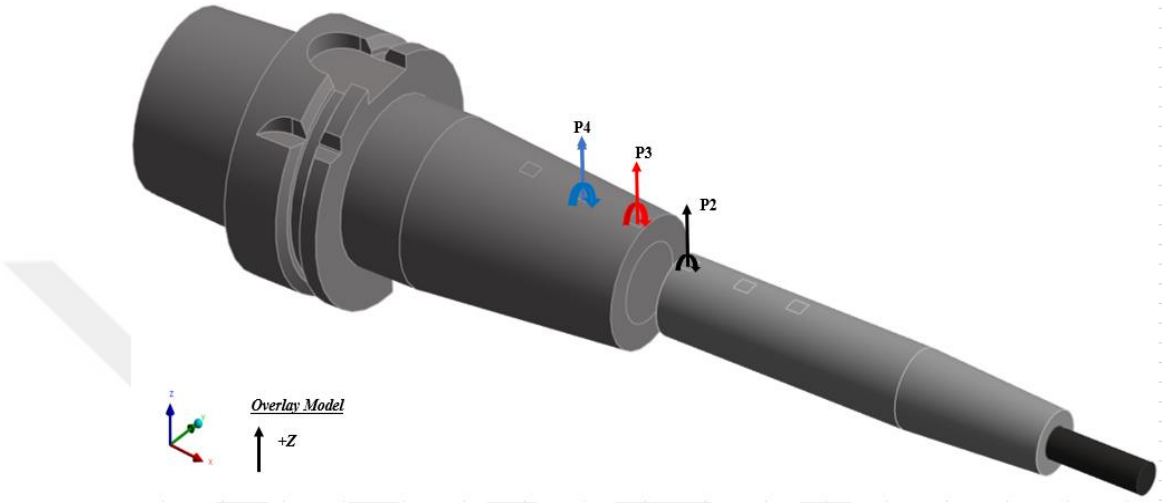


Figure 4.10 Overlay Model- (FE model includes only +Z FRFs)

- **Removed Model**: *The model is the subset of the parent model that contains only translational FRF values for P2, P3, and P4.*

4.3.1 Hybrid Model

The SEMM method aims to create a hybrid model representing the complete dynamics of the contact faces', *i* and *j*, FRF Matrix (4*4). To get the hybrid model by the SEMM method, the translational FRFs from the FE simulation and the rotational FRFs obtained by FDT in Section 4.3 are implemented into Equation (4.8). Using the SEMM Equation (4.8), translational and rotational joint dynamics at the interfaces (*i* and *j*, Figure 4.9) are obtained and shown in Figure 4.11. FRFs obtained are also compared to their Simulated Experiment counterparts. The model obtained

by using the SEMM method is called the Hybrid model and is accepted to have a complex stiffness matrix, $[K_2(w)^*]$.

The names used in the graphs are explained below to make it easy to understand the descriptions used in the graphs.

- **Simulated Experiment- SEMM:** This is the simulated experiment model created by the SEMM method.
- **Simulated Experiment- FEM:** This is the simulated experiment model in which whole results are obtained from the ANSYS FE model.

It can be seen from the results in Figure 4.11 that they are highly different from their Simulated Experiment counterpart. This difference is related to the term $(H_{ov}^{rem} - H^{ov})$ in Equation (4.8). In Section 4.1, the FE model is created by comparing only the translational FRFs of the boundary DOFs at the +Z direction of P2, P3, and P4.

$$\left[H_{par}^{rem} - H^{ov}\right] = \begin{bmatrix} \left[H_{P_Z P_{Z\,all}}^{\;\;rem-ov}\right] & \left[H_{P_Z P_{RotY}\,all}^{\;\;rem-ov}\right] \\ \left[H_{P_{RotY} P_{Z\,all}}^{\;\;rem-ov}\right] & \left[H_{P_{RotY} P_{RotY}\,all}^{\;\;rem-ov}\right] \end{bmatrix} \tag{4.9}$$

Nevertheless, when the results (Figure 4.11) are examined, it is seen that cross-FRF terms are also effective in the results. To make those effects more visible, some investigation studies have been done and represented in the following.

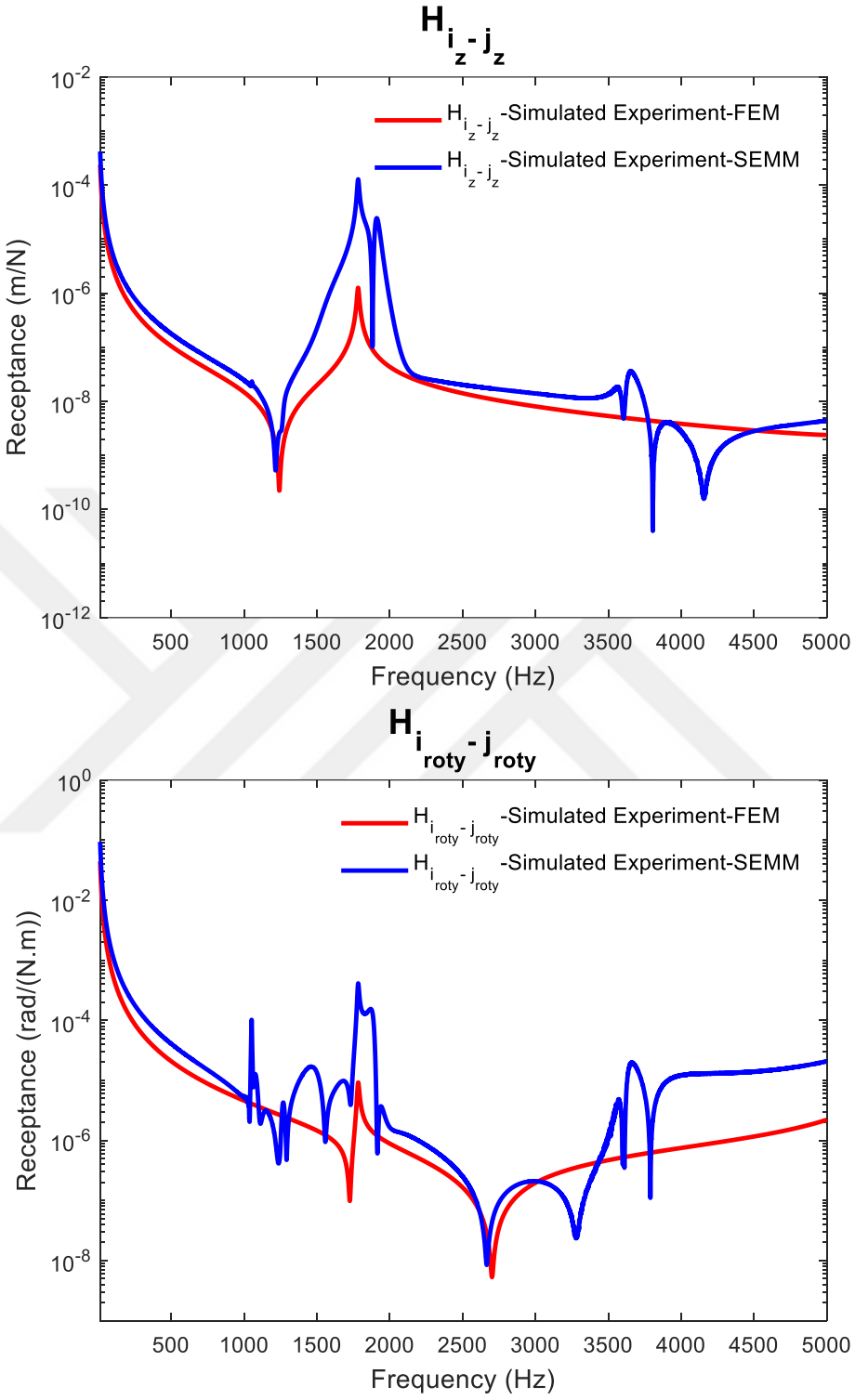


Figure 4.11 Obtained contact face FRFs via the SEMM Method

Cross-FRF terms are not included in the model

Cross-FRF terms in the boundary are excluded. The term in Equation (4.9) is included as given below. The obtained SEMM results are shared in Figure 4.12.

$$\left[H_{par}^{rem} - H^{ov}\right] = \begin{bmatrix} \left[H_{P_Z P_Z}{}_{all}^{rem-ov}\right] & 0 \\ 0 & \left[H_{P_{RotY} P_{RotY}}{}_{all}^{rem-ov}\right] \end{bmatrix} \tag{4.10}$$

Only $H_{P_{4Z} P_{4RoY}}{}_{all}$ -Cross FRF terms are included in the model

Only $H_{P_{4Z} P_{4RoY}}{}_{all}$ Cross FRF terms in the boundary are included. The term in Equation (4.9) is equal to the matrix below. The obtained results are given in Figure 4.12.

$$[H_{ov}^{rem} - H^{ov}] = \begin{bmatrix} \left[H_{P_Z P_Z}{}_{all}^{rem-ov}\right] & \begin{bmatrix} 0 & 0 & 0 \\ 0 & 0 & 0 \\ 0 & 0 & H_{P4ZP4RotY}{}^{rem-ov} \end{bmatrix} \\ \begin{bmatrix} 0 & 0 & 0 \\ 0 & 0 & 0 \\ 0 & 0 & H_{P4ZP4RotY}{}^{rem-ov} \end{bmatrix}^T & \left[H_{P_{RotY} P_{RotY}}{}_{all}^{rem-ov}\right] \end{bmatrix} \tag{4.11}$$

Only $H_{P_{4Z}\,P_{4RoY}\,all}$ and $H_{P_{3Z}\,P_{3RoY}\,all}$ Cross-FRF terms are not included in the model

The term in Equation (4.9) becomes like Equation (4.12). The obtained results are given in Figure 4.12.

$$[H_{ov}^{rem} - H^{ov}] = \begin{bmatrix} & & \left[H_{P_Z\,P_Z\,all}{}^{rem-ov}\right] \\ \begin{bmatrix}0\\0\\0\end{bmatrix} & \begin{matrix}0\\ H_{P3ZP3RotY}{}^{rem-ov}\\0\end{matrix} & \begin{matrix}0\\0\\ H_{P4ZP4RotY}{}^{rem-ov}\end{matrix} \end{bmatrix}^{T} \cdots$$

$$\cdots \begin{bmatrix}0\\0\\0\end{bmatrix} \begin{matrix}0\\ H_{P3ZP3RotY}{}^{rem-ov}\\0\end{matrix} \begin{matrix}0\\0\\ H_{P4ZP4RotY}{}^{rem-ov}\end{matrix} \Bigg] \Bigg] \\ \left[H_{P_{RotY}\,P_{RotY}\,all}{}^{rem-ov}\right]$$

(4.12)

It becomes evident that the SEMM method may produce unrealistic and unacceptable results for points near the contact interface if the rotational dynamics are not accurately represented. However, when the displacement-moment FRF terms are not included in the SEMM method, the hybrid model aligns perfectly with the FEM counterparts at the contact face (Figure 4.12). As stated earlier, the effectiveness of the SEMM method relies on the term specified in Equation (4.9). In order to minimize discrepancies arising from this term, the FE model is constructed to match the translational FRF values of points P2 to P4. However, in the end, it is concluded that not only translational FRFs but also FRFs influenced by rotational inputs significantly impact the results. Upon examining the approximated rotational FRF results, the rotational FRF value of P2 is highly deviated from their FEM counterparts, as seen in Figure 4.5. Due to this differentiation, FRFs obtained from SEMM and their FEM counterparts have significant differentiation in the translational direction. To address the reason behind that disparity, the order of the

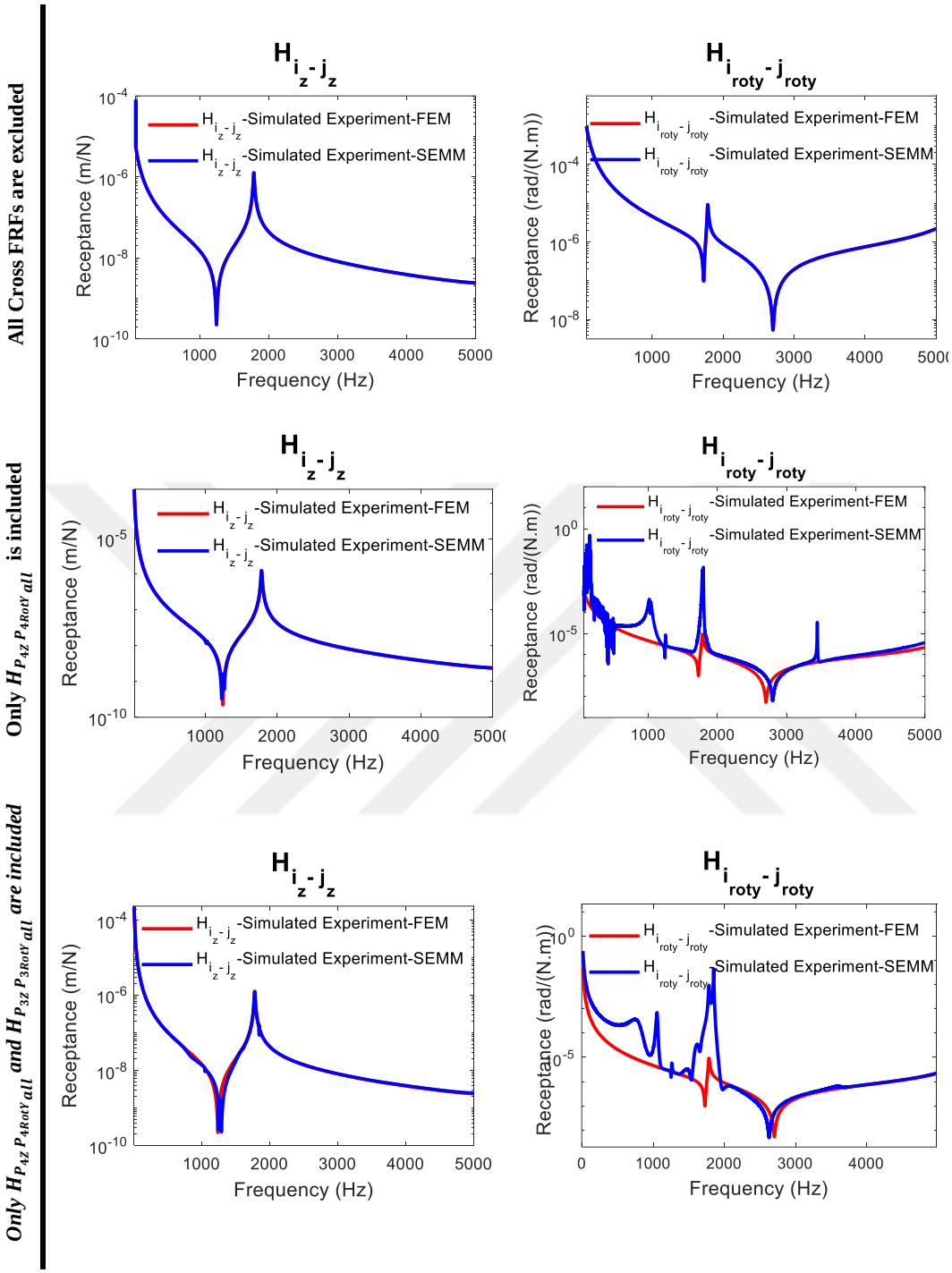


Figure 4.12. Obtained contact face FRFs via SEMM Method (for different cross FRFs)

applied FDT is looked at closer, and to check if the order of the technique changes the results, the first-order expansion technique [33] is applied, and the FRF results are shared in Figure 4.13.

4.3.2 Effect of Finite Difference Technique on Hybrid Model

In this section, first-order FDT findings for the rotational FRF values of the P2 and P3 are implemented in the SEMM equation instead of their second-order equivalents to obtain the hybrid model. The first-order approximation findings are shown in Figure 4.13. When the results for P2 and P3 are evaluated, the FRFs produced for the FDT's first-order approximation follow the FEM results better than the FRFs obtained for the FDT's second-order approximation. P4's rotational FRF differs significantly from its FEM counterparts. According to those findings, first-order FDT results are used for rotational FRFs at points P2 and P3, and second-order results are only used for point P4. The newly obtained rotating FRFs are used in Equation (4.8) to get another hybrid model called *'Simulated Experiment-New'* in the comparison graphs. The new-generated hybrid model is represented and compared to the hybrid model created in Section 4.3.1 in Figure 4.14. Also, those FRFs are compared with their FEM counterparts in Figure 4.15. The difference between the parent and the overlay model makes obtaining completely matching FRFs impossible. Besides, it is important to note that regardless of the stiffness values identified, obtaining such misbehaved FRFs is impossible, as in Figure 4.14, without committing FE modeling errors. That is why a new modeling approach is accepted and used in identification studies. Section 4.4 goes into detail about this method.

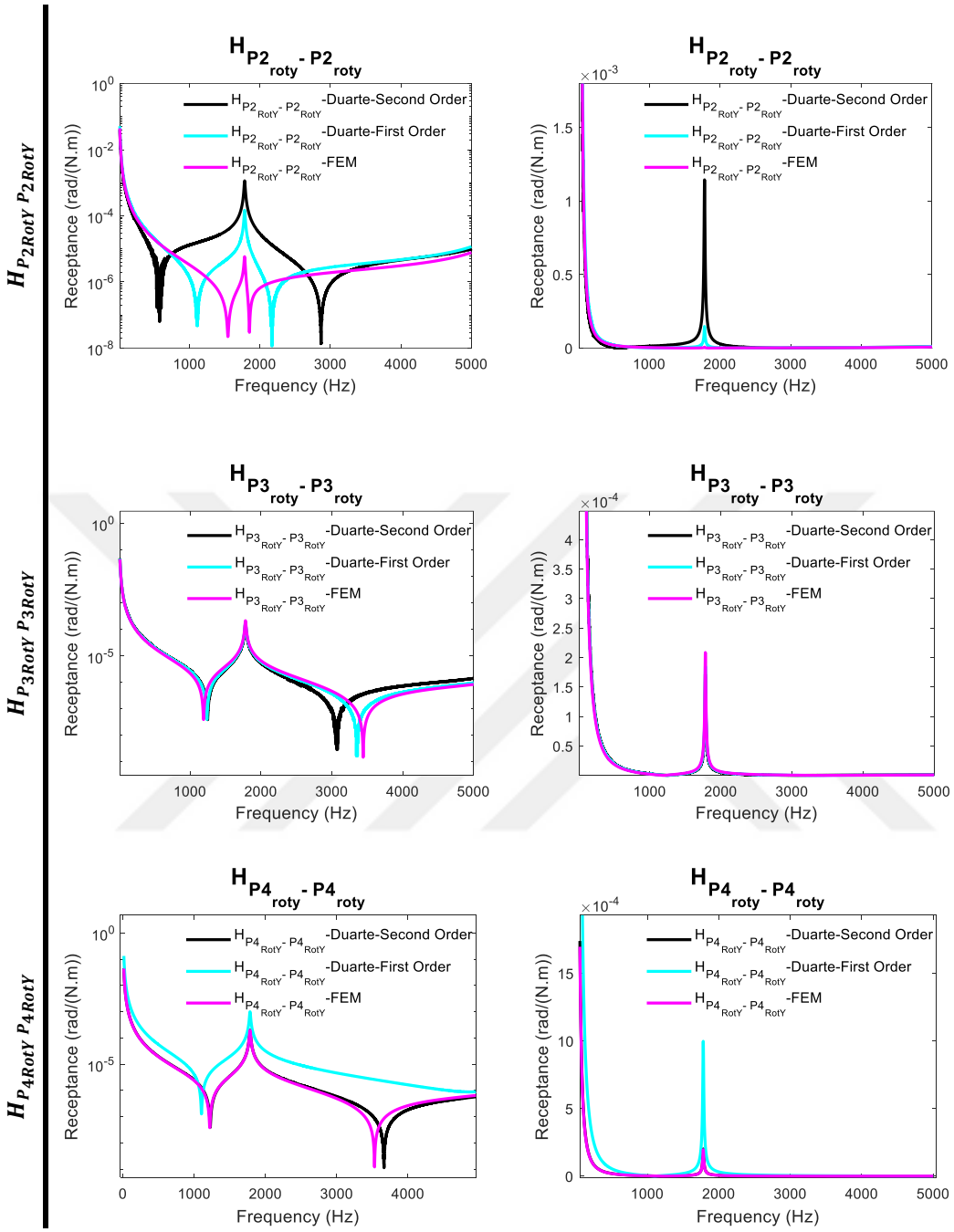


Figure 4.13. Rotational FRFs for different order Finite Difference Technique (log scale (left), linear scale(right).

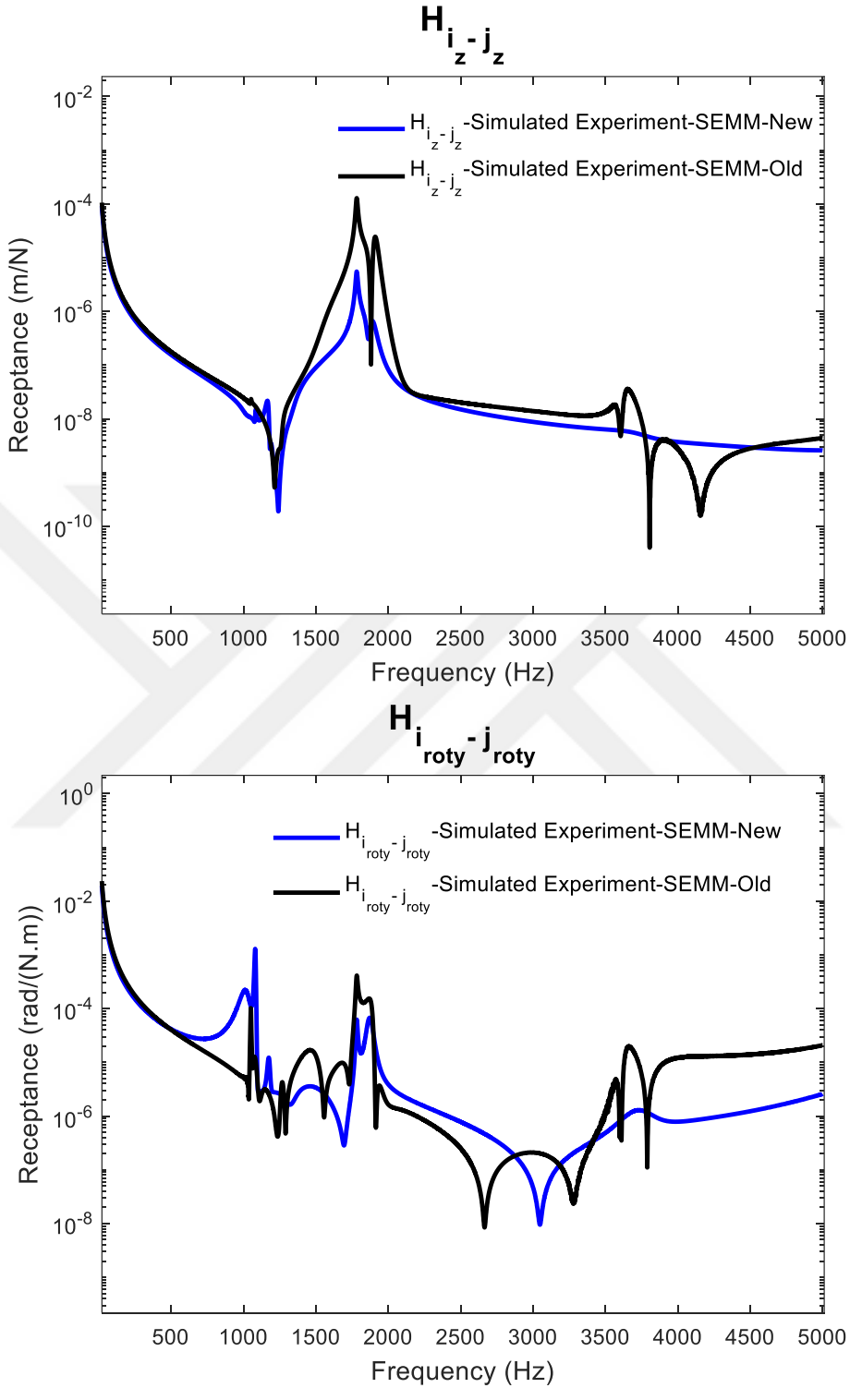


Figure 4.14 Comparison of Hybrid Models' translational (upper) and rotational (lower) FRFs

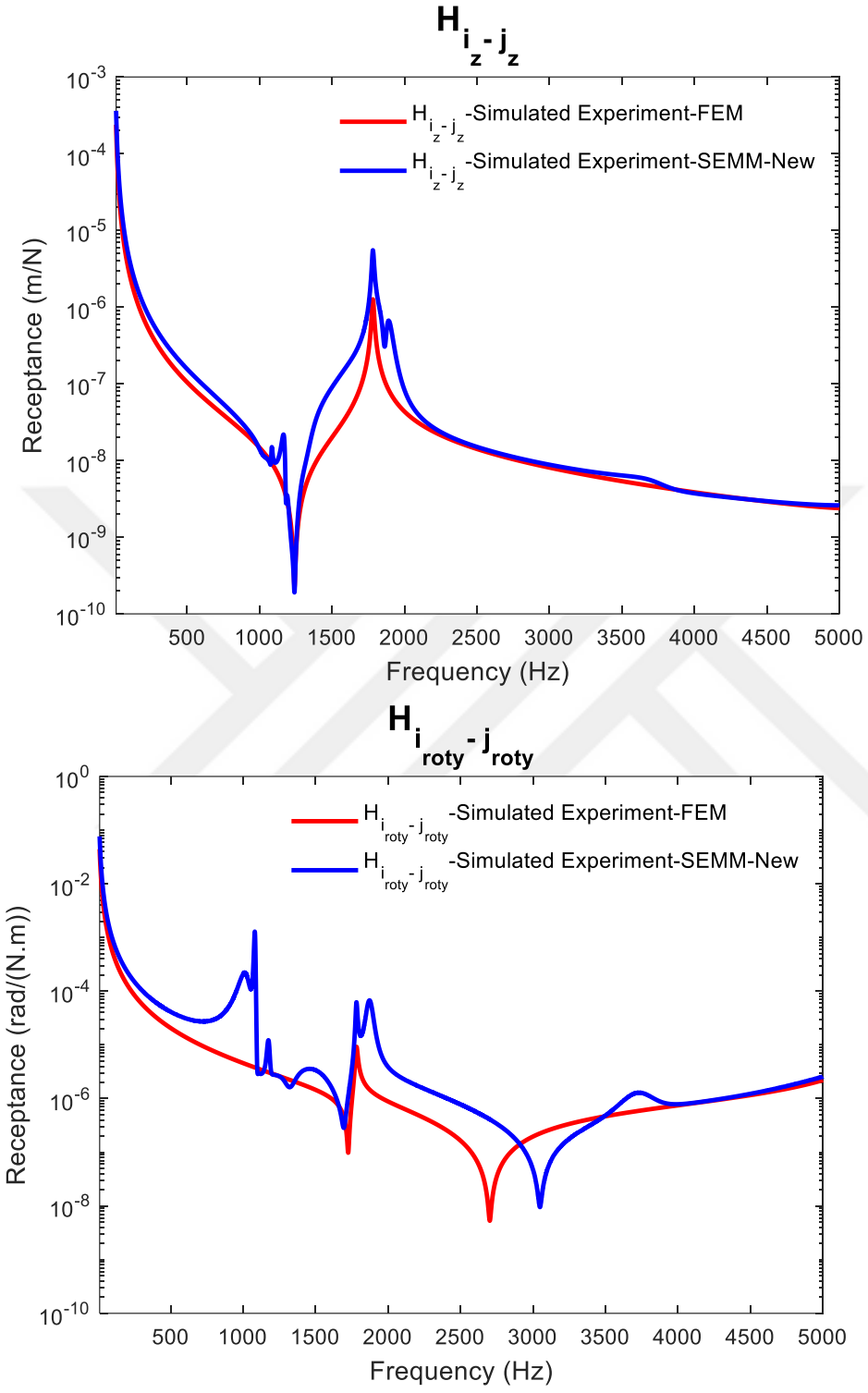


Figure 4.15 Comparison of the contact faces' translational (upper), and rotational (lower) FRFs for FEM and SEMM models

4.4 New Simulated Experiment Model: ISMM Methods via the Closest Points of the Holder and Extension to the Contact Face

Section 4.3 and its subsections investigate the possible issues that prevent SEMM from obtaining well-behaved FRFs. After the investigation, it was concluded that the SEMM Method does not provide reliable FRF values that can be used in ISMM to identify stiffness values. So, in this section, new application points for ISMM, which are the closest points of the holder and extension to the contact face, are selected. The selected points are shown in Figure 4.16. Those points are P2 and P3. Unlike the model given in Section 4.1, the locations of P2 and P3 are selected 5 mm away from the contact faces in that section. Since new selection is applied, the translational FRFs of those points are compared with their experimental counterparts, which are given in Section 5.1 (Figure 4.17). Moreover, they are still close enough to say the points represent almost the same behavior as the experimental results.

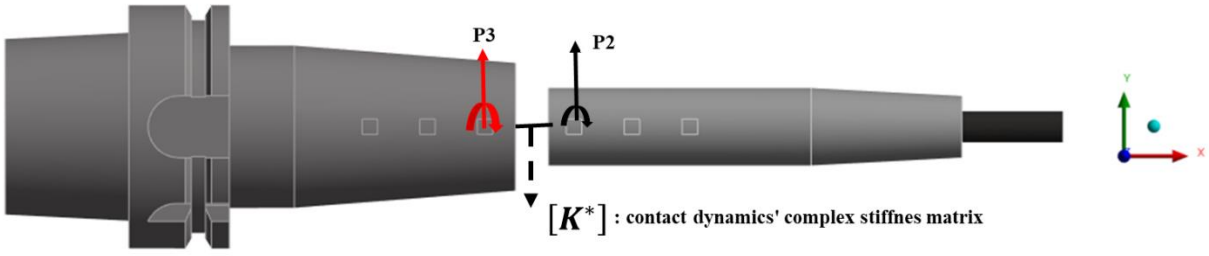


Figure 4.16 Closest Points (P2 and P3) for ISMM Application

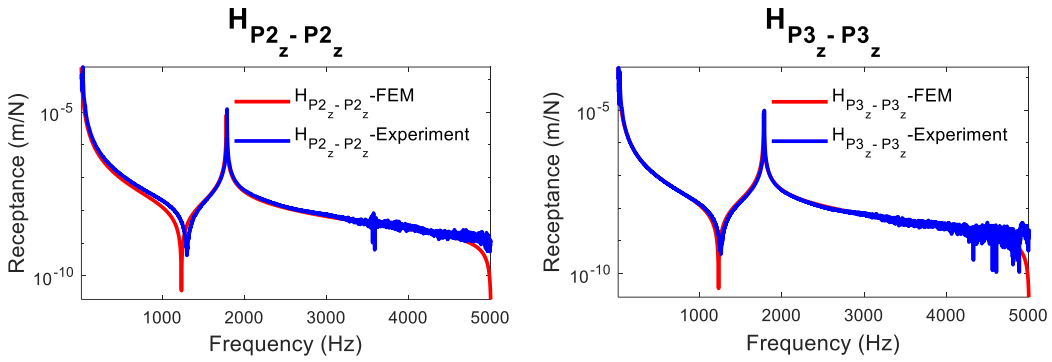


Figure 4.17 Comparison of the FRF at the new P2 and P3 with their experimental counterparts

The details of the simulated experiment model are kept the same as described in Section 4.1. As in the previous section, two simulated experiment-real models are created. These models are as follows:

- ***FEM***: In this model, both translational and rotational FRFs needed in the ISMM (Equation (2.72) are obtained from the ANSYS FE simulation.
- ***Duarte***: In this model, only the translational FRFs needed in ISMM's Equation (2.72) are obtained from the ANSYS FE simulation. The FRFs of the points P2 and P3, which have rotation effects, are approximated through the finite difference technique [33].

For the *Duarte Model*, the obtained rotational FRFs are given in Figure 4.18 and Figure 4.19. For P2 and P3, rotational FRFs are obtained using the 1st and 2nd-order finite difference techniques. The rotational FRFs' results obtained from the 1st order FDT formula are named the *Duarte Model* and selected to apply ISMM. The assumed model is the same as the one outlined in Table 3-1. Only the rotational stiffness value changed as 1E+05 (N.m)/rad. By doing that, it also aims to show the effects of the assumed model changing the simulation results.

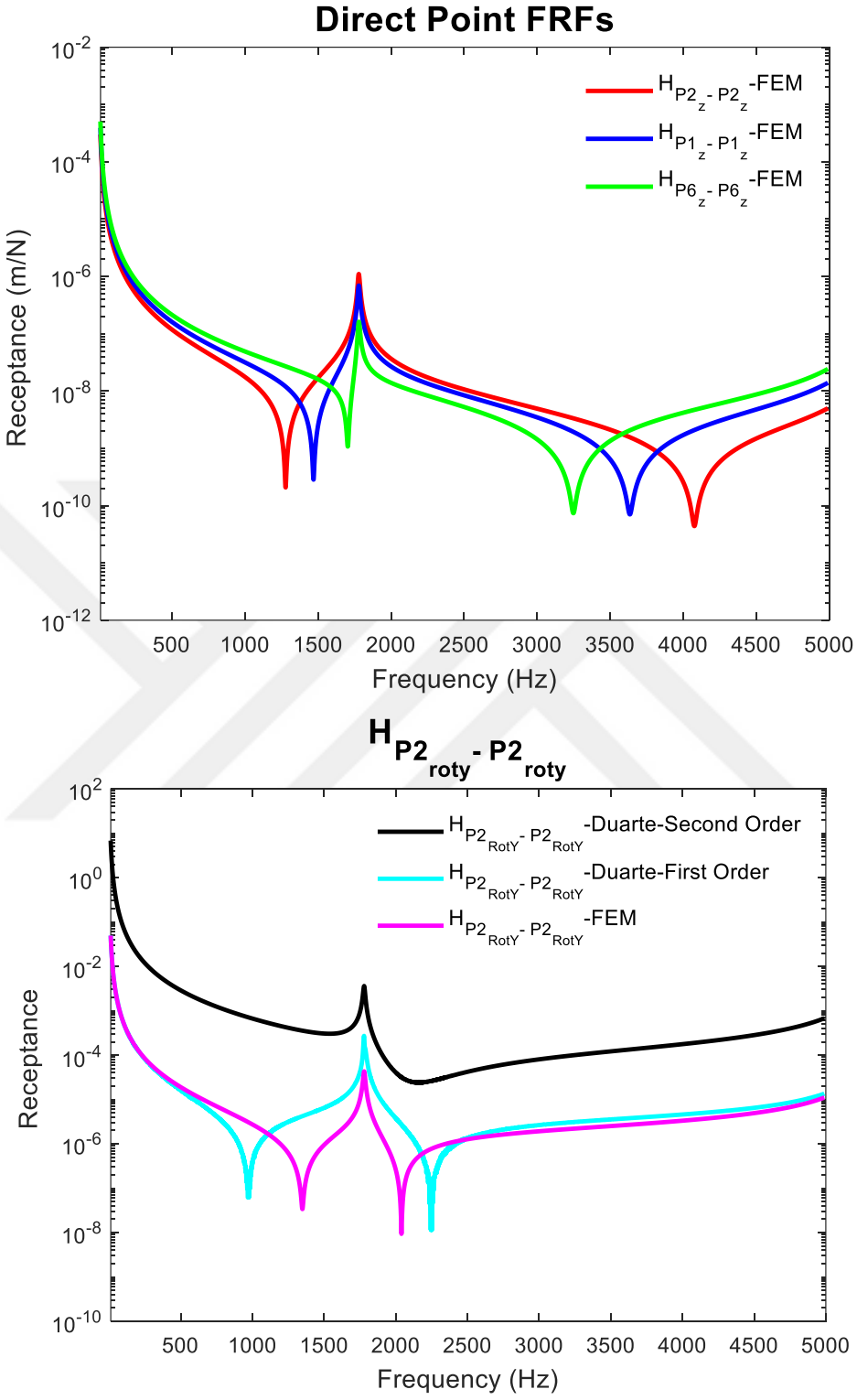


Figure 4.18 Translational FRFs used in FDT (upper) and obtained rotational FRFs for Simulated Experiment and Duarte Models' Rotational FRFs at P2

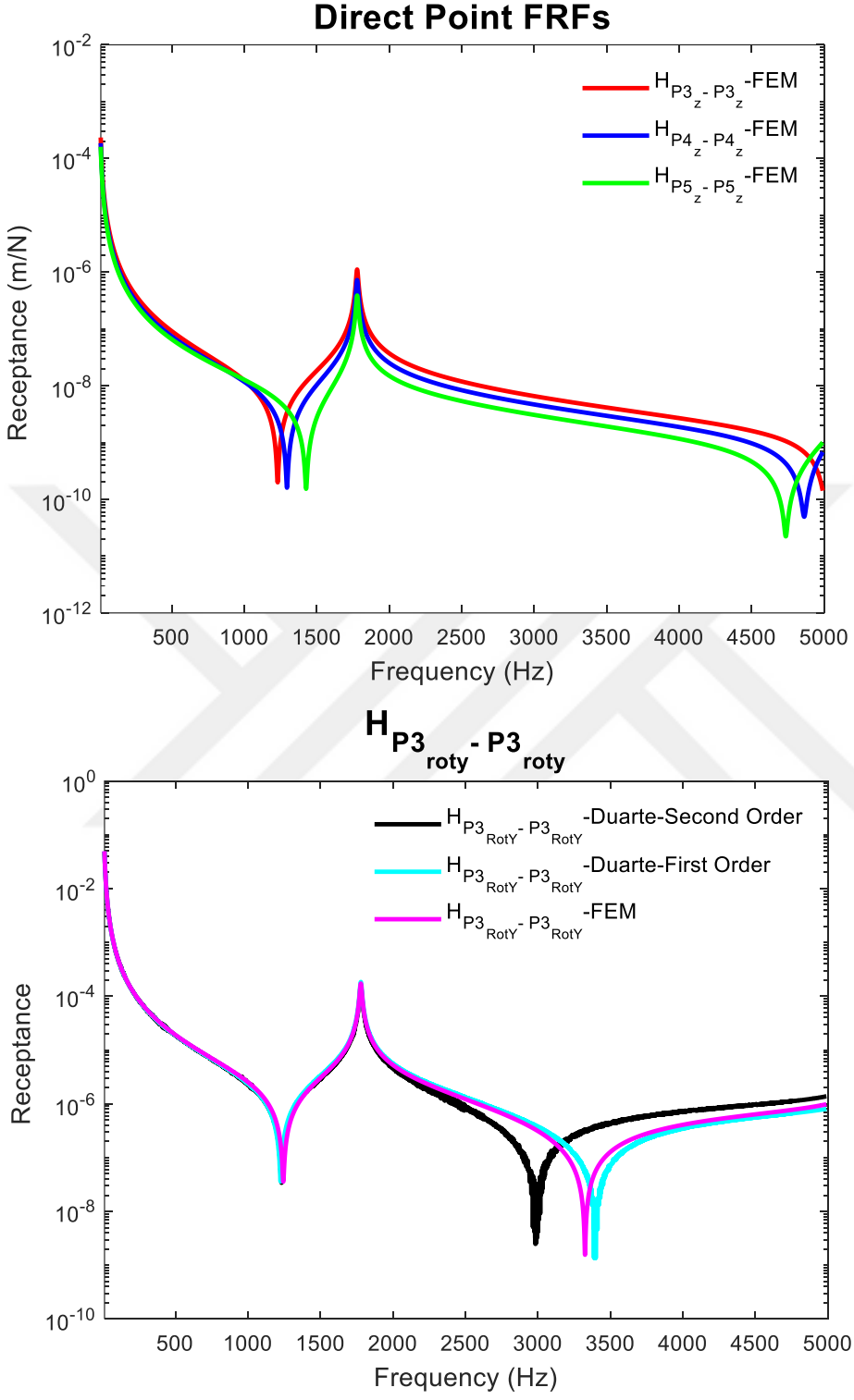


Figure 4.19 Translational FRFs used in FDT (upper) and obtained rotational FRFs for Simulated Experiment and Duarte Models' Rotational FRFs at P3

After both the *Actual (FEM and Duarte)* and *Assumed Models* are determined, the ISMM method is applied to obtain the contact dynamics' translational and rotational stiffness values. Firstly, the identification regions are determined based on the effective frequency of the stiffness values. That is because, as seen in Figure 4.18 and Figure 4.19, the rotational FRFs of the *Duarte Model* differ significantly from *Assumed* counterparts since their results are not from the same calculation method. The comparison of the FRFs at P2 and P3 for *Assumed, FEM,* and *Duarte Models* are shared in Figure 4.20Figure 4.21, respectively. Thanks to the studies executed in Chapter 3, it is concluded that the first natural frequency is mainly affected by rotational stiffness value, whereas the translational stiffness value is effective on the second natural frequency; based on Figure 4.18 and Figure 4.19, the ranges are summarized in Table 4-3. It is worth mentioning that identification ranges rely on the *Duarte Model*, *FEM Model* results are only shared how they are close to each other. So, identification from the *FEM Model* is also done in the same ranges as the *Duarte Model.*

Table 4-3 Sensitivity Regions for Closest Points Application

Stiffness Direction	**Sensitivity Region**
$\mathbf{k_{Fx}}$	4620-4700 Hz
$\mathbf{k_{M\theta y}}$	1740-1820 Hz

The identified translational stiffness values of both models are shared in Figure 4.22 and Figure 4.23. When the identified translational results are looked at, the values change in the order of E-02, so the identified stiffness value is calculated as the mean of the stiffness values given in Figure 4.22- Figure 4.23.

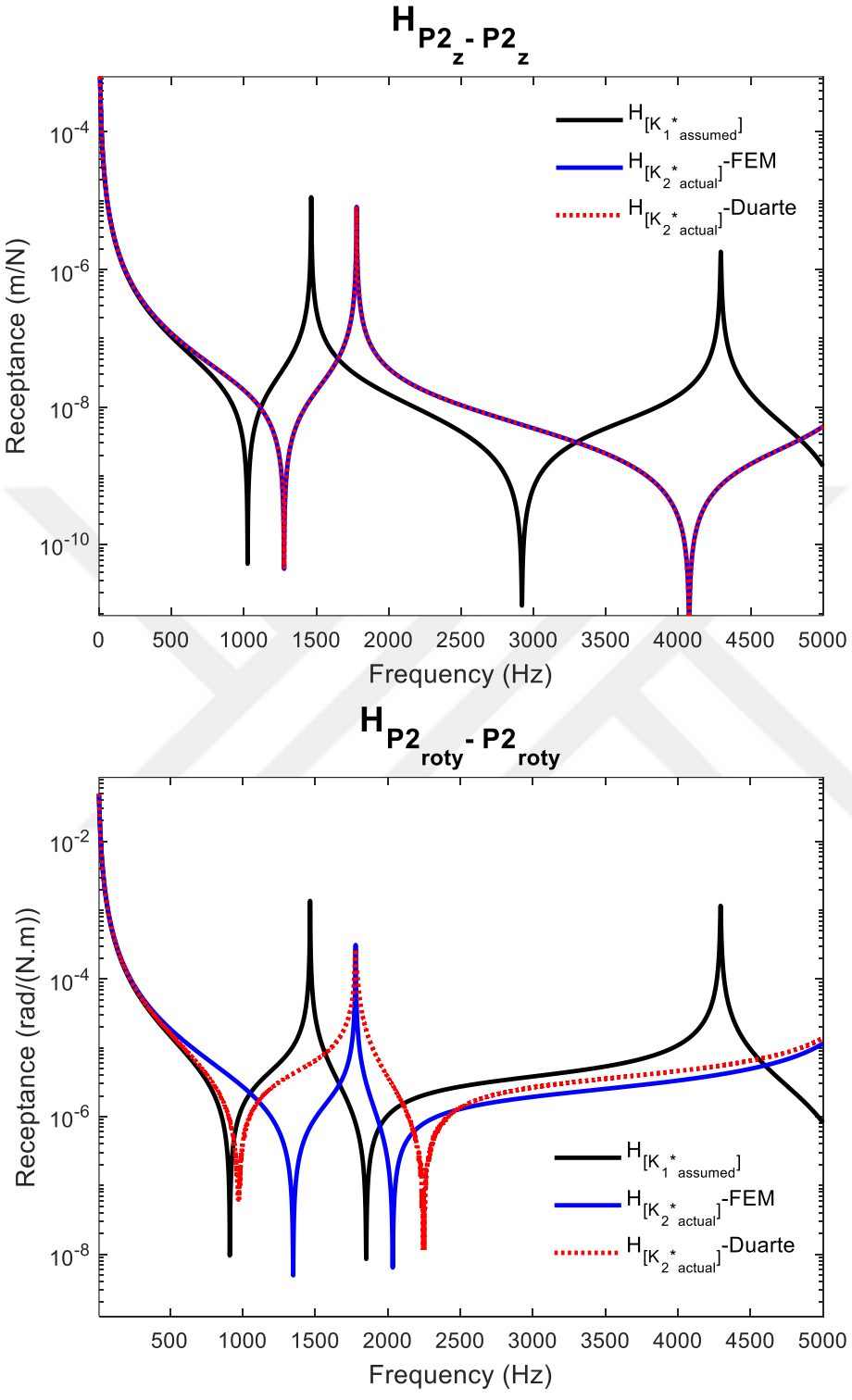


Figure 4.20 Direct translational and rotational FRFs at P2 for assumed and actual models

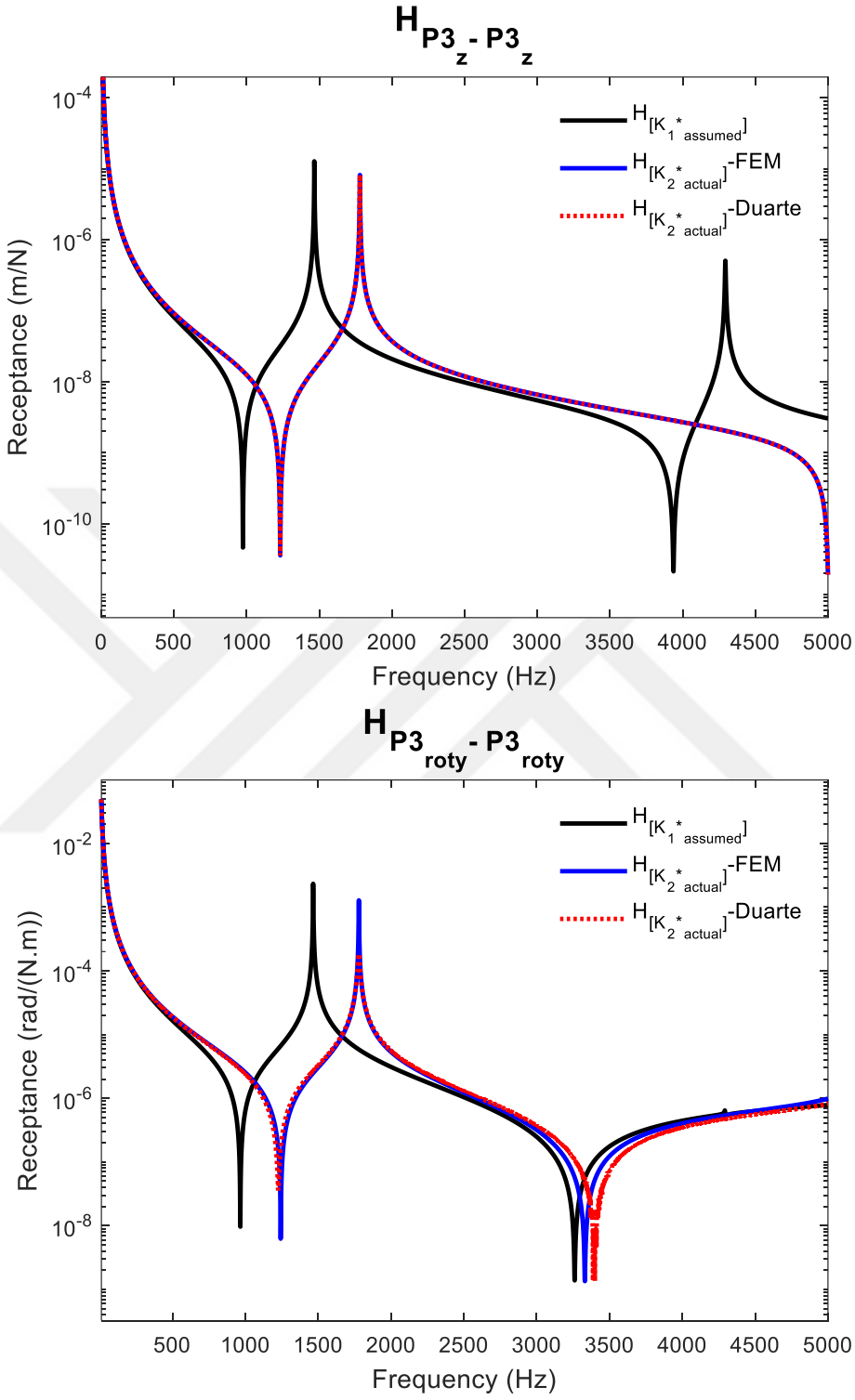


Figure 4.21 Direct translational and rotational FRFs at P3 for assumed and actual models

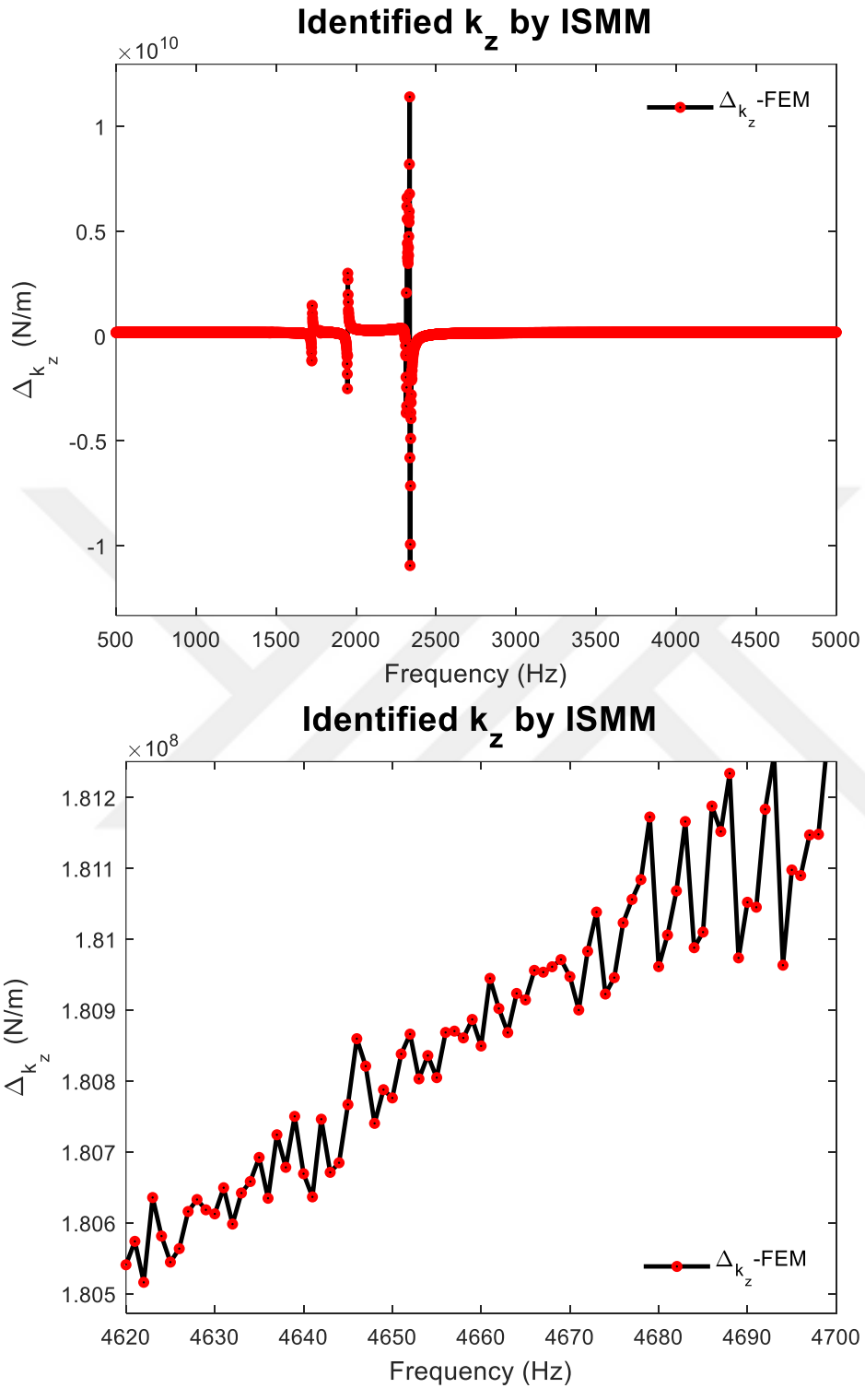


Figure 4.22 Identified stiffness value of k_Z −FEM Model

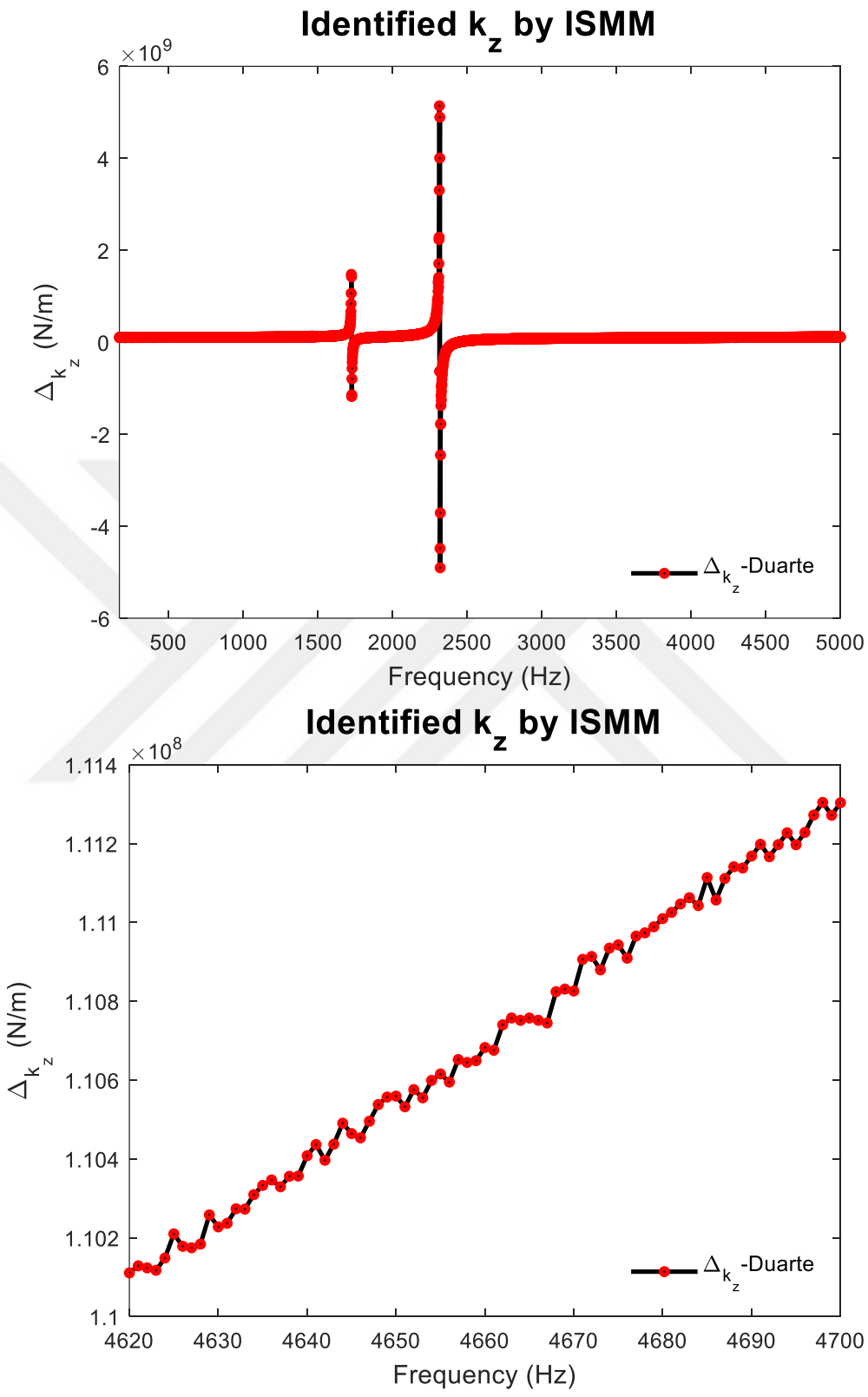


Figure 4.23 Identified stiffness value of k_Z −Duarte Model

Unlike identified translational values, identified rotational stiffness values in Figure 4.24 and Figure 4.25 differ significantly, so the identification range is decreased to 1770-1790 Hz, closer to the first natural frequency. In that new range, the identified rotational stiffness values are shared in Figure 4.26. The results of the *FEM Model* are still changing significantly, so instead of taking the mean of the values in Figure 4.24, the identified stiffness value at first natural frequency (1799 Hz) is directly taken into consideration.

When Figure 4.26 is examined, it is seen that the values for the *Duarte Model* are still changing between the ranges of the graph. To continue the identification, the mean value of those data is considered, and the identification results are shared in Table 4-4. Nevertheless, looking at the variation of the identified natural frequencies is essential if the highest or the lowest values in Figure 4.26 are selected. When identified stiffness models are used in the FE model, it is seen that the error of the identified first natural frequency changes from 0.51% to 1.57%, whereas the second natural frequency changes from 1.09% to 0.82% for the *Duarte Model.* Therefore, it is concluded that taking the mean of the identified rotational stiffness values does not affect the identified system response significantly. So, the mean of the identified values in Figure 4.26 is considered the rotational stiffness value for the *Duarte Model*. Identified stiffness values and identification errors are shared in Table 4-5 and Table 4-6.

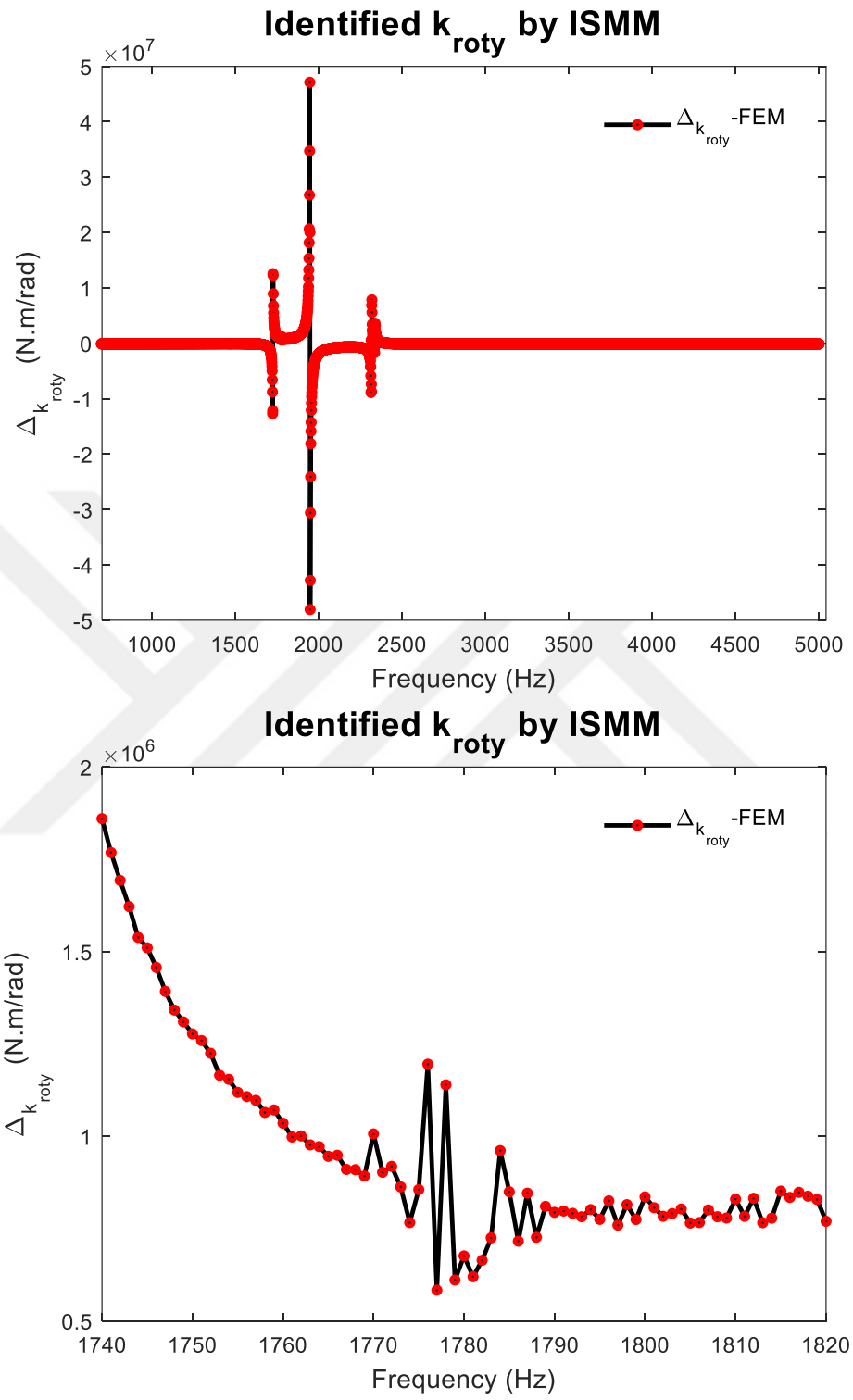


Figure 4.24 Identified stiffness value of k_{RotY} −FEM Model

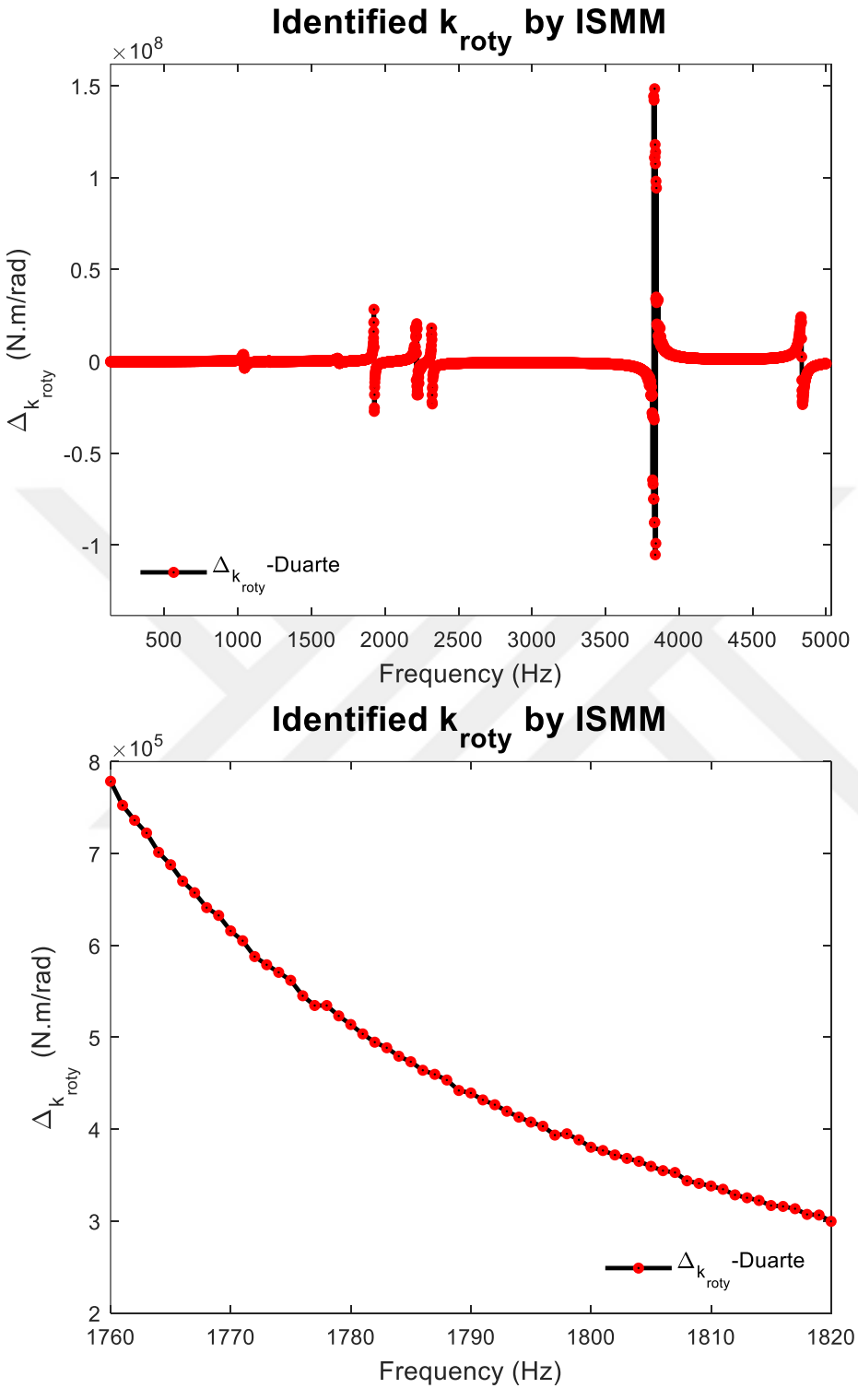


Figure 4.25 Identified stiffness value of k_{RotY} −Duarte Model

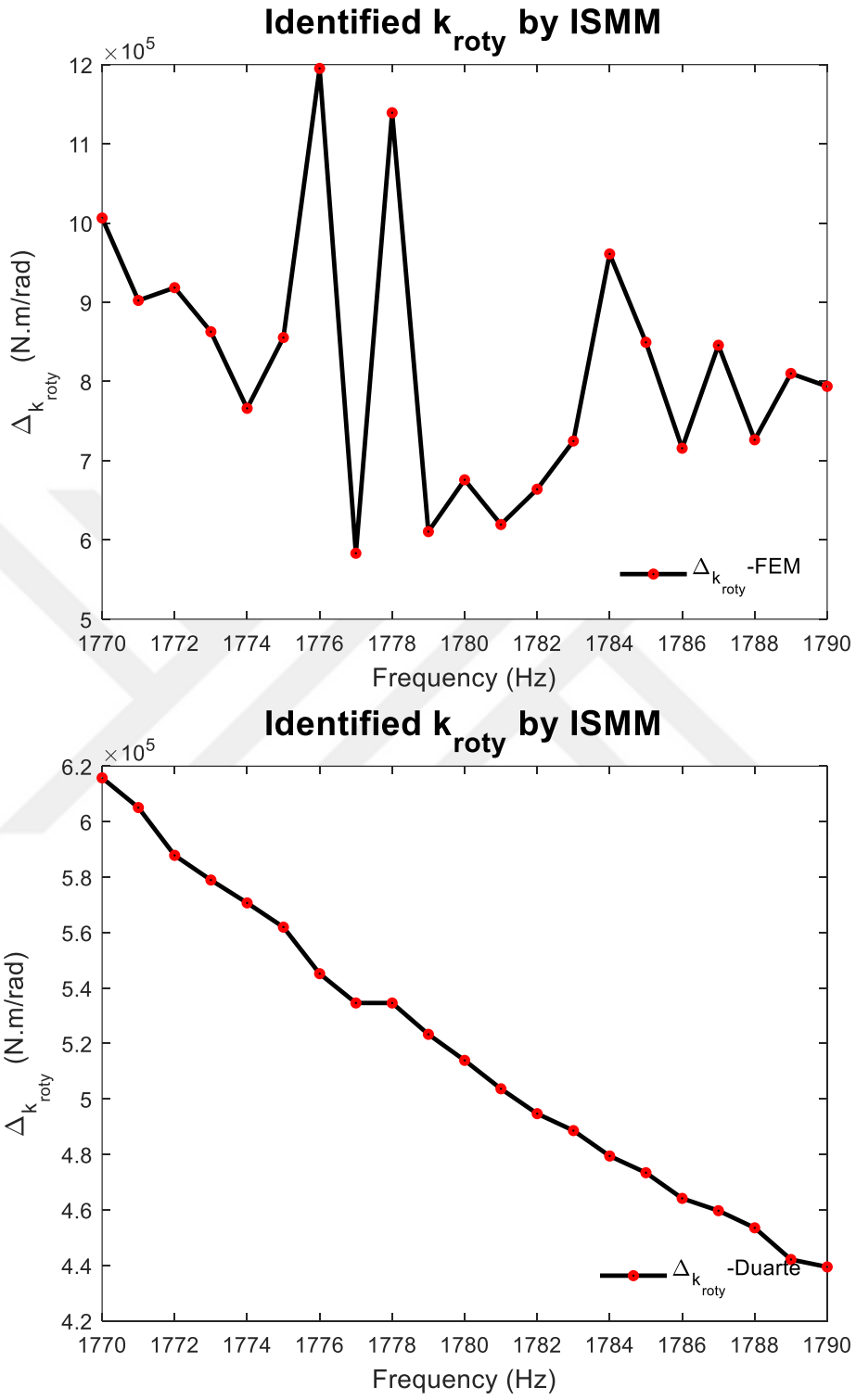


Figure 4.26 Identified stiffness value of k_{RotY} − FEM (upper) Duarte (lower) Models

Table 4-4 Identified stiffness values for different frequency ranges

Stiffness Directions	Identified Stiffness Values		Abs-Error (%)	
	ISMM with Exact RDOF	ISMM with App. RDOF (Duarte)	ISMM with Exact RDOF	ISMM with App. RDOF (Duarte)
$\mathbf{k_{Fz}}$ (N/m)	2.81E+08	2.11E+08	17.08	**12.08**
$\mathbf{k_{M\theta y}}$ (N.m/rad)	7.50E+05	6.21E+05	66.66	**38.00**
Actual Stiffness Values Used in Simulated Experiment				
$\mathbf{k_{Fz}}$ (N/m)	2.40E+08			
$\mathbf{k_{M\theta y}}$ (N.m/rad)	4.50E+05			

As seen from Table 4-4, the identified rotational stiffnesses errors are high, especially for the *FEM Model* rotational stiffness values. It is worth noting that the *FEM Model* gives good agreement in Section 3, but here, the identification ranges are determined by only considering the *Duarte Model*. Hence, the *FEM Model* results can change if the same identification ranges as in Section 3 are used. However, the main goal of the ISMM is to obtain a stiffness matrix that represents the actual dynamics of the assembly as closely as possible. Because the exact values of the stiffnesses are unknown in experimental studies, the effectiveness of the identified values can be checked by comparing the identified natural frequencies to experimental results. In Table 4-5 and Table 4-6, the identified natural frequency errors are around 1%. That implies that the identification gives reliable results to represent the actual dynamics of the HET assembly.

Table 4-5 Identified natural frequencies for different identification models

Model	Modes (Hz)	
	1st	**2nd**
Identified Model by ISMM- FEM	1812	5396
Identified Model by ISMM- Duarte	1799	5258
Actual Model (Simulated Experiment)	1779	5302

Table 4-6 Errors of the identified natural frequencies

Model	Absolute Error of Identified Modes (%)	
	1st	**2nd**
Identified Model by ISMM- FEM	1.86	1.77
Identified Model by ISMM- Duarte	**1.12**	**0.83**

Through two sets of identified stiffness matrices, ANSYS FE simulations are repeated and compared with the *FEM Model* FRFs, and the results are shown in Figure 4.27.

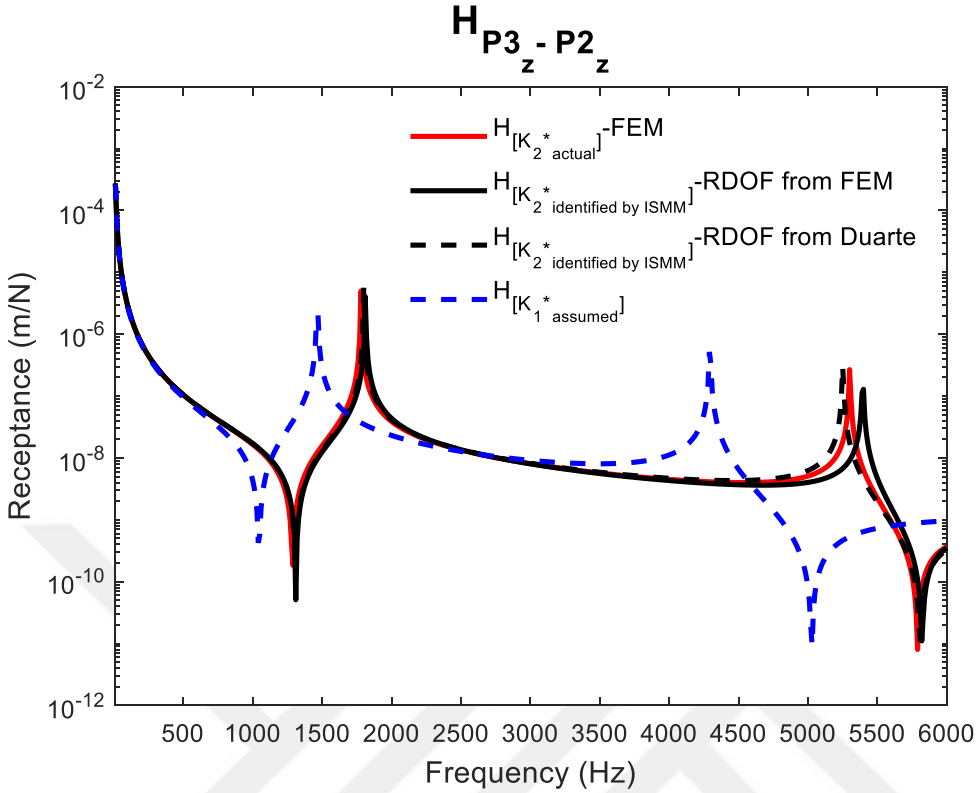


Figure 4.27 Obtained FRFs with identified stiffness values

The identified FRFs of both the *FEM* and *Duarte Models* are found to be close to their actual-simulated experimental counterparts around both the first and second natural frequencies. When the identification results are examined, it is clear that the difference in rotational stiffness values between the *FEM* and *Duarte Models* has no significant effect on the identified modes (Table 4-6) and the FRFs (Figure 4.27).

4.5 Effects of ANSYS FE Modeling Boundary Conditions on FDT Results

In Section 4.4, while the rotational FRF results from FDT and FE simulation are nearly identical at P3, they are not remarkably similar at P2. The reason behind that is the discrepancy in the spring definition faces in the FE simulation. This section details this difference with the narrow contact face definition.

Section 4.4 presents the spring definition for the contact face dynamic, as shown in Figure 4.28. This definition is based on faces with the same diameter as the extension. However, the contact face definition has now been limited to a 4 mm diameter region, as illustrated in Figure 4.29. All the other modeling details of the narrow contact face model are the same as the one named the actual model in Section 4.4. With this new model, the identification of the rotational FRFs at P2 and P3 through FDT is repeated, and the results are compared with their simulated experimental counterparts in Figure 4.30 and Figure 4.31. As expected, the assembly has become more flexible due to the narrower spring regions, resulting in a decrease in the assembly modes.

The comparison between the rotational FRF results obtained through the first-order FDT and the simulated experimental results reveals that the matchings for P2 and P3 are almost identical, unlike the one mentioned in Section 4.4. This observation highlights the sensitivity of the applied approximation techniques, SEMM and FDT, to the boundary conditions in simulated experiments.

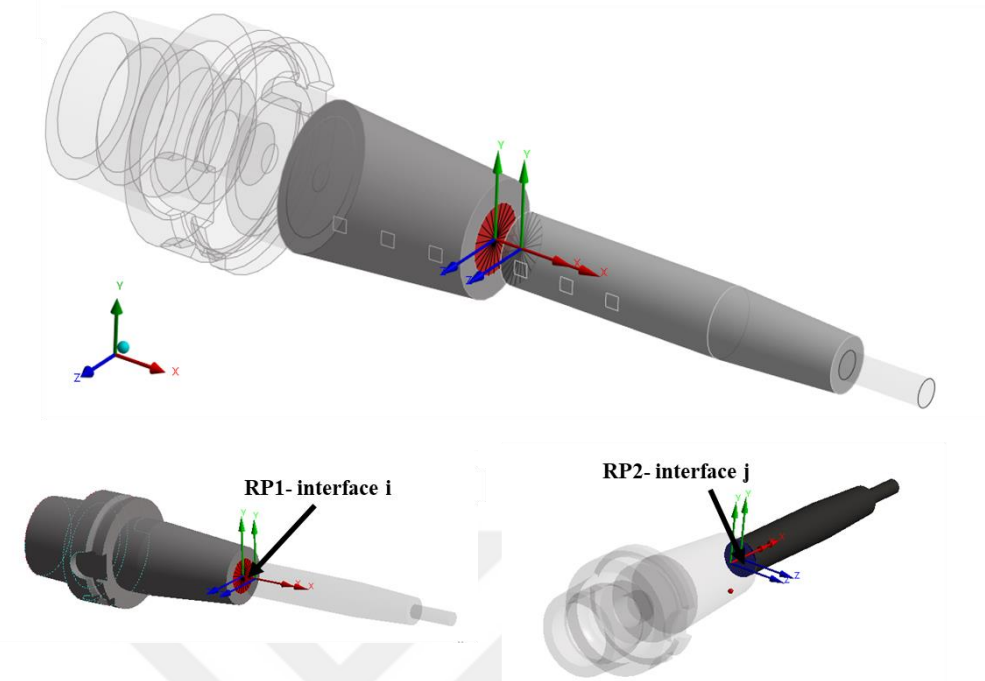


Figure 4.28 Contact face definition in $\emptyset = 10\ mm$

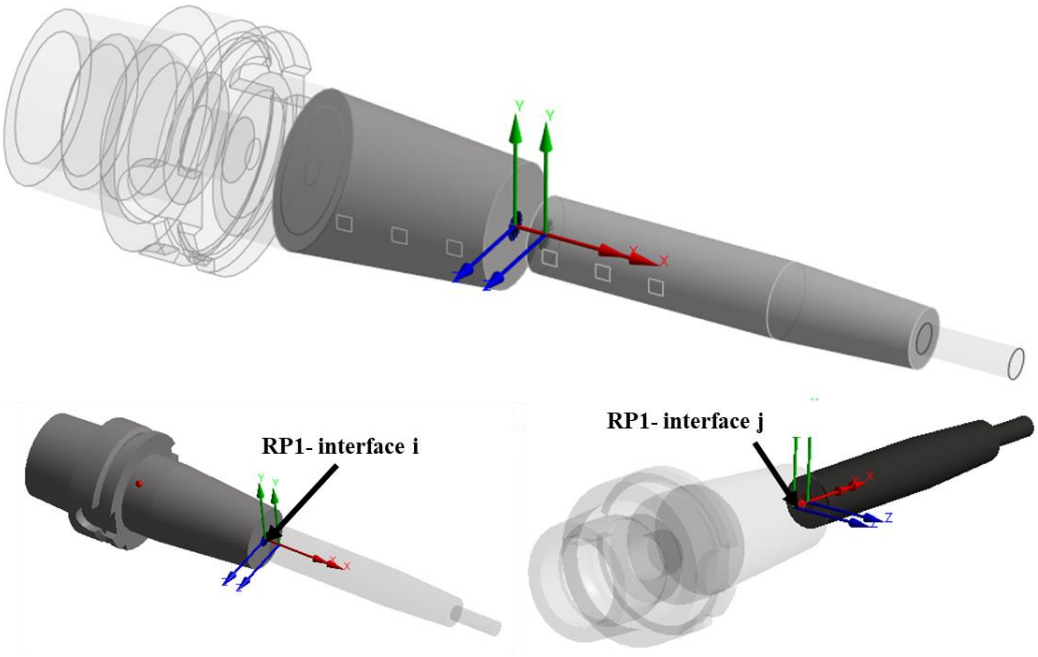


Figure 4.29 Contact face definition in $\emptyset = 4\ mm$

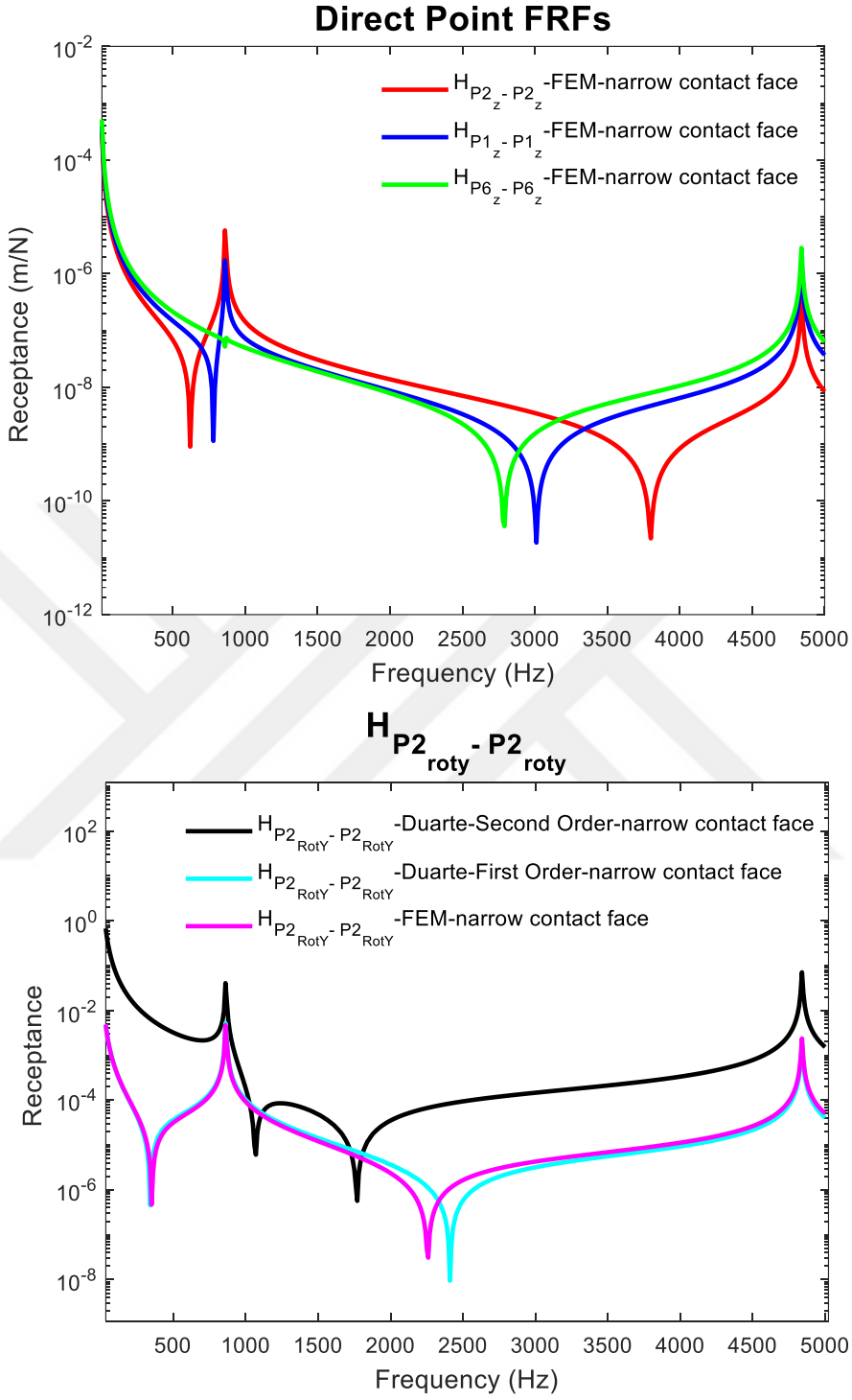


Figure 4.30 Translational FRFs used in FDT (upper) and rotational FRFs of the FEM and Duarte Models for P2 (lower)-narrow contact face model

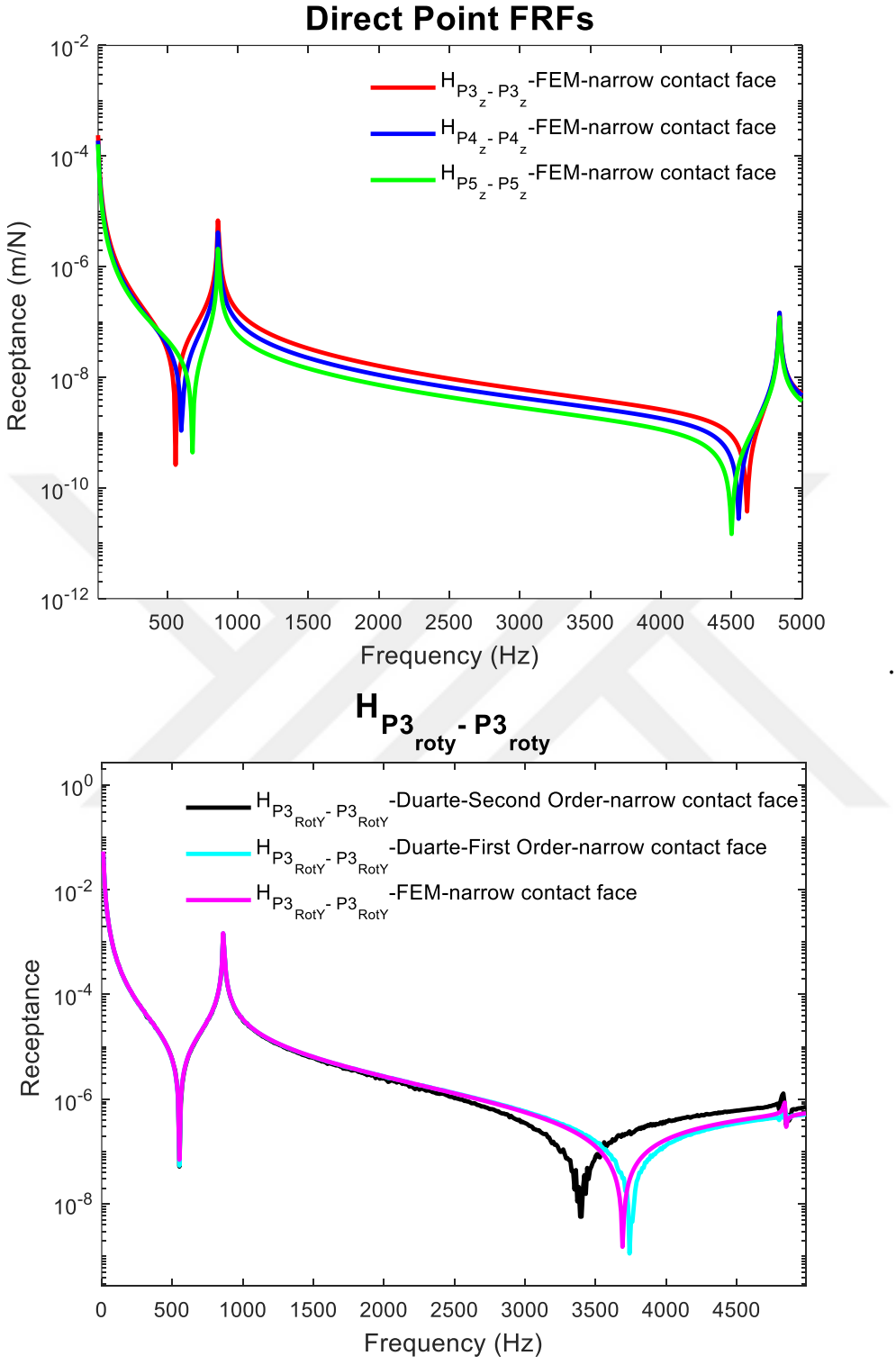


Figure 4.31 Translational FRFs used in FDT (upper) and rotational FRFs of the FEM and Duarte Models for P3 (lower)-narrow contact face model

4.6 Effects of Assumed Stiffness Properties on the ISMM

Until now, the ISMM has relied on a single assumed stiffness matrix model for identification studies. However, the sensitivity of the ISMM to the chosen assumed stiffness matrix model is an additional factor that impacts the overall applicability of the proposed method in contact dynamics identification. Hence, this section aims to examine the sensitivity of the ISMM to the selected assumed stiffness matrix model. This investigation mainly compares three sets of assumed stiffness matrix models. These sets are collected in Table 4-7. The assumed models primarily differ in terms of rotational stiffness values. When the assumed and actual models' FRFs in Figure 4.21 are looked at again, it is clear that, although half of the actual rotational stiffness value is accepted as the assumed rotational stiffness value, those FRFs still demonstrate a close resemblance, particularly around the first natural frequency. The first natural frequency is where the rotational degree of freedom significantly impacts. That is why all assumed stiffness sets in Table 4-7 have different rotational stiffness values and the same translational stiffness value. Cross-translational and rotational FRFs are represented in Figure 4.32. Comparison of those FRFs with their actual model equivalence are also represented in Figure 4.33. Figure 4.33 shows that when translational stiffness is constant, after 4.50E+05 (N.m/rad), the rotational value has no significant impact on the natural frequencies, mainly the first natural frequency.

Table 4-7 Assumed stiffness and damping values

Stiffness/ Damping Properties	**Assumed Stiffness Values**		
	Set 1	**Set 2**	**Set 3**
$\mathbf{k_{Fz}}$ (N/m)	1.00E+08	1.00E+08	1.00E+08
$\mathbf{k_{M\theta y}}$ (N.m/rad)	5.00E+04	1.00E+05	1.00E+06
Constant Structural Damping	0.001		

The identification procedures with the *Duarte Model* provided in Section 4.4 are now repeated for each assumed model, and the identified stiffness values and natural frequencies for each set are collected in Table 4-8 and Table 4-9, respectively. Since simulated experiment models are used, the effectiveness of the identified models is determined by comparing identified natural frequencies with their actual equivalent (Table 4-9), and identified natural frequency errors are represented in Table 4-10. Also, ANSYS FE simulations are run for each identification results in Table 4-8, and the obtained FRFs with identified stiffness values for each model are compared to their actual equivalents in Figure 4.34.

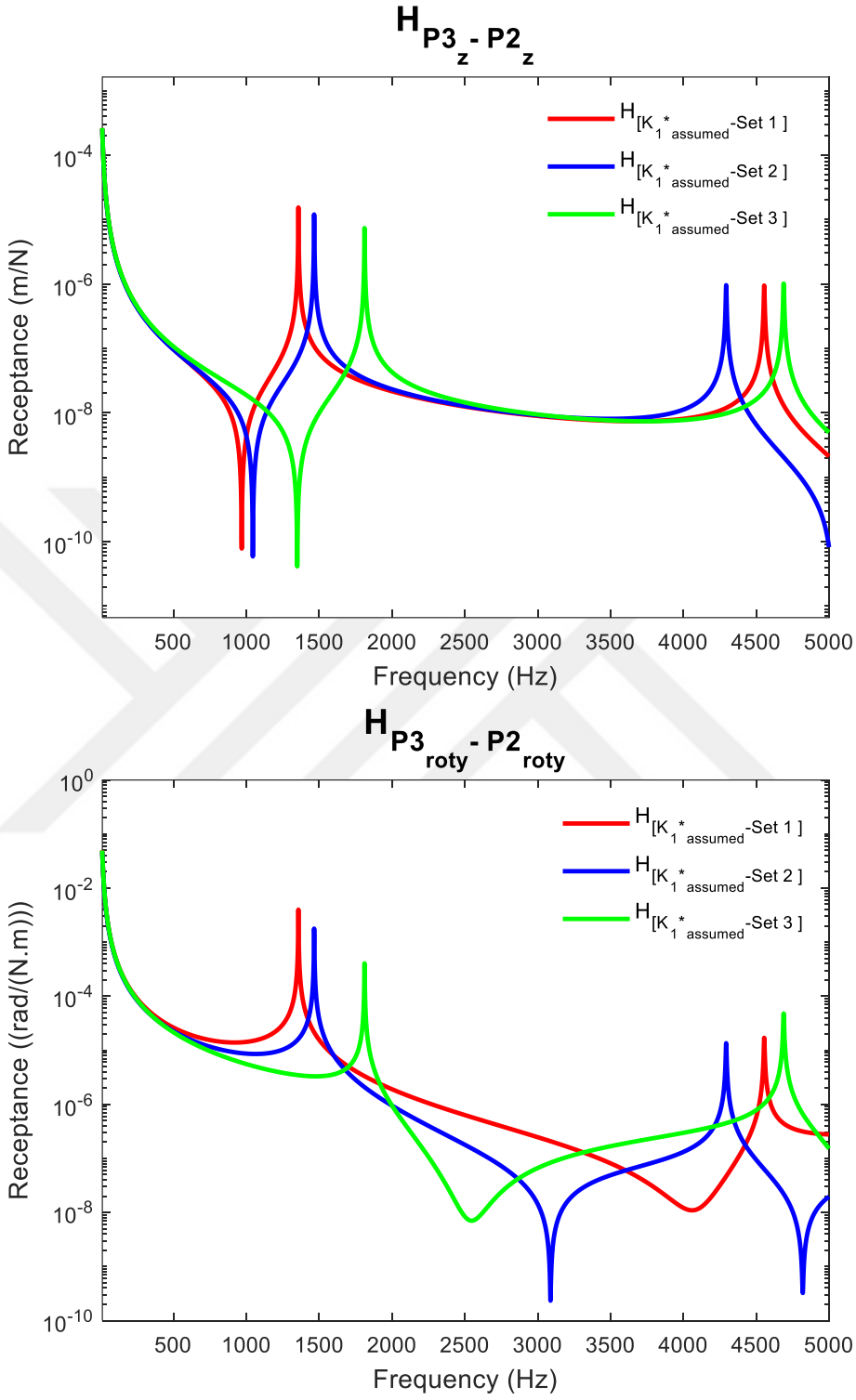


Figure 4.32 Translational and rotational FRFs for different assumed models

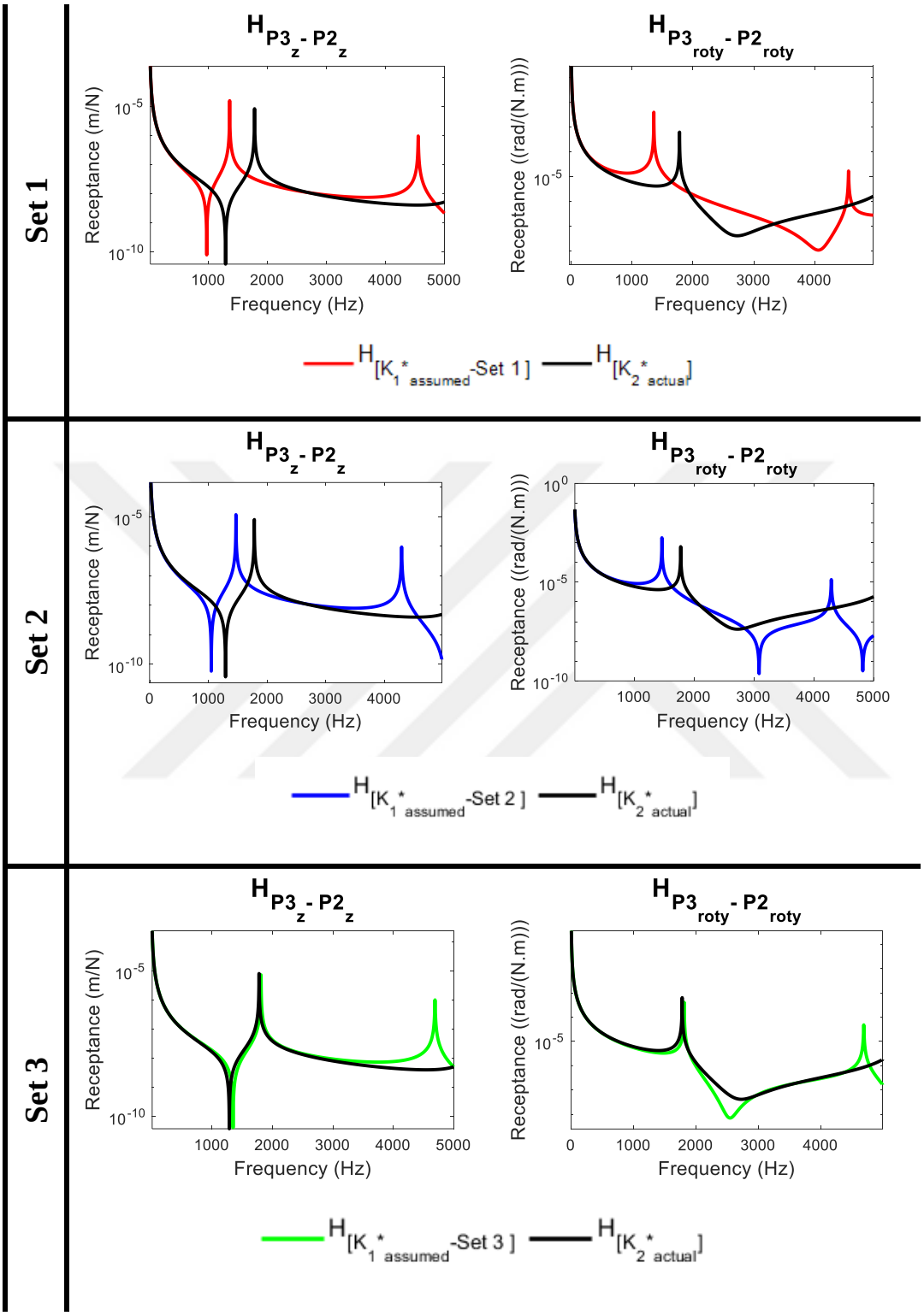


Figure 4.33 Comparison of assumed models to the actual model

Table 4-8 Identified stiffness values with three different assumed models

Stiffness Properties	**Identified Stiffness values by ISMM**		
	Set 1	**Set 2**	**Set 3**
$\mathbf{k_{Fz}}$ (N/m)	2.12E+08	2.11E+08	2.09E+08
$\mathbf{k_{M\theta y}}$ (N.m/rad)	5.51E+05	6.21E+05	1.11E+06
Real Stiffness Values			
$\mathbf{k_{Fz}}$ (N/m)		2.40E+08	
$\mathbf{k_{M\theta y}}$ (N.m/rad)		4.50E+05	
Absolute Value Error (%)			
$\mathbf{k_{Fz}}$ (N/m)	14.58	12.08	12.92
$\mathbf{k_{M\theta y}}$ (N.m/rad)	22.44	38.00	146.67

When the identified results are examined in Table 4-8, the ISMM does not work in experimental studies if the *Assumed Model* closely resembles the *Actual Model*. This means that if the assumed model natural frequencies differ from the actual model natural frequencies by around 24%, the identified natural frequencies by ISMM align well with the actual natural frequencies with around 1% error (Table 4-9). In *Assumed Model-Set3*, Actual and Assumed Models' first natural frequencies differ by 1.79%. Since the identification is made around the first natural frequency, the rotational stiffness value is identified with 146.67% errors. Therefore, it is concluded that in experimental studies, the assumed model should be selected as its natural frequencies differ by around %20 from the actual model counterparts.

Table 4-9 Identified natural frequencies for different assumed models

Model	Modes (Hz)	
	1st	2nd
Identified Model by ISMM- Assumed Model Set1	1792	5246
Identified Model by ISMM- Assumed Model Set2	1799	5258
Identified Model by ISMM- Assumed Model Set3	1825	5265
Actual Model (Simulated Experiment)	1779	5302

Table 4-10 Identified natural frequency errors

Model	Absolute Error of Identified Modes (%)	
	1st	2nd
Identified Model by ISMM- Assumed Model Set1	0.39	1.06
Identified Model by ISMM- Assumed Model Set2	1.12	0.80
Identified Model by ISMM- Assumed Model Set3	2.58	0.70

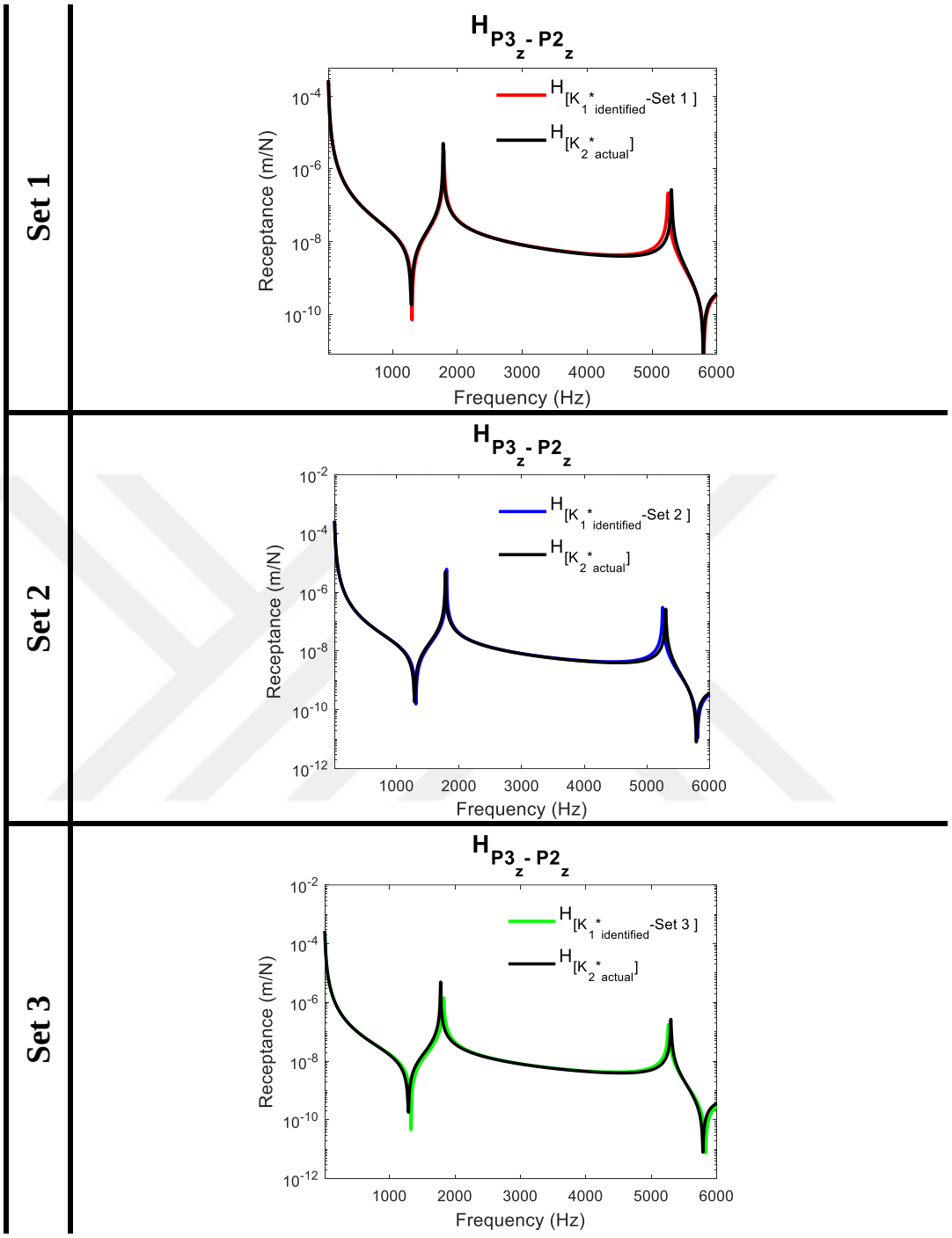


Figure 4.34 Comparison of obtained translational FRFs with identified stiffness values to their actual model equivalent for different Assumed Models

As the obtained rotational stiffness values (Table 4-8), the modes (Table 4-9), and their errors (Table 4-10) compared to actual values are examined, the rotational stiffness values in *Assumed Model-Set3* are identified with significant errors. Nevertheless, in light of the obtained modes (Table 4-9) and the FRFs (Figure 4.34), it is evident that this differentiation has no significant impact on the identified modes and the FRFs. That is because although the difference between the *Actual Model* and the *Assumed Model-Set3's* rotational stiffness values seems significant since the effects of the rotational stiffness are the same after a specific value, this difference does not significantly contribute to the results. This shows us that the effect of the rotational stiffness value is limited as long as the translational stiffness value is identified close enough to its actual counterparts.

CHAPTER 5

REAL EXPERIMENT STUDIES

In Chapter 4, all identification studies by ISMM are done using simulated experiments, which are obtained through FEM. Those works have enabled us to recognize the possible issues encountered in the identification procedure, and a clear road map for real experimental studies has been created. The created road map for contact identification through real experimental studies is shown in Figure 5.1

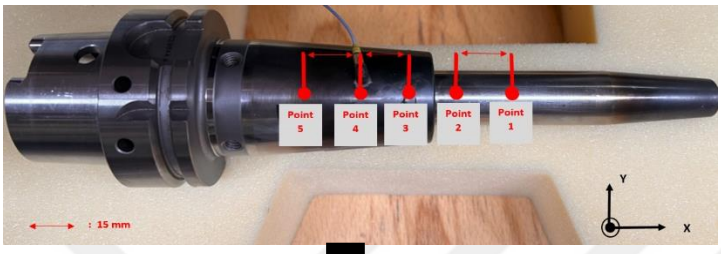
This chapter applies ISMM using direct experimental measurements on holder-extension assembly. A new extension length is used for the experimental verification, and tests are repeated with this new length. Another important topic that needs to be highlighted is the contact definition of the extension and the tool interface. Section 4.1 defines the tool and extension as a singular body with different material properties. However, in literature, a complex stiffness matrix also represents the contact between the extension and the tool. In simulated experimental studies, single body definition is not crucial since both assumed and actual models have the same tool contact definition. However, in real experimental studies, if the single-body assumption still holds, that will create additional differences coming from the contact definition of the extension and tool. Consequently, the error coming from the extension-tool contact will be compensated in the identified holder-extension contact dynamics, which will also, in the end, cause unrealistic identification of the stiffness values in the contact between the holder and extension. In this chapter, real experimental studies are executed only with the HE assembly (without a tool) to solve that issue. The tests are repeated with this assembly.

The length of the extension and the results of the new experiment are given in Section 5.2. After the details of the impact test are presented, the identification procedures

conducted via ISMM are implemented, and these procedures are elaborated upon in the relevant subsections.

Executing Impact Hammer Test of the HE assembly

To obtain the translational FRFs



↓

Curve Fitting to FRFs to Eliminate the Measurement Error

↓

Obtaining RDOF FRFs of P2 and P3

making use of the Finite Difference Technique [33]

↓

Creating the Assumed Model- ANSYS FE model

requires applying the ISMM

↓

Extract Translational and Rotational FRFs at P2 and P3 for Assumed Model through ANSYS Simulation

↓

Determine the Sensitivity Ranges to Identify the Stiffness Parameters

↓

Apply the ISMM to Obtain the Stiffness Properties Representing the Contact Dynamics Between the Holder and Extension

Figure 5.1 The procedure followed in identifying connection dynamics using real experimental data

5.1 Tool-Holder-Extension Impact Hammer Test

This experiment aims to determine the FRFs of the assembly for analyzing the interface dynamics of the holder and extension. Figure 5.2 depicts the test set-up and measurement points for data collection.

During the planning phase of the test, it became evident that FRFs at the contact faces would need to be obtained using FRF extension methods, as the contact faces are inaccessible. Before starting measurement, it is decided that the SEMM (System Equivalent Model Mixing) method [25] will be used as an expansion technique. That is why five locations in Figure 5.2 are being considered. Also, those points are determined under the assumption that the interface between the holder and extension is done on the single face depicted in Figure 5.2. Section 4.3 describes how these data points are used in the expansion method.

The assembly is located on the sponge (Figure 5.2) to conduct the free-free modal impact test. The Z and RotY axes are considered degrees of freedom. The equipment and software utilized in this experiment are outlined in Table 5-1.

The assembly is excited in the +Z direction, and only FRFs in direction Z are gathered. The frequency range is set to 10 kHz. CutPRO software is used for modal testing. The modal test setup parameters of the CutPRO are given in Figure 5.3. Due to the limited availability of accelerometers, one accelerometer is relocated to the subsequent data point for each run. The obtained FRFs in the Z direction are presented in Figure 5.4. Due to the necessity of specialized equipment for measuring rotational FRF in the RotY direction, such observations were not feasible during impact testing. The Finite Difference Technique [33] is employed in related sections to obtain rotational FRFs at specific data points. Those results are not presented here because they are not direct experiment results.

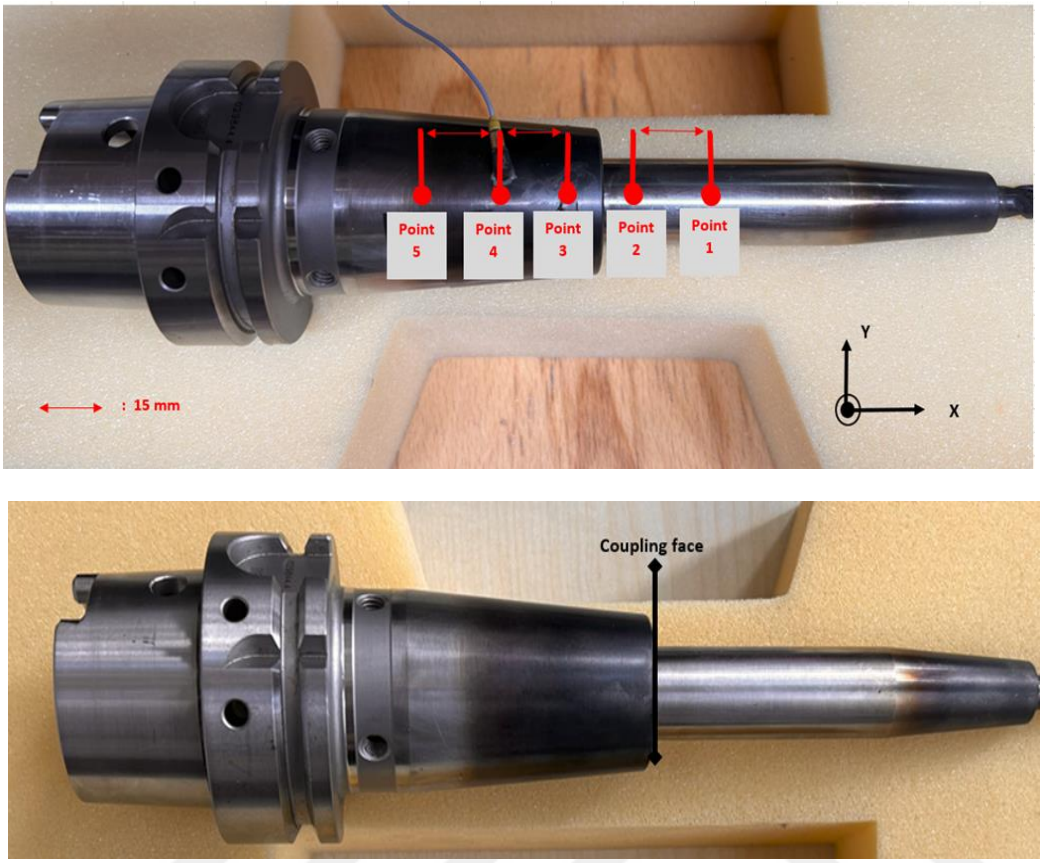


Figure 5.2 Data points and test set-up

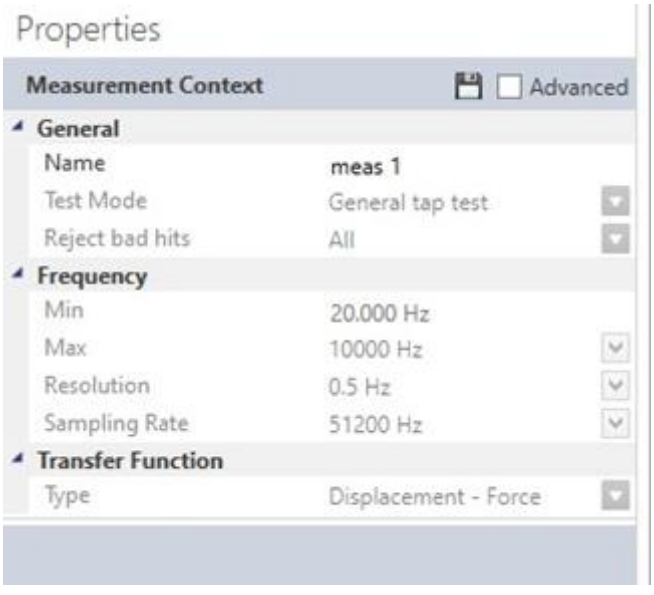


Figure 5.3 Test setup- CutPRO settings

Table 5-1 Modal impact test equipment and software

Test Equipment		
Accelerometer	PCB 3252C23 SN LW260924	
Hammer	PCB TLD086C03	
DAQ Hardware	The Natural Instruments (NI) cDAQ-9174	
DAQ Software	CutPRO	

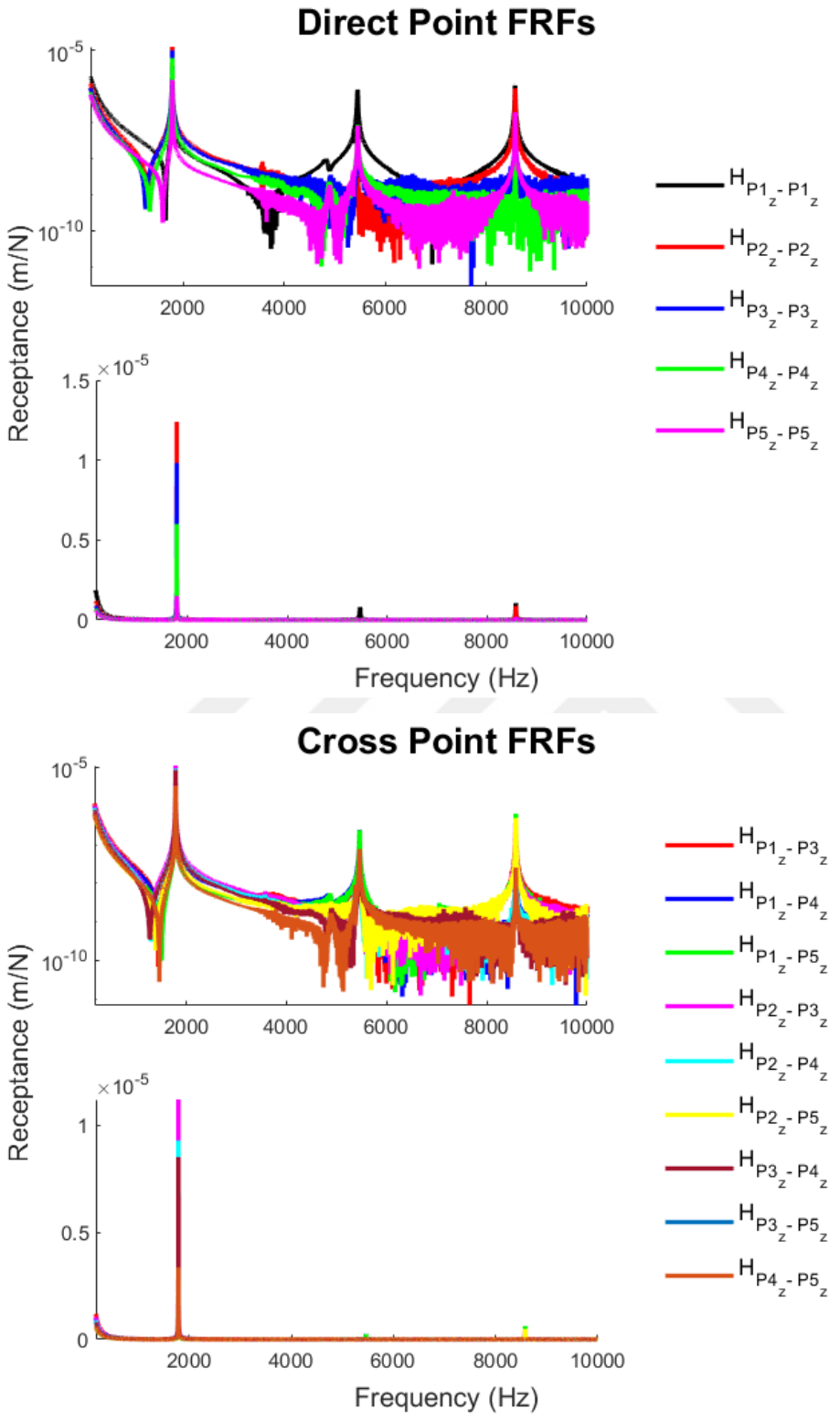


Figure 5.4 Direct (upper) and Cross (lower) FRFs from experiments

5.2 Impact Hammer Test via New Extension

As stated at the beginning of this chapter, impact hammer tests are performed on holder-extension assembly with 140 mm extension length. However, all other test plans remain unchanged, including the data point locations, test equipment and software used, and software settings outlined in Section 5.1. The measured translational FRFs obtained are given in Figure 5.5.

As seen from Figure 5.5, the *Fitted* FRFs obtained using the modal curve fit algorithm are also shared. Fitting is done to eliminate the noise in the Measured data. Peak-Pick Method in HBM nCode software is used as a curve fit algorithm. The Peak-Pick Method is a mainly SDOF method that looks only at the gain of the FRF and estimates modal parameters one mode at a time. To generate fitted FRFs, a list of natural frequencies has to be defined. Through the defined natural frequencies, identification of the newly fitted FRF is generated by identifying the half-power (-3 dB) points. The details of how this fitting approach is implemented in the HBM nCode Software can be found in [34].

To make it clear, the names used in Figure 5.5 are as follows:

- *Measured*: FRF results that are extracted from the impact hammer test
- *Fitted*: Fitted FRFs to the Measured FRFs.

As seen from Figure 5.5, the fitted FRFs align with the measured equivalents at the eigenfrequencies. However, slight discrepancies, particularly around the anti-resonance frequencies, are likely due to noise and selected fitting parameters.

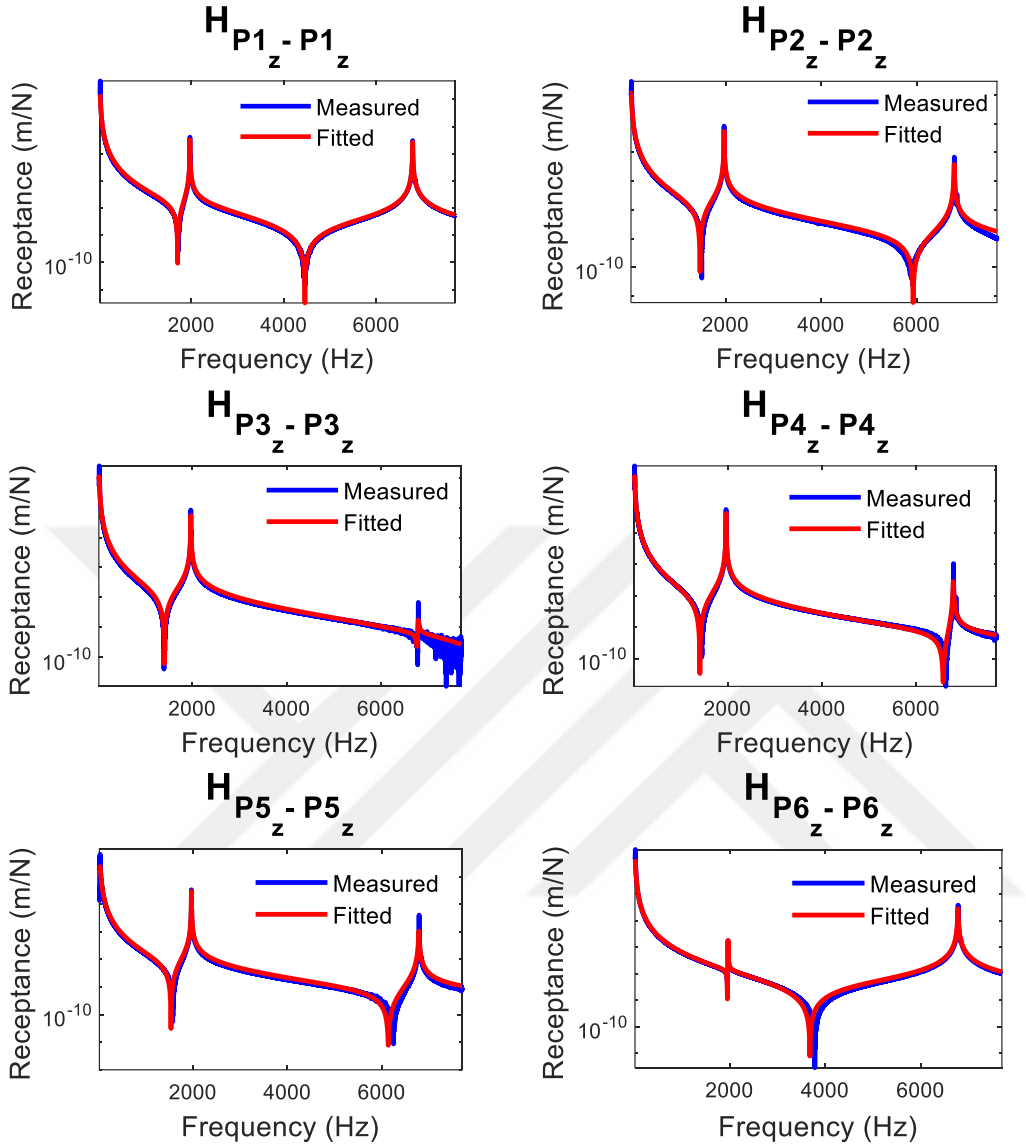


Figure 5.5 FRFs from impact hammer test and their fitted counterparts

To utilize the measured FRFs in the ISMM, it is necessary to identify the rotational FRFs at points P2 and P3, along with the direct and cross-translational FRFs. The subsequent section provides the rotational FRFs for P2 and P3.

5.3 Estimation of RDOF FRFs by Finite Difference Technique

The rotational FRFs for points P2 and P3 (Figure 4.16) are determined for the Measured and Fitted FRFs. The FDT is employed once again to identify the rotational FRFs. However, it should be noted that although the FRFs (*Measured* and *Fitted* ones) in Figure 5.5 demonstrate satisfactory agreement, they are not a perfect match. The subsequent sections will also delve into the effects of curve-fitting on the identification results.

To generate rotational FRFs at P2, the FRF results of P1 and P2 are utilized. Only first-order FDT results are presented in Figure 5.6. In Section 4.3.2, it was observed that for the simulated experiment, the first-order results for P2 were closer to their FEM counterparts. As a result, in the identification processes of this chapter, the 1st-order FDT results regarding P2 are utilized. Figure 5.6 shows that minor errors become more evident and impactful after the matrix multiplication process of the FD method, as indicated in [35]. The study [35] mentions that when the translational FRFs have measurement errors, this error is amplified after propagation of the FD method. In this study, an error analysis is used to prove the instability of FDT when noisy data are used. Then, they proposed an optimum spacing to balance the numerical and propagation errors from FDT. The details and outcomes of the executed studies are given in [35]. The same calculations are repeated for *Fitted* FRFs, and rotational FRF results at P2 are shared in Figure 5.7. Since there are no numerical or measurement errors in the *Fitted* FRFs, the approximated RDOF FRFs have no contamination, unlike those approximated from *Measured* ones.

Similarly, translational FRFs at points P3 and P4 are required to generate RDOF FRF at P3. The rotational FRFs obtained at P3 from *Measured* and *Fitted* FRFs are shown in Figure 5.8 and Figure 5.9, respectively. It should be noted that the ISMM calculation will be performed using the first-order results, as stated previously.

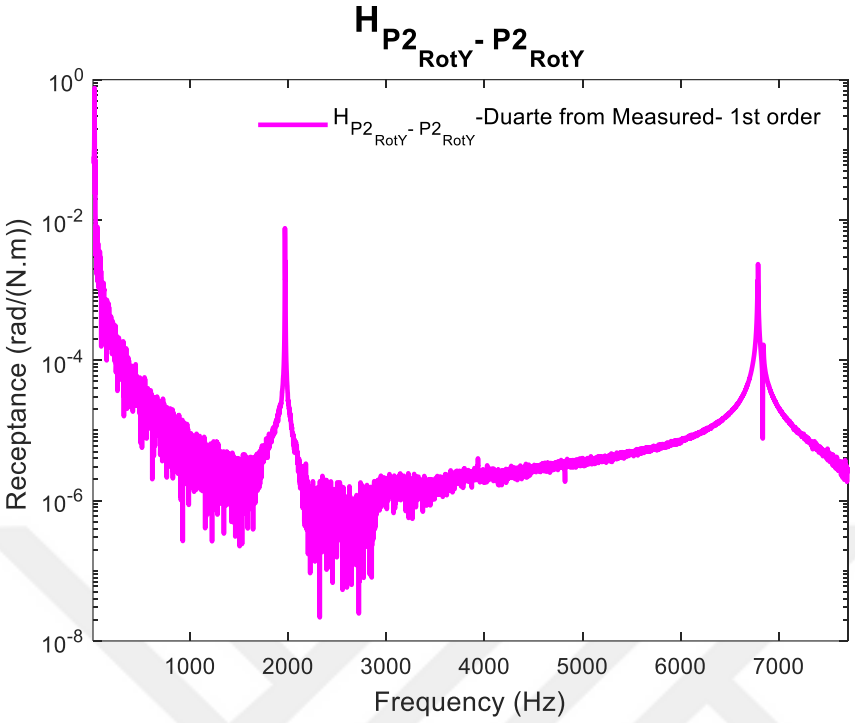


Figure 5.6 Approximated RDOF FRFs from *Measured* FRFs at P2

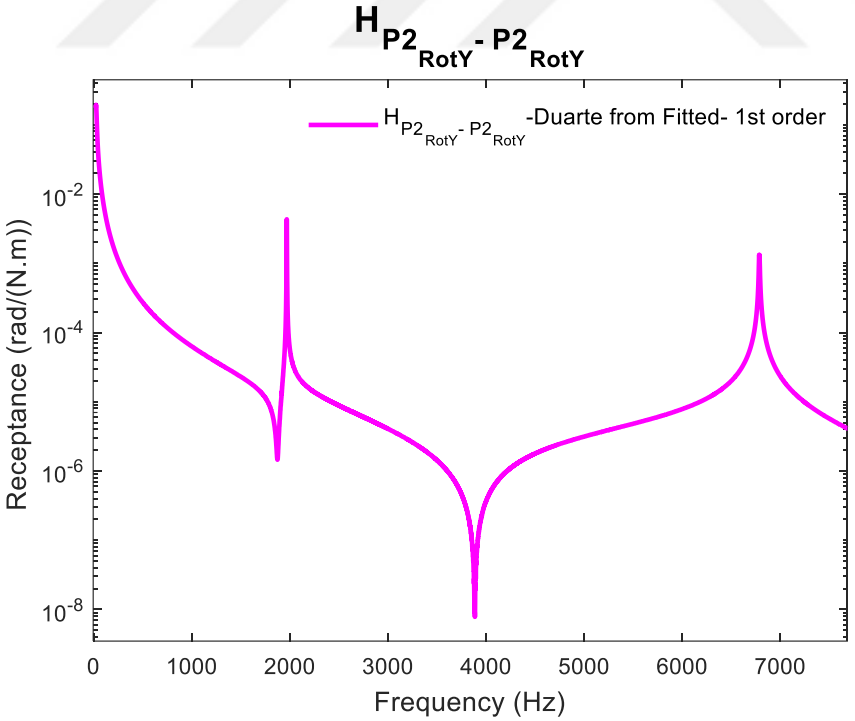


Figure 5.7 Approximated RDOF FRFs from *Fitted* FRFs at P2

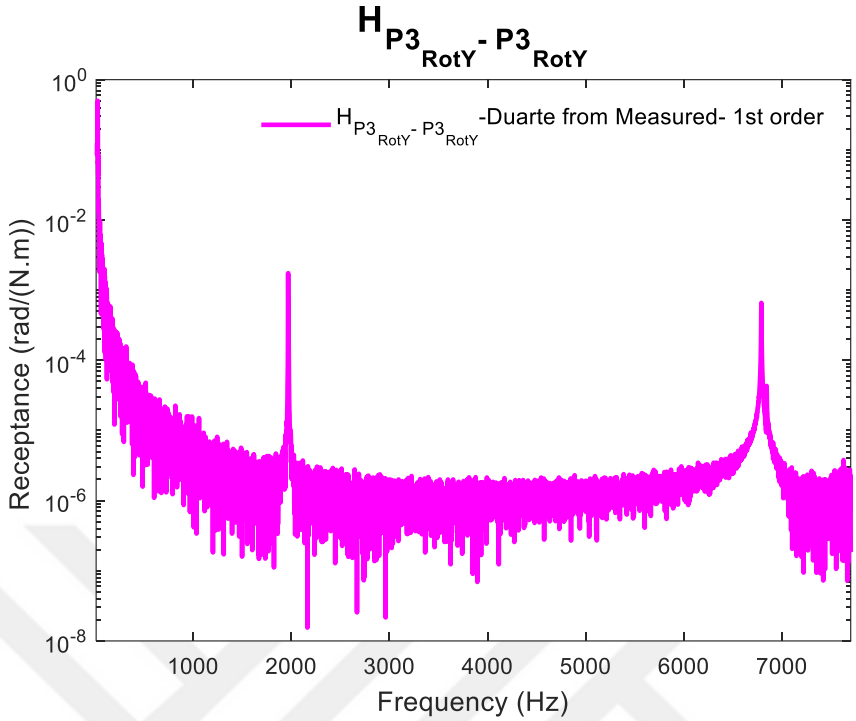


Figure 5.8 Approximated RDOF FRFs from *Measured* FRFs at P3

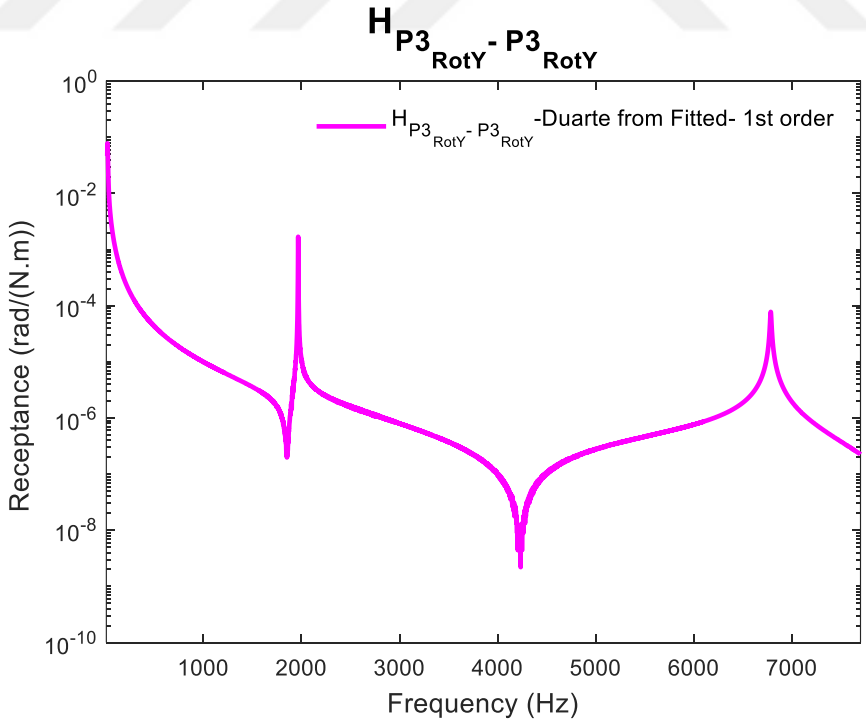


Figure 5.9 Approximated RDOF FRFs from *Fitted* FRFs at P3

5.4 Contact Dynamics Identification by ISMM

The implementation of the ISMM in experimental studies also necessitates the use of an assumed model. As the assumed model, an ANSYS FE simulation is developed. However, this simulation undergoes specific alterations compared to the one in Section 4.1, which are detailed in Section 5.4.1.

5.4.1 Assumed Model for ISMM

In order to apply the proposed ISMM procedure to the experimental results, it is necessary to obtain an assumed model. So, firstly, the assumed model is created using ANSYS software in Section 4.1 and employed with the new extension length.

The assembly modes are directly influenced by the material properties, specifically Young's Modulus and density values of the holder and extension. During the assembly process, which involves shrink-fit, the holder and extension are subjected to high temperatures that can potentially alter the Young's Modulus of the materials. In order to eliminate any errors caused by Young's Modulus and to accurately determine the elastic modulus value, stand-alone free-free impact hammer tests are conducted for both the holder and extension. The Young's Modulus values are then determined by comparing the first two natural frequency results obtained from the FE model and impact tests (Figure 5.10). Identified Young's modulus values are presented in Table 5-2. Then, the assumed model uses identified values as the material properties. All other mechanical properties in Section 3.2 remain unchanged.

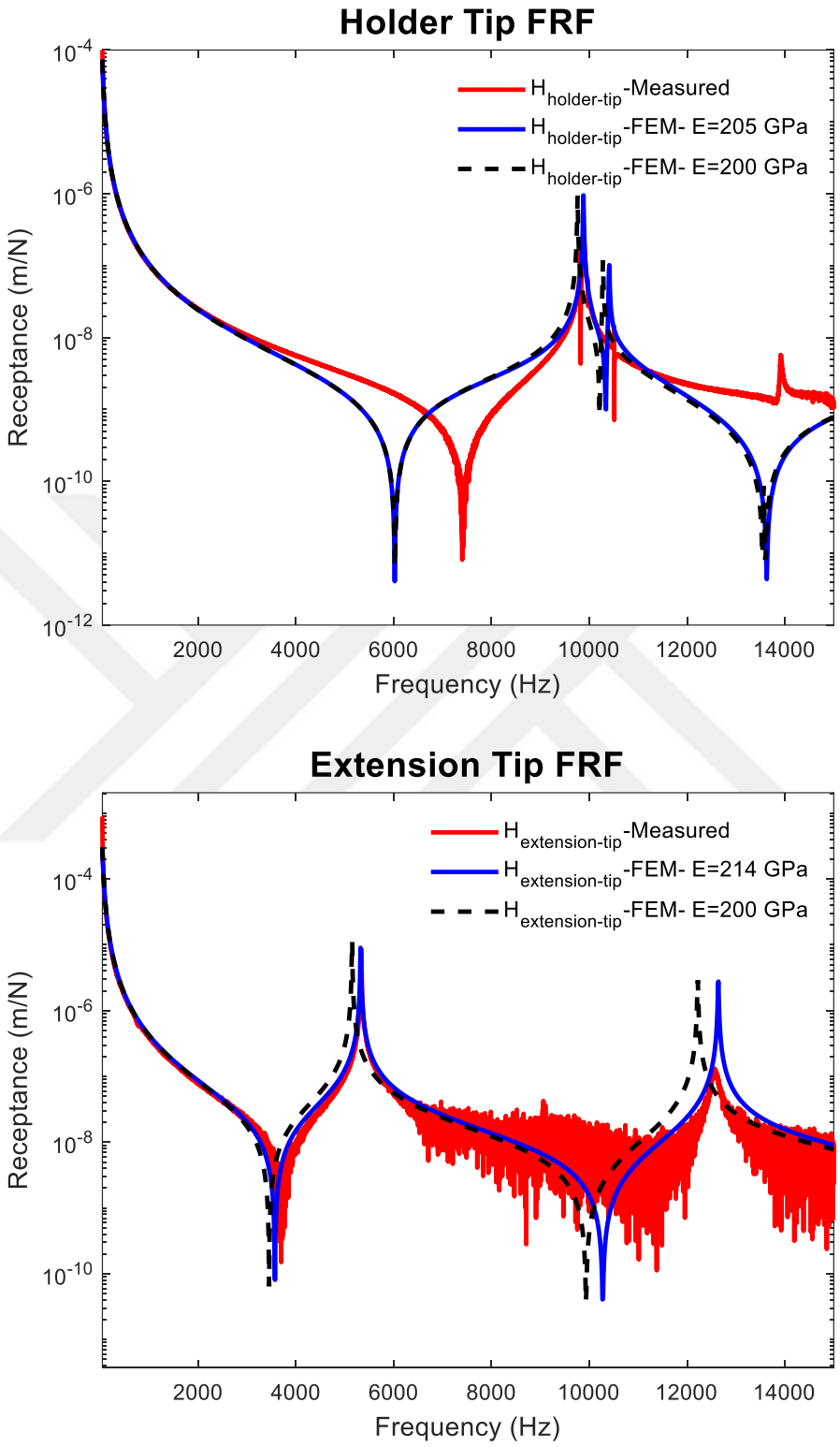


Figure 5.10 Comparison of the holder-tip (upper) and extension-tip (lower) FRFs

Table 5-2 Young's of the holder and extension identified by impact hammer test results

Stainless Steel	Young's Modulus- E (GPa)
Defined in ANSYS Software	200
Identified with Impact Hammer Test for Holder	205
Identified with Impact Hammer Test for Extension	214

In Section 4.6, it is concluded that the assumed model gives good alignment if the assumed and actual models' first and second natural frequencies change around 15%. Based on this information, the stiffness values of the assumed model are selected as given in Table 5-3. The obtained cross-translational FRF between P2 and P3 is shared in Figure 5.11.

Table 5-3 Defined assumed stiffness and damping properties

Assumed- α Model Stiffness and Damping Properties		
Stiffness Properties	$\mathbf{k_{Fz}}$ (N/m)	5.00E+07
	$\mathbf{k_{M\theta y}}$ (N.m/rad)	5.00E+04
Constant Structural Damping		0.001

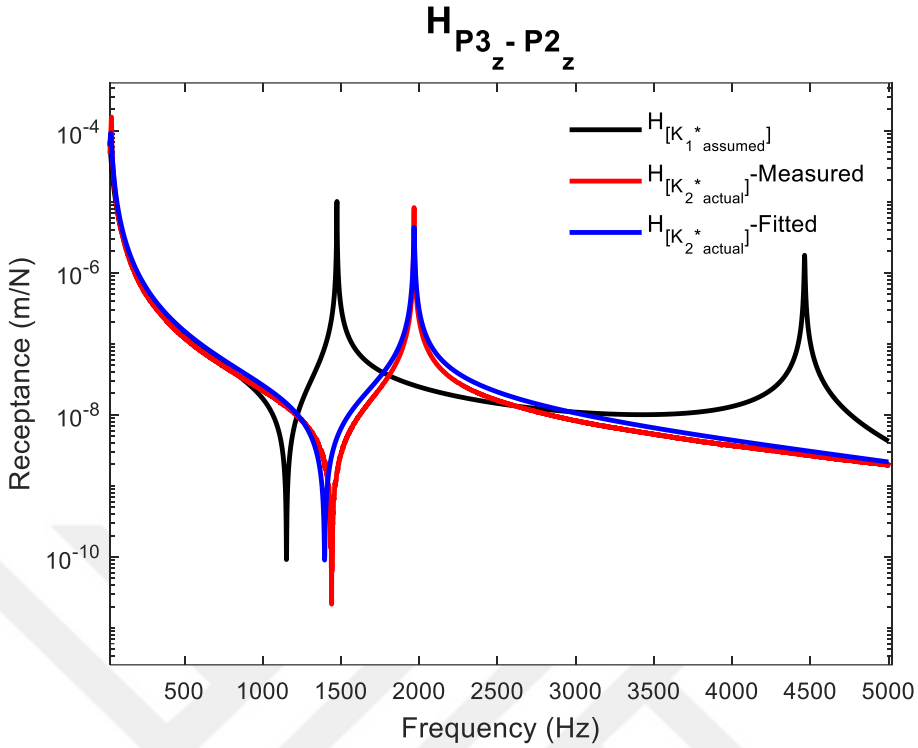


Figure 5.11 Comparison of cross translational FRFs between P2 and P3

Figure 5.11 shows that the actual HET assembly has only one eigenfrequency within the designated frequency range, whereas the presumed model has two. Before moving to contact dynamics identification by ISMM, since the length of the extension and the assumed stiffness values are changed, the sensitivity analyses need to be repeated. The calculated FRFs for three different translational and rotational stiffness values are given in Figure 5.12.

Figure 5.12 shows that the first frequency is primarily influenced by rotational stiffness, while the second natural frequency is influenced by translational stiffness.

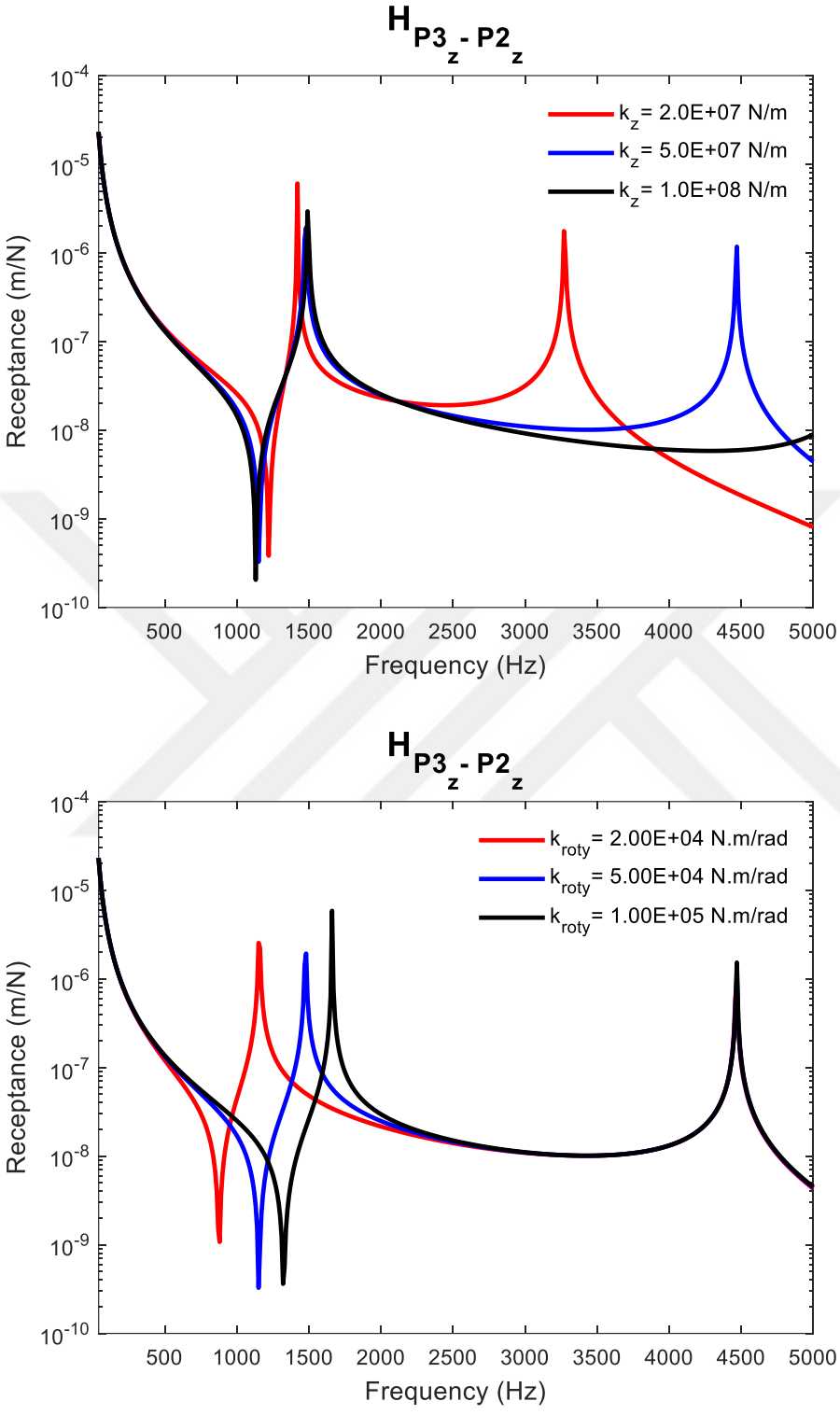


Figure 5.12 Cross translational FRF between P3 and P2 for different translational (upper) and rotational (lower) stiffness values

5.4.2 Identification of The Contact Parameters by ISMM

The *Measured* and *Fitted* experimental FRF sets and the presumed model are utilized in the identification operations. Before initiating the identification procedure, it is necessary to determine the identification ranges. If the entire region where differentiation begins in Figure 5.12 is selected, as in the simulated experiment investigations, the identification results are shown in Figure 5.13 and Figure 5.14. Are obtained. However, determining the mean of these ranges reveals that the identification results are unreliable due to the models being from different environments, which are simulated and actual experiments. That is why the identification will be made around natural frequencies where the stiffnesses significantly affect the related natural frequency. In Figure 5.11, it is seen that the first natural frequency is around 1967 Hz. In Figure 5.12, the effective frequency of the rotational stiffness values shows significant effects in the range of 1920-2000 Hz. The effect of the translational stiffness value becomes significant in the 4400-4500 Hz range.

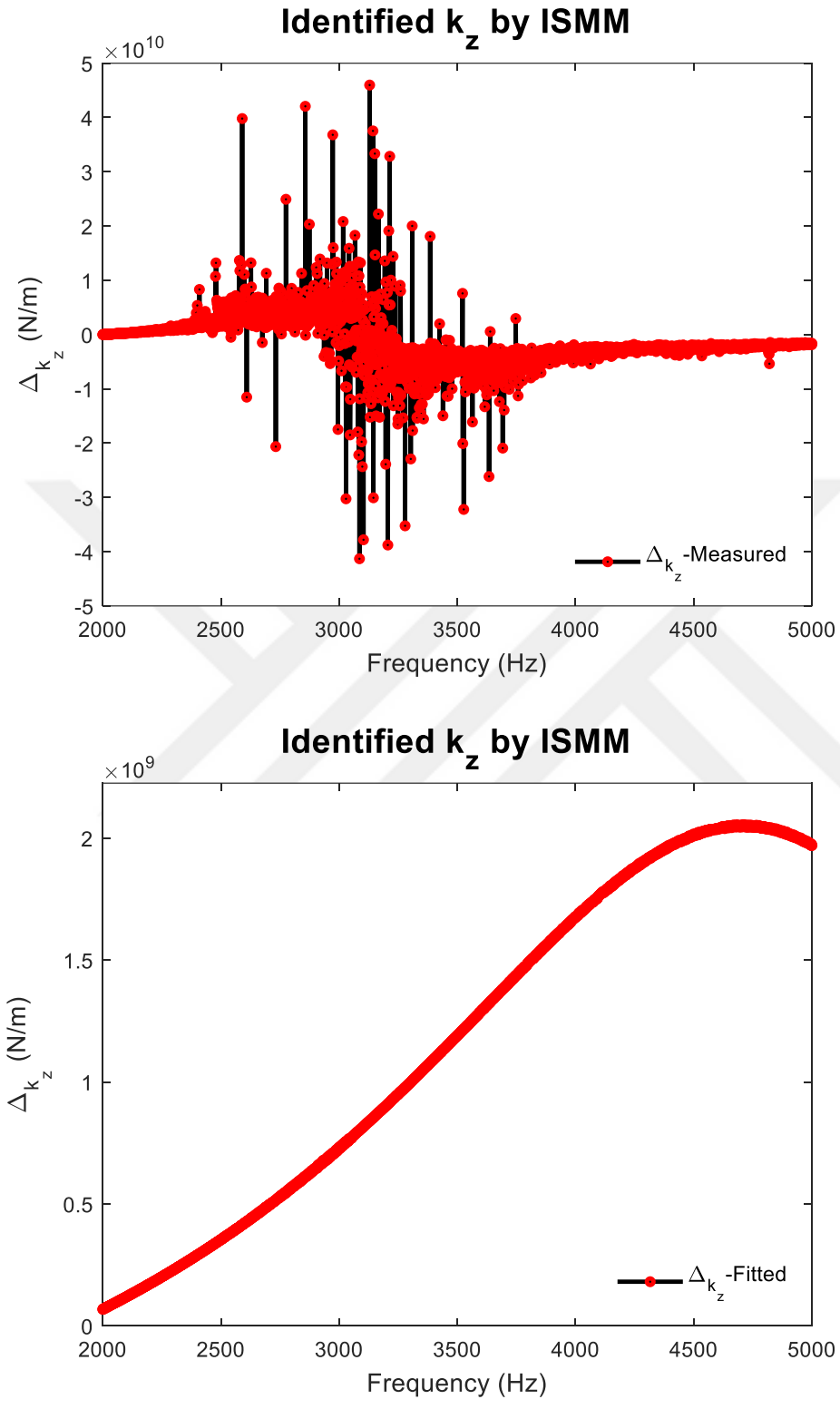


Figure 5.13 Identified translational stiffness values by ISMM for *Measured* (upper) and *Fitted (lower)* models

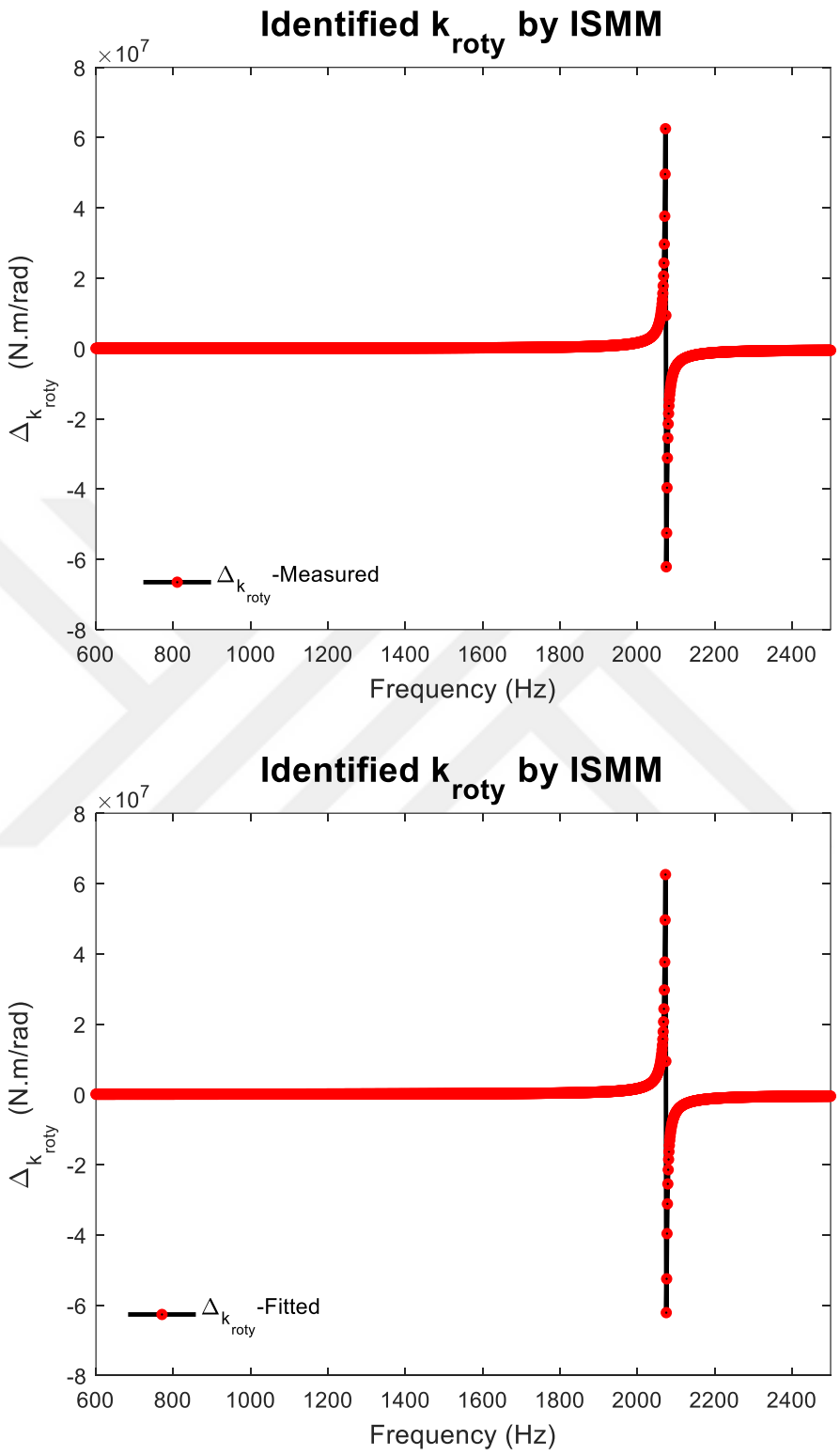


Figure 5.14 Identified rotational stiffness values by ISMM for *Measured* (upper) and *Fitted (lower)* models

The identified translational and rotational stiffness values in the effective ranges are presented in Figure 5.15 for both the *Measured* and Fitte*d* models.

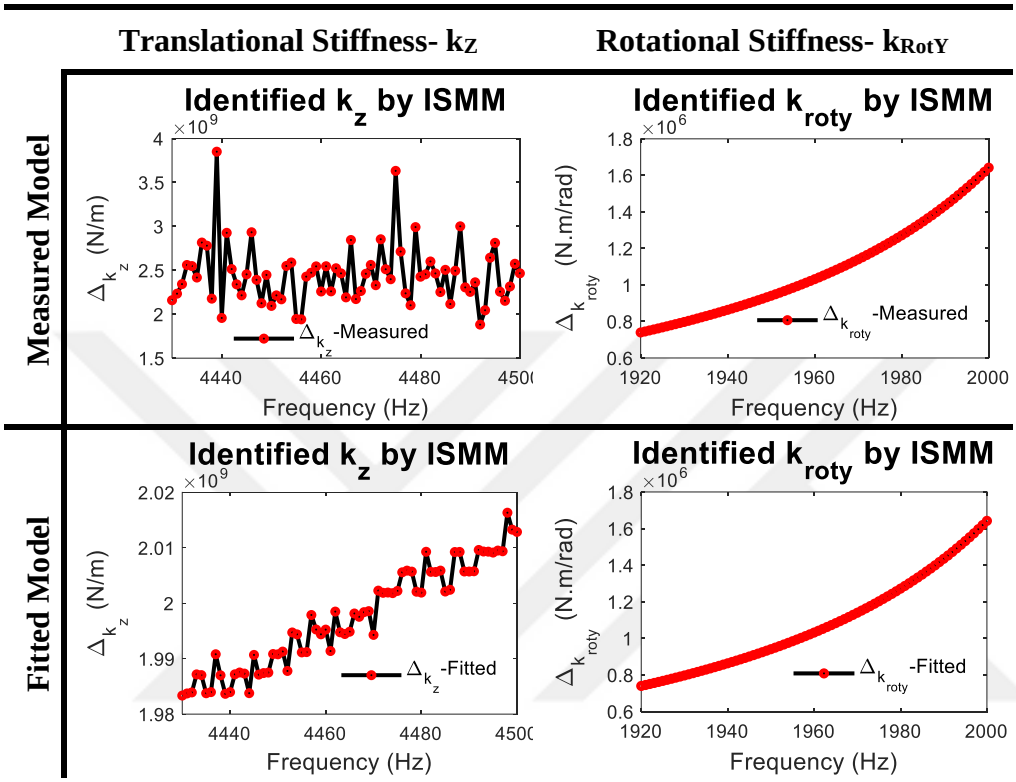


Figure 5.15 Identified stiffnesses for *Measured* (upper) and *Fitted* (lower) model values by ISMM

In Figure 5.15, the fluctuation of the identified rotational stiffness value, between 0.7E+06 and +1.6E+06, implies that the rotational stiffness identification is sensitive to the identification range. This range is determined by the sensitivity analysis given in Figure 5.12. Nevertheless, that range is more extensive when the assumed and experimental models' first eigenfrequencies are examined. Since the first natural frequency of the experimental results is around 1967 Hz, the rotational stiffness value identification range is limited to the close vicinity of 1967 Hz. The range of

the rotational stiffness value is set from 1950 to 1980 Hz. The identification results of the rotational stiffness value in that range are shared in Figure 5.16.

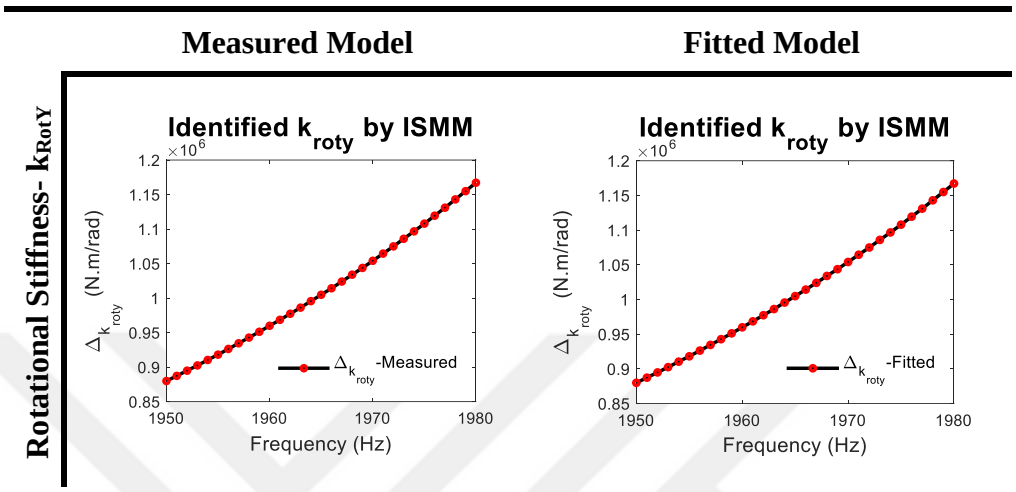


Figure 5.16 Identified rotational stiffness values for *Measured* (left) and *Fitted* (right) models by ISMM (1950-1980 Hz)

In Figure 5.16, the fluctuation is lower compared to the more extensive range in Figure 5.15. To get the newly identified stiffness value, the mean values of the identified translational stiffness value from the *Fitted* model, in Figure 5.16, and rotational stiffness values for both experiment models are calculated and shared in Table 5-4.

Table 5-4 Identified stiffness values

Stiffness Directions	**Identified Stiffness Values**	
	ISMM with *Measured FRFs*	**ISMM with *Fitted* FRFs**
$\mathbf{k_{Fz}}$ (N/m)	2.50E+09	2.01E+09
$\mathbf{k_{M\theta y}}$ (N.m/rad)	1.11E+06	1.11E+06

Upon evaluating the final results in Table 5-4, it becomes apparent that the effects of the noise become significant in the identified translational stiffness values. In contrast, there is no significant difference between the obtained rotational stiffness values for *Measured* and *Fitted Models*. With the newly identified stiffness values, the FRF is regenerated in ANSYS, and the obtained FRF is compared with its fitted experimental and assumed counterparts in Figure 5.17.

Figure 5.17 shows that both identified models, *Measured* and *Fitted* FRFs, align well with the experiments' first and second natural frequencies and FRFs. Due to the logarithmic scale of the figure, values in the range of E-08 and below seem to have significance. However, as the discrepancies approach zero, it can be concluded that the identified FRF outcomes exhibit satisfactory agreement with their experimental counterparts. Other factors that explain the FRF mismatch are the assumptions about the created FE model (see Section 5.4.1). Given all of these matters, the identification study is considered successful.

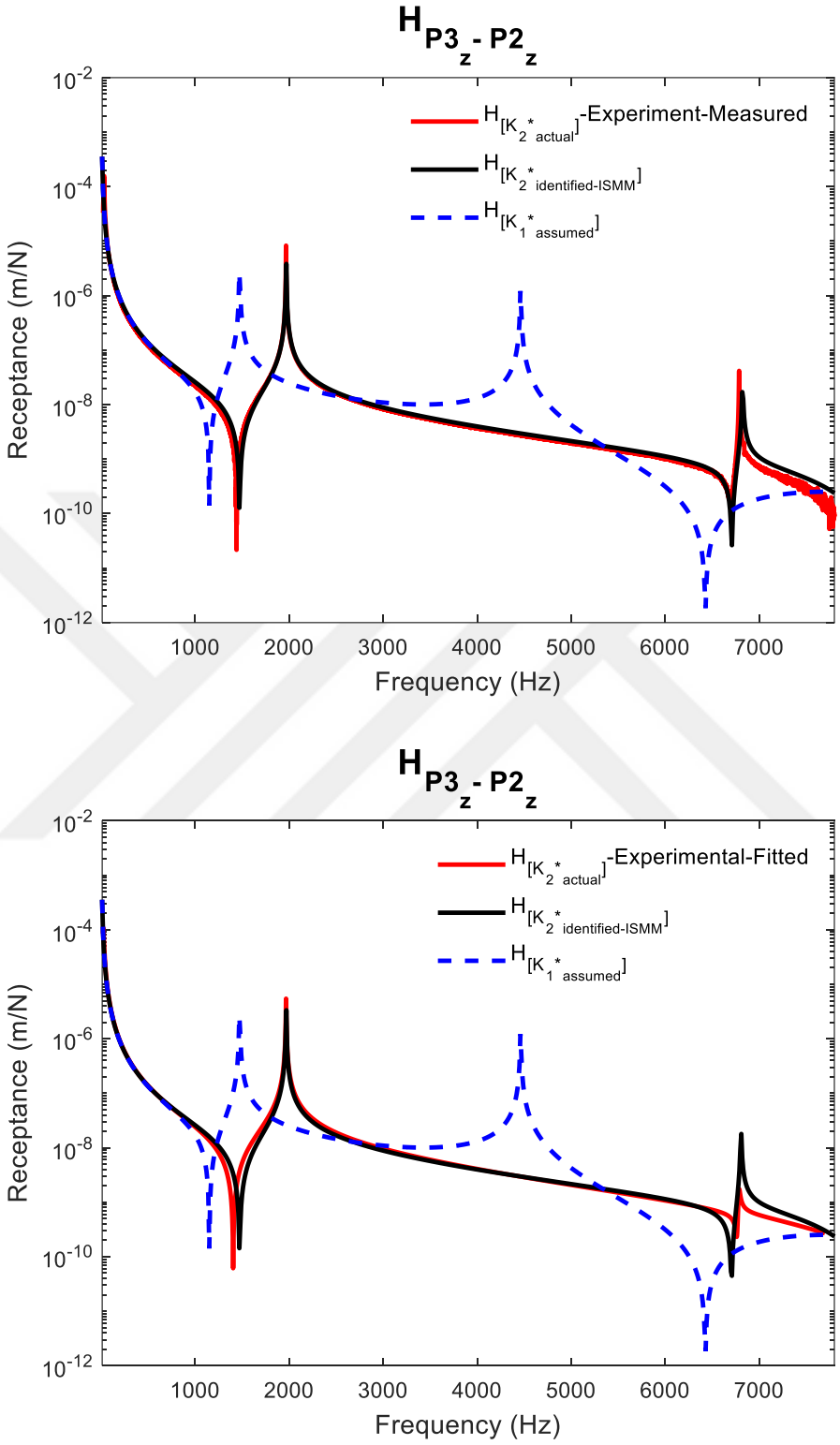


Figure 5.17 Calculated cross translational FRFs between P2 and P3 using identified contact parameters for *Measured* (upper) *Fitted* (lower) FRFs

The exact stiffness value of the actual contact dynamics is unknown. The accuracy of the identified model can be determined by comparing the FRFs in Figure 5.17 and the identified natural frequency values. Since the exact value of the first two natural frequencies of the experimental results is known, the complete set of identified natural frequency results is shared in Table 5-5 to discuss the accuracy of the identified natural frequencies.

Table 5-5 Identified natural frequencies

Model	**Modes (Hz)**	
	1st	**2nd**
Predicted (by contact parameters identified using direct measurements)	1968	6824
Predicted (by contact parameters identified using fitted FRFs)	1968	6807
Real Experimental Results	1968	6785

Table 5-5 shows that the identified modes are close enough to their experimental counterparts. Also, the error of the identified results concerning the relevant model is shared in Table 5-6.

Table 5-6 Error of the identified natural frequencies

Model	Absolute Error of Identified Modes (%)	
	1st	2nd
Predicted (by contact parameters identified using direct measurements)	0.00	0.58
Predicted (by contact parameters identified using fitted FRFs)	0.00	0.32

Based on the data presented in Table 5-5, it can be observed that the first natural frequency is predicted without any error. The errors associated with the determined 2nd natural frequency are not even approximately one percent. Consequently, it can be concluded that the ISMM effectively determines the stiffness values that characterize the contact dynamics between the holder and extension.

In experimental studies, it is concluded that having an FE model representing the accurate HE assembly is crucial to obtaining a good estimation by ISMM. Additionally, the effective region of the directional stiffnesses allows for selecting the correct range for identification. When the identification range is correctly estimated, the ISMM results align well with the experiment. It should be noted that as the frequency ranges increase and the noise in the data becomes more dominant, the fitted models can be used to obtain reliable results and eliminate the effects of the noise on the results.

5.5 Importance of the Contact Dynamics Definition via Complex Stiffness Matrix

Up until now, the effectiveness of the ISMM in contact dynamics identification has been investigated. However, it is critical to determine whether the complex stiffness matrix representation of the contact dynamics is required. To check this matter, the

contact is defined as rigid through the contact dynamics interfaces in the FE simulation instead of using the stiffness matrix between the holder and extension. The translational FRF results for the rigid contact definition are compared to its identified and experimental equivalents in Section 5.4.2. The calculated FRF for the rigid contact is shown in Figure 5.18, along with the measured and identified FRFs.

As seen in Figure 5.18, it can be observed that the bonded contact definition has an impact on the assembly modes. The first natural frequency increased from 1968 Hz to 2041 Hz, indicating a difference of 3.71%. Similarly, the second natural frequency changed from 6785 Hz to 6958 Hz, showing a difference of 2.55%.

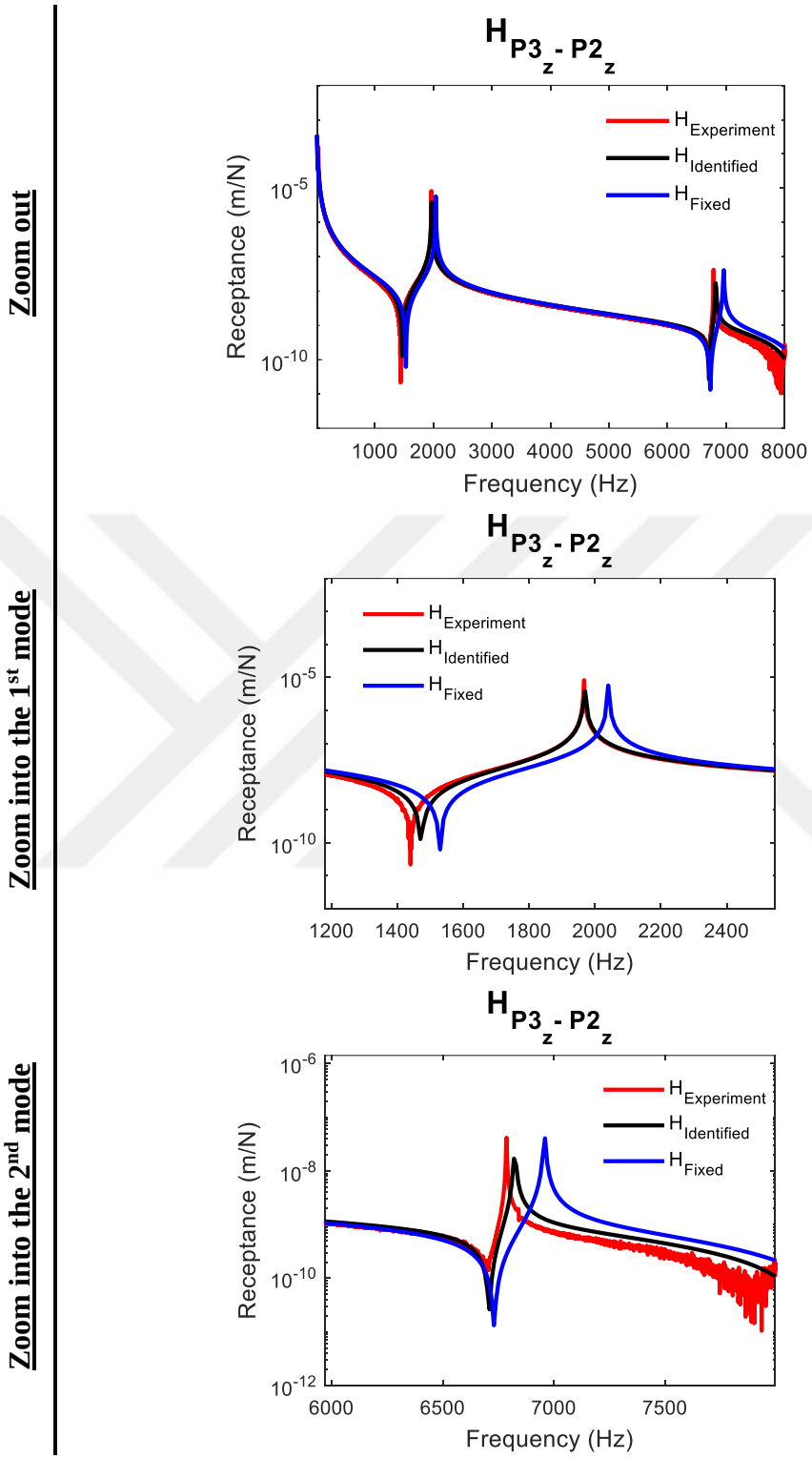


Figure 5.18 Direct translational FRF at P3 -FRF obtained by bonded contact definition and comparison with identified FRF

CHAPTER 6

CONCLUSION AND FUTURE WORK

6.1 Conclusion

The definition of joints, whether bolted, welded, or shrink fit, can vary depending on the specific system being considered. However, it is crucial for any system that involves joints or contact dynamics to have a clear understanding of the dynamics of these joints in order to represent the overall system dynamics using numerical models. The identification of joint dynamics can be achieved using coupling and decoupling methods, such as utilizing modal domain results or the receptance results of the system and its subcomponents. In the case of bolted joint assemblies, joint identification involves the use of receptance coupling, decoupling methods, and structural modification methods. Similarly, when identifying contact dynamics, the same receptance coupling and decoupling methods are used to identify the interface dynamics between the holder, extension, and tool in machine tool dynamics.

The Inverse Structural Modification Method (ISMM) is a contact dynamics identification method primarily used for in-line beams assembled by bolted joints. However, the method lacks experimental evidence to validate its effectiveness and relies solely on numerical examples for verification. This thesis aims to address this gap by demonstrating the application of ISMM through numerical, simulated experimental, and real experimental studies. The objective is to identify the complex stiffness matrix representing the contact dynamics between the holder and extension in milling machines. Both numerical and experimental studies are conducted in this thesis to show the applicability of the methods, specifically in the context of the holder-extension assembly. In these studies, quasi-static contact dynamics models are used. The contact dynamics are represented with a 2 DOF, namely translational and rotational, complex stiffness matrix.

The contact dynamics between the H and E are initially analyzed using the ISMM method, which utilizes numerical results from ANSYS FE simulation to extract translational and rotational FRFs of the contact dynamics. The application of ISMM to identify the complex stiffness matrix representing the contact dynamics shows satisfactory alignment between the identified stiffness values and the actual values. However, the identified viscous damping values deviate significantly from their actual counterparts. That is because the defined viscous damping values are considerably lower than the defined stiffness values by a magnitude of E+05. As observed in this thesis, it is important to note that identifying small numbers can lead to substantial errors when performing matrix inversion calculations in the ISMM methods [17]. Therefore, only structural damping is considered in the upcoming works. Also, with the numerical studies, the effects of noise on the identification results are examined by the three sets of polluted numerical data. Through the examination of the effects of the noise on the ISMM, it is concluded that the method also gives reliable results even when the data is contaminated with zero mean with a standard deviation of 5% and 10% noisy data.

In the subsequent stage of the thesis, the focus shifts towards exploring the potential changes if the ANSYS FE model behaved as the actual experiment set-up, called simulated experimental studies. This scenario is designed to address any potential issues that may arise during the experimental identification study. Given that measuring rotational FRFs and accessing the contact dynamics interfaces of the assembly is challenging, it becomes necessary to employ expansion techniques to obtain rotational FRFs at the measurement points and the receptance matrix of the contact dynamics. The Finite Difference Technique (FDT) is employed to estimate RDOF FRFs at the measurement points. Using the obtained RDOF FRFs, the SEMM method is then applied to derive the complete receptance matrix of the contact dynamics. However, due to numerical errors resulting from matrix calculations in the SEMM Method, this method does not yield reliable and accurate outcomes. The impact of the FDT order on the results of the SEMM Method is also examined by comparing the RDOF FRFs from the FDT with those obtained from the FE

simulation. The conclusion drawn is that, as the boundary condition changes due to the contact dynamics definition, first-order FDT formulas give better results than second-order counterparts.

The SEMM method, when applied in simulated experimental studies, does not yield reliable FRFs for the contact face dynamics. As a result, the identification points need to be changed. These new identification points are selected as the closest points on the holder and extension to the interfaces. By utilizing these new identification points, the identified stiffness values at the interfaces align well with their actual counterparts. Furthermore, the effects of the assumed complex stiffness matrix model on the identification process using ISMM are examined through simulated experimental studies. Three different assumed models are used in these studies. It is observed that the assumed model should have natural frequencies that differ by at least 10% compared to the actual counterparts. Another finding is that selecting a rotational stiffness value beyond approximately 1E+06 N.m/rad does not significantly affect the natural frequencies of the identified system.

As the main contribution to the previous work [18], the ISMM is verified through experimental studies. The experiment results are collected through the free-free impact hammer test of the HE assembly. The peak-peak fitting algorithm is applied to experimental results to eliminate the effects of the noise on the identified stiffness values. Additionally, stand-alone impact hammer tests were employed to determine the actual values of the Young's Modulus for both the holder and the extension materials.

Identification studies are done for the measured and fitted FRFs to show the effects of the noise on the identified stiffness values. With the identified stiffness values, ANSYS FE simulations are repeated, and 1st natural frequency of the actual HE assembly is estimated by 0.00% error, while the 2nd natural frequency is estimated by 0.58% and 0.32% error for the measured and fitted experimental results, respectively. Also, it is observed that the FRFs of the actual system and the identified systems show good alignment.

Besides all identification studies, the contact definition between the holder and the extension is defined as to be rigid. This work aims to show how much improvement will be obtained by the contact stiffness definition instead of rigid contact. In rigid contact definition, the first and second natural frequencies are identified with errors of 3.71% and 2.55%, respectively. The errors of the identified modes are significantly reduced through contact dynamics identification by the ISMM.

6.2 Future Work

This study focuses solely on HE assemblies but can potentially be expanded to analyze the contact dynamics between the extension and the tool. The findings of this research specifically contribute to understanding the dynamics of HE assemblies. As a future direction, it would be interesting to explore how the identified stiffness values can be incorporated into machine tool dynamics, particularly for complex systems involving spindles, bearings, and tools.

REFERENCES

[1] Altıntaş, Y., and Budak, E. (1995). Analytical Prediction of Stability Lobes in Milling. *CIRP Annals - Manufacturing Technology*, 44(1), 357–362. https://doi.org/10.1016/S0007-8506(07)62342-7

[2] Schmitz, T., and Donalson, R. (2000). Predicting High-Speed Machining Dynamics by Substructure Analysis. *CIRP Annals*, 303-308. https://doi.org/10.1016/S0007-8506(07)62951-5

[3] Brecher, C., and Chaven P., F. M. (2016). A modal parameter approach for receptance coupling of tools. *MM Science Journal*, 1032-1034. doi:10.17973/MMSJ.2016_10_201616

[4] Ertürk, A., Özgüven, H., and Budak, E. (2006). Analytical modeling of spindle-tool dynamics on machine tools using Timoshenko beam model and receptance coupling for the prediction of tool point FRF. *International Journal of Machine Tools and Manufacture*, 46(15), 1901-1912. Retrieved from https://doi.org/10.1016/j.ijmachtools.2006.01.032

[5] Budak, E., Ertürk, A., and Özgüven, H. (2016). A modeling approach for analysis. *CIRP Annals*, 55(1), 369-372. Retrieved from https://doi.org/10.1016/S0007-8506(07)60437-5

[6] Park, S. S., Altıntaş, Y., and Movahhedy, M. (2003). Receptance coupling for end mills. *International Journal of Machine Tools & Manufacture*, 43(9), 889–896. Retrieved from https://doi.org/10.1016/S0890-6955(03)00088-9

[7] Özşahin, O., Ertürk, A., H., N. Özgüven, and Budak, E. (2009). A closed-form approach for identification of dynamical contact parameters in spindle–holder–tool assemblies. *International Journal of Machine Tools and Manufacture*, 49(1), 25-35. Retrieved from https://doi.org/10.1016/j.ijmachtools.2008.08.007

[8] Tony, L., and Scott, G. D. (2006). Receptance coupling for dynamics prediction of assemblies. *Journal of Sound and Vibration*, 289(4-5), 1045-1065. Retrieved from https://doi.org/10.1016/j.jsv.2005.03.006

[9] Namazi, M., Altıntaş Y., Abe, T., and N., R. (2007). Modeling and identification of tool holder–spindle interface dynamics. *International Journal of Machine Tools & Manufacture*, 47(9), 1333–1341. Retrieved from https://doi.org/10.1016/j.ijmachtools.2006.08.003

[10] Movahhedy, M. R., and Gerami, J. M. (2006). Prediction of spindle dynamics in milling by sub-structure coupling. *International Journal of Machine Tools and Manufacture*, 46(3-4), 243-251. Retrieved from https://doi.org/10.1016/j.ijmachtools.2005.05.026

[11] Mehrpouya, M., Graham, E., and Park, S. (2013). FRF based joint dynamics modeling and identification. *Mechanical Systems and Signal Processing*, 265-279. doi:10.1016/j.ymssp.2013.03.022

[12] Okubo, N., and Miyazaki, M. (1986). Development of uncoupling technique and its application. *Proceedings of the 4th International Modal Analysis Conference*.

[13] Ren, Y., and Beards, C. (1995). Identification of joint properties of a structure using FRF data. *Journal of Sound and Vibration*, 186(4), 567-587. Retrieved from https://doi.org/10.1006/jsvi.1995.0469

[14] Celic, D., and Boltezar, M. (2008). Identification of the dynamic properties of joints using frequency-response functions, *Journal of Sound and Vibration*, 317(1–2), 158-174.Retrieved from https://doi.org/10.1016/j.jsv.2008.03.009

[15] Celic, D., and Boltezar, M. (2009). The influence of the coordinate reduction on the identification of the joint dynamic properties. *Mechanical Systems and Signal Processing*, 23(4). Retrieved from https://doi.org/10.1016/j.ymssp.2008.11.002

[16] Wang, M., Wang, D., and Zheng, G. (2012). Joint dynamic properties identification with partially measured frequency response function. *Mechanical Systems and Signal Processing*, 27, 499-512. Retrieved from https://doi.org/10.1016/j.ymssp.2011.09.024

[17] Tol, S., and Özgüven, H. N. (2015). Dynamic characterization of bolted joints using FRF decoupling and optimization. *Mechanical Systems and Signal Processing*, 54–55, 124–138. Retrieved from https://doi.org/10.1016/j.ymssp.2014.08.005

[18] Özgüven, H. N., and Tekin, M. (2020). Dynamic Modelling of Bolted Joints Using Structural Modification Approach. *IMAC XXXVIII: Conference & Exposition on Structural Dynamics*, Houston, Texas. https://hdl.handle.net/11511/105239

[19] Meggitt, J., and Moorhouse, A. (2019). In-situ sub-structure decoupling of resiliently coupled assemblies. *Mechanical Systems and Signal Processing*, 117, 723-737. Retrieved from https://doi.org/10.1016/j.ymssp.2018.07.045

[20] O'Callahan, J., Avitabile, P., and Riemer, R. (n.d.). System equivalent reduction expansion process. *Proceedings of the 7th International Modal Analysis Conference, A Conference on Structural Dynamics.*

[21] Kim, Y., and Kang, J. (1997). A new experimental method to determine rotational modes from the strain measurement. *Proceedings of SPIE – The International Society for Optical Engineering*, 1415-1418.

[22] Williams, A., Chipman, C., and Avitabile, P. (2008). Modal and frequency based substructuring using rotational DOF considerations. *Proceedings of the 26th International Modal Analysis Conference, A Conference on Structural Dynamics*.

[23] Silva, T., and Maia, N. (2015). Estimation of rotational frequency response functions. *Proceedings of the 33rd IMAC, A Conference and Exposition on Structural Dynamics*, 35-48.

[24] van der Seijs, M., de Klerk, D., Rixen, D., and Rahimi, S. (2013). Validation of current state Frequency Based Substructuring Technology for the characterization of Steering Gear –. *Proceedings of the XXXI International Modal Analysis Conference.*

[25] Klaassen, S. W., Seijs, M. V., and Klerk, D. d. (2018). System Equivalent Model Mixing. *Mechanical Systems and Signal Processing*, 105, 90–112. Retrieved from https://doi.org/10.1016/j.ymssp.2017.12.003

[26] Saeed, Z., Firrone, C., and Ber, T. (2021). Joint identification through hybrid models improved by correlations. *Journal of Sound and Vibration*, 494. Retrieved from https://doi.org/10.1016/j.jsv.2020.115889

[27] Özgüven, H. N. (1987). Determination of Receptances of Locally Damped Structures. *Proceedings of the Second International Conference on Recent Advances in Structural Dynamics*, 887-892.

[28] Özgüven, H. N. (1990). Structural modifications using frequency response functions. *Mechanical Systems and Signal Processing*, 4(1), 53-63. Retrieved from https://doi.org/10.1016/0888-3270(90)90040-R

[29] GmbH, H. (2018). Mini shrink shrink fit extension- Haimer. Haimer GmbH. Retrieved from https://www.haimer.biz/products/toolholders/

[30] GmbH, H. (2020). Standard shrink fit Chuck HSK-A63 - Haimer UK. Retrieved from https://www.haimer.biz/products/tool-holders/din-69893-hsk-a-hsk-e-hskf/

[31] Ansys®. (n.d.). Mechanical APDL, Release 23.2, Help System, Theory Reference. ANSYS, Inc.

[32] Matthias, W. ,Özşahin, O., Altıntaş, Y., and Denkana, B. (2016). Receptance coupling based algorithm for the identification of contact parameters at holder–tool interface. *CIRP Journal of Manufacturing Science and Technology*, 13, 37-45. Retrieved from https://doi.org/10.1016/j.cirpj.2016.02.005

[33] Duarte, M. L., and Ewins, D. J. (2000). Rotational Degrees of Freedom for Structural Coupling Analysis via Finite-Difference Technique with Residual Compensation. *Mechanical Systems and Signal Processing*. Retrieved from https://doi.org/10.1006/mssp.1999.1241

[34] HBM nCode, VibeSys, Release 2021.0, Help System, Theory Guides, Hottinger Brüel & Kjaer GmbH.

[35] Gibbons, T., Öztürk, E., and Sims, N. (2019). Rotational degree-of-freedom synthesis: An optimized finite. *Journal of Sound and Vibration*, 412, 207–221. Retrieved from https://doi.org/10.1016/j.jsv.2017.09.031